PROBING LOCAL CONFORMATION AND DYNAMICS OF MOLECULAR

COMPLEXES USING PHASE-SELECTIVE FLUORESCENCE CORRELATION

AND COHERENCE SPECTROSCOPY

by

GEOFFREY ADAM LOTT

A DISSERTATION

Presented to the Department of Physics
and the Graduate School of the University of Oregon
in partial fulfillment of the requirements
for the degree of
Doctor of Philosophy

June 2010

University of Oregon Graduate School

Confirmation of Approval and Acceptance of Dissertation prepared by:

Geoffrey Lott

Title:

"Probing Local Conformation and Dynamics of Molecular Complexes Using Phase-Selective Fluorescence Correlation and Coherence Spectroscopy"

This dissertation has been accepted and approved in partial fulfillment of the requirements for the degree in the Department of Physics by:

Hailin Wang, Chairperson, Physics
Andrew Marcus, Advisor, Chemistry
Stephen Gregory, Member, Physics
Michael Raymer, Member, Physics
Marina Guenza, Outside Member, Chemistry

and Richard Linton, Vice President for Research and Graduate Studies/Dean of the Graduate School for the University of Oregon.

June 14, 2010

Original approval signatures are on file with the Graduate School and the University of Oregon Libraries.

An Abstract of the Dissertation of

Geoffrey Adam Lott   for the degree of   Doctor of Philosophy

in the Department of Physics   to be taken   June 2010

Title: PROBING LOCAL CONFORMATION AND DYNAMICS OF MOLECULAR

COMPLEXES USING PHASE-SELECTIVE FLUORESCENCE

CORRELATION AND COHERENCE SPECTROSCOPY

Approved: _____ _____
Dr. Andrew Marcus

When two or more fluorescent chromophores are closely spaced in a

macromolecular complex, dipolar coupling leads to delocalization of the excited states,

forming excitons. The relative transition frequencies and magnitudes are sensitive to

conformation, which can then be studied with optical spectroscopy. Non-invasive

fluorescence spectroscopy techniques are useful tools for the study of dilute

concentrations of such naturally fluorescent or fluorescently labeled biological systems.

This dissertation presents two phase-selective fluorescence spectroscopy techniques for

the study of dynamical processes in bio-molecular systems across a wide range of

timescales.

Polarization-modulated Fourier imaging correlation spectroscopy (PM-FICS) is a

novel phase-selective fluorescence spectroscopy for simultaneous study of translational and

conformational dynamics. We utilize modulated polarization and intensity gratings with phase-sensitive signal collection to monitor the collective fluctuations of an ensemble of fluorescent molecules. The translational and conformational dynamics can be separated and analyzed separately to generate 2D spectral densities and joint probability distributions. We present results of PM-FICS experiments on DsRed, a fluorescent protein complex. Detailed information on thermally driven dipole-coupled optical switching pathways is found, for which we propose a conformation transition mechanism.

2D phase-modulation electronic coherence spectroscopy is a third-order nonlinear spectroscopy that uses collinear pulse geometry and acousto-optic phase modulation to isolate rephasing and nonrephasing contributions to the collected fluorescence signal. We generate 2D spectra, from which we are able to determine relative dipole orientations, and therefore structural conformation, in addition to detailed coupling information. We present results of experiments on magnesium tetraphenylporphyrin dimers in lipid vesicle bilayers. The 2D spectra show clearly resolved diagonal and off-diagonal features, evidence of exciton behavior. The amplitudes of the distinct spectral features change on a femtosecond timescale, revealing information on time-dependent energy transfer dynamics.

This dissertation includes co-authored and previously published material.

CURRICULUM VITAE

NAME OF AUTHOR: Geoffrey Adam Lott

PLACE OF BIRTH: Cortland, NY

DATE OF BIRTH: July 3, 1980

GRADUATE AND UNDERGRADUATE SCHOOLS ATTENDED:

　　　University of Oregon
　　　University of Rochester

DEGREES AWARDED:

　　　Doctor of Philosophy, 2010, University of Oregon
　　　Master of Science, 2004, University of Oregon
　　　Bachelor of Science, 2002, University of Rochester

AREAS OF SPECIAL INTEREST:

　　　Ultrafast Spectroscopy
　　　Fluorescence Spectroscopy and Microscopy

PROFESSIONAL EXPERIENCE:

　　　Graduate Research Assistant, University of Oregon, 2004-2010

　　　Graduate Teaching Assistant, University of Oregon, 2002-2003, 2007-2010

GRANTS, AWARDS AND HONORS:

Harry W. Fulbright Prize, Department of Physics and Astronomy, University of Rochester, 2002

Degree Awarded with High Distinction, Department of Physics and Astronomy, University of Rochester, 2002

PUBLICATIONS:

Lott, G. A.; Senning, E. N.; Fink, M. C.; Marcus, A. H. I. Conformational dynamics of biological macromolecules by polarization-modulated Fourier imaging correlation spectroscopy. *J. Phys. Chem. B* **2009**, *113*, 6847-6853.

Senning, E. N.; Lott, G. A.; Fink, M. C.; Marcus, A. H. II. Kinetic pathways of switching optical conformations in DsRed by 2D Fourier imaging correlation spectroscopy. *J. Phys. Chem. B* **2009**, *113*, 6854-6860.

Tekavec, P. F.; Lott, G. A.; Marcus, A. H. Fluorescence-detected two-dimensional electronic coherence spectroscopy by acousto-optic phase modulation, *Ultrafast Phenomena XVI, Proceedings of the 16th International Conference*, Stresa, Italy, June 9 – 14, 2009, Springer: Heidelberg, 2009.

Senning, E. N.; Lott, G. A.; Marcus, A. H. Fourier imaging correlation spectroscopy for cellular structure-function. *Methods in Cell Biology* **2008**, *90*, 117-137.

Tekavec, P. F.; Lott, G. A.; Marcus, A. H. Fluorescence-detected two-dimensional electronic coherence spectroscopy by acousto-optic phase modulation. *J. Chem. Phys.* **2006**, *127*, 214307/1-214307/21.

ACKNOWLEDGMENTS

I would like to thank many people for their help and support during my time as a graduate student at the University of Oregon. First and foremost, I would like to thank my advisor Dr. Andrew Marcus, without whom the research contained within this dissertation would not be possible. His experimental creativity, scientific vision, and relentless optimism have all been indispensible to the success of the scientific endeavors contained here within, and my success as a graduate student. I would like to thank many members, past and present, from the Marcus Lab: Dr. Patrick Tekavec for teaching me the ins and outs of ultrafast lasers and interferometry; Dr. Eric Senning for collaborative efforts on the PM-FICS analysis and unquantifiable support; Dr. Michael Fink for taking the time to teach me the molecular FICS apparatus; all the other members of the lab during my time here – Dr. Michelle Knowles, Dr. Kenneth Adair, David Proctor, Aurelia Honerkamp-Smith, Chun-Mei Lin, James Utterback, and Jasper Cook.

I would like to thank members of the University who have directly contributed to the experimental apparatuses. Clifford Dax built many pieces of custom electronics that have been vital in the implementation of our novel experimental techniques. Dr. Lawrence Scatena provided an innumerable number of hours of assistance with optics and laser system issues. The machine shop staff, led by Kris Johnson, Dave Senkovich, and John Boosinger, has either directly built or assisted in building many crucial pieces of scientific machinery.

There are many teachers and mentors who played important roles in the journey to reach this point. Foremost, I would like to thank Mr. Hal Fuller for teaching physics in

an engaging and unconventional way in 12th grade, when I knew I was good at math and science, but didn't know what I wanted to do with those proficiencies.

Finally, I wish to thank my family and friends for their unconditional love and support, and for fostering my interest in science from a young age. Without their support, advice, and care, I could not have succeeded.

TABLE OF CONTENTS

LIST OF FIGURES

LIST OF TABLES

CHAPTER I

INTRODUCTION

Performing spectroscopic experiments on biological systems is a difficult

proposition. The use of fluorescent proteins as labels for tracking biological processes has

provided many new avenues for studies on biologically relevant systems, but the

experimental methods used are often limited in dynamic range, sensitivity, and

efficiency. The cellular environment is microscopic, easily photodegradable, and

optically dispersive due to the congested heterogeneous mixture of proteins, organelles,

lipid based membranes, cytoplasm, and other bio-molecular complexes. Due to these

obstacles, it is often useful to apply fluorescence detection based spectroscopic

techniques in an attempt to circumvent many of the difficulties that current methods face

in dealing with biological macromolecules. When using robust fluorophores, such

methods offer a means to generate contrast and enhance signal levels. Furthermore, by

combining phase-sensitive fluorescence detection with phase modulation of the exciting

laser fields, it is possible to obtain additional information while further increasing signal-

to-noise.[1-3] In this thesis, I describe the development of two fluorescence spectroscopy

methods to study structure and dynamics in biological systems. Two-dimensional phase-

modulation electronic coherence spectroscopy (2D PM-ECS) is an optical analog of 2D

magnetic resonance spectroscopy, and provides information about coupling between optical modes in biomolecular aggregates on femtosecond to picoseconds timescales. Polarization-modulation Fourier imaging correlation spectroscopy (PM-FICS)is a phase-selective approach to fluorescence fluctuation spectroscopy, and can be used to study the dynamics of biomolecular systems on time scales much longer than the fluorophore excited state lifetime.

The commercial availability of broadband laser systems has made the study of femtosecond dynamics over broad spectral ranges a vital technique for the determination of local structure and dynamics via coupling interactions in complex molecular systems. The most widely used ultrafast spectroscopic techniques for measuring nonlinear susceptibilities require the generation of a macroscopic polarization in the sample for signal detection, which therefore requires optically dense samples. We have developed the technique of 2D PM-ECS, a high signal-to-noise phase-selective fluorescence technique, to study the nonlinear susceptibilities in dilute systems from a sequence of four phase-related ultrafast laser pulses.

Techniques for measuring dynamics on timescales longer than the excited state lifetime (10^{-9} s) of molecular complexes also have inherent limitations. Techniques, such as fluorescence recovery after photo-bleaching (FRAP) and fluorescence correlation spectroscopy (FCS) are often limited by auto-fluorescence, narrow dynamic range, photo-bleaching due to high excitation intensities, and model-dependent interpretation of data.[4] To address these shortcomings, the phase-selective fluorescence detection technique of

PM-FICS has been developed to separate the spatial dynamics from internal dynamics, such as rotation and energy transfer, for a number of complex systems.

This thesis will focus heavily on the PM-ECS technique and its applications towards studying spectral fluctuations, with additional information about PM-FICS and its use as a tool for monitoring the conformational fluctuations of biological macromolecules. Throughout this dissertation we will use the convention that $\hbar = 1$ unless specifically noted.

Molecular Aggregates

Molecular aggregate complexes are ubiquitous in biological systems. Photosynthetic complexes of bacteriochlorophylls, for example, contain many chromophores which transfer excitation energy from an antenna site to a reaction center for photosynthesis with near 100% efficiency. Membrane-bound protein complexes are difficult to study using conventional NMR spectroscopy or x-ray crystallography, but have strongly coupled vibrational modes that are well suited for study by two-dimensional vibrational coherence spectroscopy.[5] There is a vast array of information that can be gleaned about the function of these systems using two-dimensional spectroscopic techniques, which will be described briefly in the following sections. Here, we will develop a qualitative understanding of how the electronic properties of individual labeled macromolecules are influenced by the formation of molecular aggregates in a membrane.

For the simplest case let us consider a system of two randomly oriented identical uncoupled monomers with a dipole-dipole dihedral angle of θ_{12} and a single optical

transition of frequency ω_0 as in Fig. 1.1A. In this case, the linear spectrum will show a

single transition. The solid black line in Fig. 1.1C shows the linear spectrum for a single

inhomogenously broadened transition in solution, centered at ω_0. If pairs of molecules

are separated by a very small distance, the resulting interaction leads to mixing of the

monomer electronics states into delocalized excitons. In the point dipole approximation,

the degenerate monomer excited electronic levels are split due to the interaction J,

described by the equation

$$\underset{\sim}{J} = \frac{\left(\underset{\sim}{\mu_1} \cdot \underset{\sim}{\mu_2}\right) - 3\left(\underset{\sim}{\mu_1} \cdot \hat{R}_{12}\right)\left(\underset{\sim}{\mu_2} \cdot \hat{R}_{12}\right)}{4\pi\varepsilon_o R_{12}{}^3}, \tag{1.1}$$

where the individual transition dipole vectors have magnitudes μ_i and the vector

connecting the dipoles has a magnitude of R_{12}. This coupling interaction determines the

magnitude of the splitting of the two resulting one-exciton energy levels, each of which is

shifted relative to the monomer frequency by the frequency $V_{12}/\hbar$, as shown in Fig.

1.1B. These so-called one-exciton states $|\pm\rangle = \frac{1}{\sqrt{2}}\left(|e_1\rangle \pm |e_2\rangle\right)$, are superpositions of the

uncoupled monomer states, with one of the monomers electronically excited and the

other unexcited. The two-exciton state $|f\rangle$ corresponds to both monomers

simultaneously electronically excited. The transition dipoles that access the two one-

exciton states $|\varepsilon_1\rangle$ and $|\varepsilon_2\rangle$ are determined by the linear combinations of the monomer

dipole moments, $\frac{1}{\sqrt{2}}\left(\underset{\sim}{\mu_1} \pm \underset{\sim}{\mu_2}\right)$. The linear spectrum for the inhomogeneously broadened

dimer sample, displayed as the dashed line in Fig. 1.1C, will be the sum of two inhomogeneously broadened Gaussian peaks, centered at frequencies shifted according to Eq. (1.1) from the monomer center frequency and with relative peak amplitudes that depend on the dihedral angle.
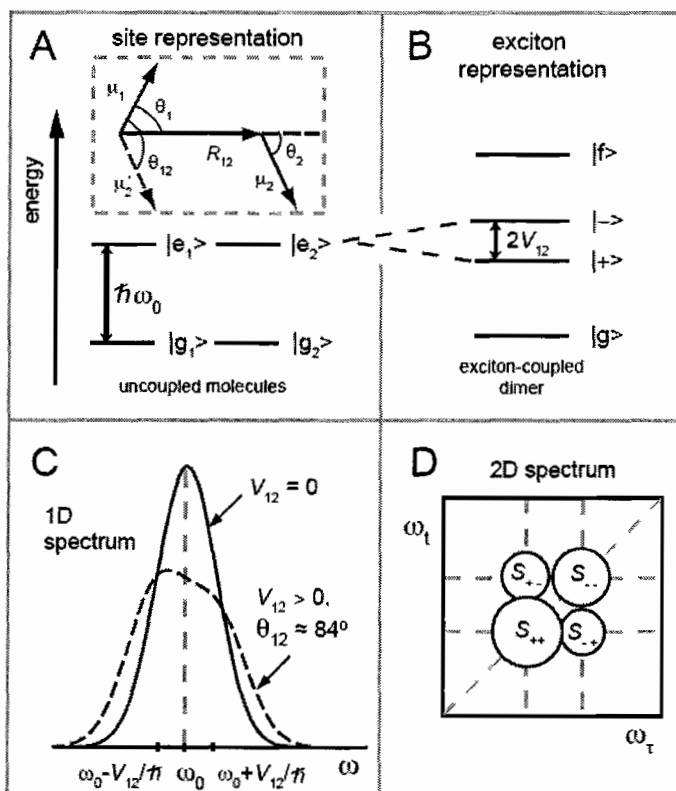
Figure 1.1: (A) Schematic of the electronic states of two identical two-level molecules, each with transition frequency ω_0. The inset shows the configuration and relative orientation of the two transition dipole moments. (B) The dipole-dipole interaction interaction V_{12}, from Eq. (1.1), results in a coupled dimer complex, with two non-degenerate one-exciton states and a single two-exciton state, f. (C) For uncoupled monomers, the 1D absorption spectrum shows a single inhomogeneously broadened feature (solid line). The dimer spectrum (dashed curve) shows additional structure due to the presence of two one-exciton transitions. Note that there is no contribution from the two-exciton state because it cannot be accessed with a single absorption/excitation interaction. (D) A simplified 2D frequency spectrum of a coupled dimer. Direct coupling information is accessible from the cross-peaks.

Two-Dimensional Spectroscopy

Two-dimensional spectroscopic techniques are useful for discerning information about local structure and dynamics that is not readily available from linear spectroscopy. Linear spectra are often congested and provide limited information on structure and dynamics, especially for molecular complexes in native environments. Linear spectroscopy can only access states by a single excitation event, determining limited structural information and no substantial information on coupling processes. Time-resolved 2D spectroscopy can yield detailed information about the coupling between monomer electronic states, and hence structural information about the configuration of interacting monomer dipole moments.

Just as it is advantageous to use fluorescence to separate signals from background, it is useful to analyze coupling processes via the off-diagonal cross peaks that exist in two-dimensional spectra, and which can be separated from linear background signals by virtue of their unique phase signatures. A typical 2D electronic spectrum, $\tilde{S}(\omega_{t_{21}}, T, \omega_{t_{43}})$, is a function of excitation and emission frequencies $\omega_{t_{21}}$ and $\omega_{t_{43}}$, respectively, and the so-called population time T.[6] The 2D spectrum yields information about how the detection frequency is affected by prior interactions at the excitation frequency. A simplified illustration of a 2D spectrum is shown in Fig. 1.1D. Designation of the feature labels S_{++}, S_{--}, etc, will be explained in chapter VI. Generally, there are diagonal and off-diagonal cross peaks in a two-dimensional spectrum. The off-diagonal features are of particular interest, as the presence of cross-peaks in a two-dimensional spectrum is direct evidence of coupling between distinct optical modes.[1-3,7-9] The features in the spectrum

may depend on the population time T, providing information about the timescales of coherent or incoherent coupling processes, optical dephasing, and individual transition frequency correlations.[6] Additionally, the sequence of pulses necessary to generate a 2D spectrum can traverse excited state absorption pathways which access the two-exciton states.

By extension of the ideas of 2D optical spectroscopy, we will use PM-FICS to examine slow dynamical processes associated with protein conformation by analysis of the 2D spectral density of polarized fluorescence fluctuations, and joint probability distributions. Similar to 2D-ECS, the 2D spectral density yields information pertaining to the correlation between two successive transition rates, separated by an adjustable time interval. Unlike PM-ECS, PM-FICS spectra reveal information about dynamics on much longer timescales ($10^{-3} - 10^2$ s). The 2D distribution functions provide information about the joint probability of observing displacements (in our case either center-of-mass translational or depolarization angle) during consecutive time intervals, which can contain detailed information about correlated conformational transitions of coupled dipole complexes.

Two-Dimensional Phase Modulation Electronic Coherence Spectroscopy

2D-ECS techniques are powerful methods for making phase-selective third-order spectroscopic measurements on coupled systems. These techniques are optical analogs of multi-dimensional NMR spectroscopy.[1-3] Specifically, these techniques are very useful for studying femto- and picosecond timescale transfer and coupling dynamics. The most

widely used ultrafast third-order spectroscopic method is four-wave mixing,[5,7,9] with a

simplified pulse diagram shown in Fig. 1.2A, in which a sequence of three pulses in a

noncollinear geometry with wavevectors $\vec{k}_1$, $\vec{k}_2$, and $\vec{k}_3$ interacts with a sample, creating

a distribution of coherences that result in fluorescence. The signals in the momentum

conserving rephasing, $-\vec{k}_1 + \vec{k}_2 + \vec{k}_3$, and non-rephasing, $\vec{k}_1 - \vec{k}_2 + \vec{k}_3$, wavevector

matching directions are detected on top of an attenuated fourth field (a well characterized

local oscillator field), preserving full phase and amplitude. These experiments have found

widespread use, but are not optimum for examining biological systems in realistic

conditions due to the necessity of generating a macroscopic polarization whose radiative

signal is collected in the wavevector matching directions. Additionally, there are more

stringent phase stability requirements as wavelengths get shorter, so many four-wave

mixing techniques that are well suited to vibrational spectra are not easily adaptable to

the visible wavelength range.

As an alternative method to four-wave mixing, we have developed the PM-ECS

technique to remove the requirement of a macroscopic polarization generated in the

sample. By utilizing a sequence of four collinear pulses, as seen in Fig. 1.2B, in

combination with an acousto-optic phase modulation technique, we are able to collect the

fluorescence resulting from this four pulse sequence, simultaneously isolating the

equivalent rephasing and non-rephasing contributions as difference and sum combination

frequencies of the relative phase sweeps applied to pulses 1 and 2, ϕ_{21}, and pulses 3 and

4, ϕ_{43}.
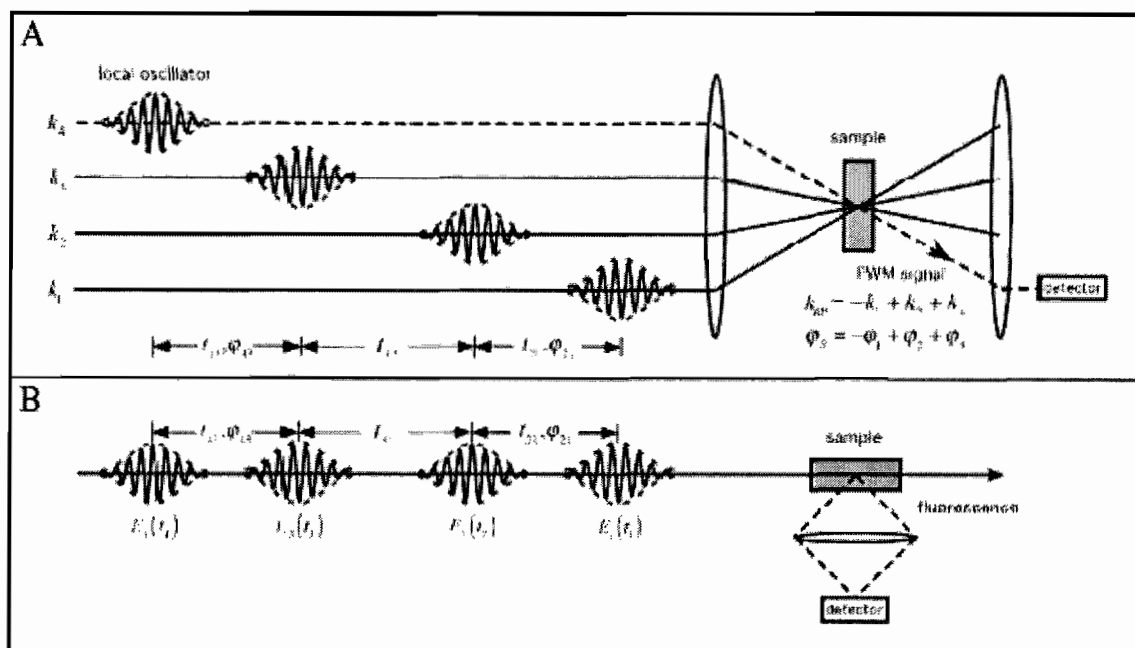
Figure 1.2: (A) Noncollinear pulse sequence for use in a four-wave mixing experiment. The signal due to the generated macroscopic polarization is shown to be collected in the rephasing direction. The non-rephasing signal contribution, not shown, may be collected in the appropriate direction after changing the pulse ordering. (B) A collinear pulse sequence for use in a 2D PM-ECS experiment is incident on a sample, and a portion of the resulting fluorescence is collected. Note that for both experimental geometries that there are three potentially variable time delays, between each set of successive pulses, and controllable relative phases between pulses 1 and 2, and pulses 3 and 4.

Fourier Imaging Correlation Spectroscopy

Experiments that probe fluorescence fluctuations of individual molecules, or the collective fluctuations of a finite population, are well suited to observe the slow (10^{-6} – several seconds) structural changes of biological macromolecules. Direct measurements of these fluctuations can reveal details of bio-molecular processes that are otherwise impossible to observe with ensemble-averaged measurements. Unfortunately, many single molecule measurements must deal with the difficulties of observing a low signal in

the presence of heterogeneity; for processes occurring on overlapping timescales, ambiguities can arise in attempting to separate internal from diffusive dynamics.

We will present the PM-FICS technique as a new tool for separating conformational dynamics from simultaneous diffusive motion. PM-FICS is a fluorescence imaging technique that probes the length-scale dependence of spatial fluctuations of an ensemble of fluorescently labeled macromolecules by exciting the ensemble with a phase and polarization modulated excitation fringe pattern. A large number ($N \sim 10^5$) of freely diffusing molecules in solution are excited by the fringe pattern. Fluctuations of the polarized steady-state emission are continuously monitored, and we are able to separately isolate the translational and optical anisotropy contributions. The PM-FICS technique utilizes the phase-selectivity of the approach to isolate a single Fourier component of the fluorescence signal to increase the signal-to-noise and accessible dynamic range of the technique at the expense of relatively unimportant spatial information of individual chromophores or chromophore complexes.

Outline

Chapter II discusses the theory for two-dimensional PM-ECS experiments, and contains co-authored material with P.F. Tekavec and A.H. Marcus. We start by defining the system Hamiltonian for a system with n indirectly coupled energy levels and define the time-resolved signals through perturbation theory and nonlinear response theory. Additionally, we display the method for transforming the collected data into two-dimensional spectra in the frequency domain.

Chapter III also contains co-authored material with P.F. Tekavec and A.H. Marcus. P.F. Tekavec designed the experimental apparatus and collected all data for this experiment. In this chapter we utilize the theory developed in chapter II to analyze the results from proof-of-principle experiments performed on atomic rubidium vapor, a model three-level system. Experimental and theoretically expected results will be compared in both the time and frequency domains.

Chapter IV introduces the PM-FICS technique, including material co-authored with E.N. Senning, M.C. Fink, and A.H. Marcus. Data was collected by M.C. Fink. Theory and results will be presented, showing that we are able to successfully separate translational dynamics from internal depolarization dynamics in DsRed, a fluorescent protein complex.

Chapter V expands upon the PM-FICS technique to four-point correlation functions, which can be displayed as two-dimensional spectra, analogous to 2D NMR. We utilize the spectra resulting from these experiments to measure rates of thermally driven conformation changes in the DsRed complex due to optical anisotropy fluctuations. Chapter V includes material co-authored by E.N. Senning, M.C. Fink, and A.H. Marcus. Data was collected by M.C. Fink.

Chapter VI adapts the 2D PM-ECS formalism developed in chapter II to coupled molecular systems in solution at room temperature. Specifically, we describe the expected theoretical results for dimeric systems and present experimental results on self-forming magnesium tetraphenylporphyrin (MgTPP) complexes in lipid bilayer vesicles. This chapter contains material co-authored J. Utterback and A.H. Marcus.

CHAPTER II

THEORY OF TWO-DIMENSIONAL PHASE-MODULATION ELECTRONIC

COHERENCE SPECTROSCOPY FOR MONOMERIC SYSTEMS

This chapter examines the theoretical treatment of two-dimensional phase

modulation electronic coherence spectroscopy (2D PM-ECS) for experiments performed

on monomeric systems. This is an extension of the wave packet interferometry formalism

developed by J.A. Cina[1] and T.S. Humble[2] to include phase modulation. This formalism

is essential to the understanding of the experiments described in chapter III, and will

provide the base for the theory expanded upon and utilized in chapter VI. This chapter

contains co-authored material with P.F. Tekavec and A.H. Marcus.

In a 2D PM-ECS experiment, a sequence of four laser pulses is collinearly

incident on a system. This sequence of pulses leads to a multitude of overlaps on the

excited state manifold. We isolate the overlaps that occur between superposition states

generated by one-pulse and three-pulse coherent contributions. These contributions

contain free evolution on the ground and excited states in the intervening periods between

field-matter interactions, and impulsive transitions between ground and excited states at

pulse incidence. These overlaps create excited state populations that generate a

fluorescence signal[3-10] with a time-varying phase dependent on characteristic features of both the laser fields and electronic structure of the sample itself.

This sequence of interactions and resultant fluorescence is a function of two interpulse delays, t_{43} and t_{21} (interchangeably referred to as t and τ, the detection time and coherence time, respectively), the time delays between pulses 3 & 4 and pulses 1 & 2, respectively. The third relevant time delay, t_{32} (interchangeably referred to as T, the population time) is held fixed for a single experiment. By varying t_{32} over a series of experiments, information about the evolution of features in the 2D spectra as a function of t_{32} is collected.[11]

Finally, we determine the third-order susceptibilities resulting from the interactions of the laser pulses with the electric dipole moments of the system and its excited state manifold. We establish the dependency of the results based on the pulse and sample parameters, finding a time-dependence due to the population time, pulse phases (ϕ_1, ϕ_2, ϕ_3, and ϕ_4), and the transition frequencies between the ground and n^{th} electronic excited state (ω_{ng}).

Electric Field of a Four Pulse Sequence

The total electric field, $E(t)$, of a sequence of four parallel polarized laser pulses utilized in a 2D PM-ECS experiment can be written as the sum of the four individual pulse electric fields $E(t) = E_1(t) + E_2(t) + E_3(t) + E_4(t)$, where the field of the jth pulse ($j \in \{1, 2, 3, 4\}$) is defined as

$$E_j(t) \equiv A_j(t-t_j)\cos\left[\gamma_j(t-t_j)\right]. \tag{2.1}$$

In Eq. (2.1), $A_j(t)$ is the temporal envelope, t_j is the pulse arrival time, and $\gamma_j(t)$ is the temporal phase function

$$\gamma_j(t) = \omega_L t + \phi_j. \tag{2.2}$$

In Eq. (2.2), ω_L $(= 2\pi\nu_L)$ is the laser center frequency and ϕ_j is a constant phase. A diagram of this four pulse sequence is shown in Fig. 2.1. We obtain the frequency-dependent expression for the pulse electric field from the Fourier transform of Eq. (2.1),

$$\hat{E}_j(\omega) = \tfrac{1}{2}\int_{-\infty}^{\infty} A_j(t-t_j)e^{-i\gamma_j(t-t_j)}e^{i\omega t}\,dt + \tfrac{1}{2}\int_{-\infty}^{\infty} A_j(t-t_j)e^{i\gamma_j(t-t_j)}e^{i\omega t}\,dt$$

$$= \hat{E}_j^{(+)}(\omega) + \hat{E}_j^{(-)}(\omega). \tag{2.3}$$

In Eq. (2.3), we define the forward-rotating and counter-rotating spectral Fourier components of the jth pulse, $\hat{E}_j^{(+)}(\omega)$ and $\hat{E}_j^{(-)}(\omega)$ respectively. These functions have explicit forms

$$\hat{E}_j^{(+)}(\omega) = \alpha_j(\omega)e^{i\omega t_j}e^{-i\phi_j} \tag{2.4}$$

and

$$\hat{E}_j^{(-)}(\omega) = \alpha_j(-\omega)e^{i\omega t_j}e^{i\phi_j}, \qquad (2.5)$$

where $\alpha_j(\omega)$ is the spectral amplitude and ϕ_j is the spectral phase of the jth pulse. For

the Fourier transform limited pulses considered here, the spectral phase is a constant,

equal to the temporal phase.
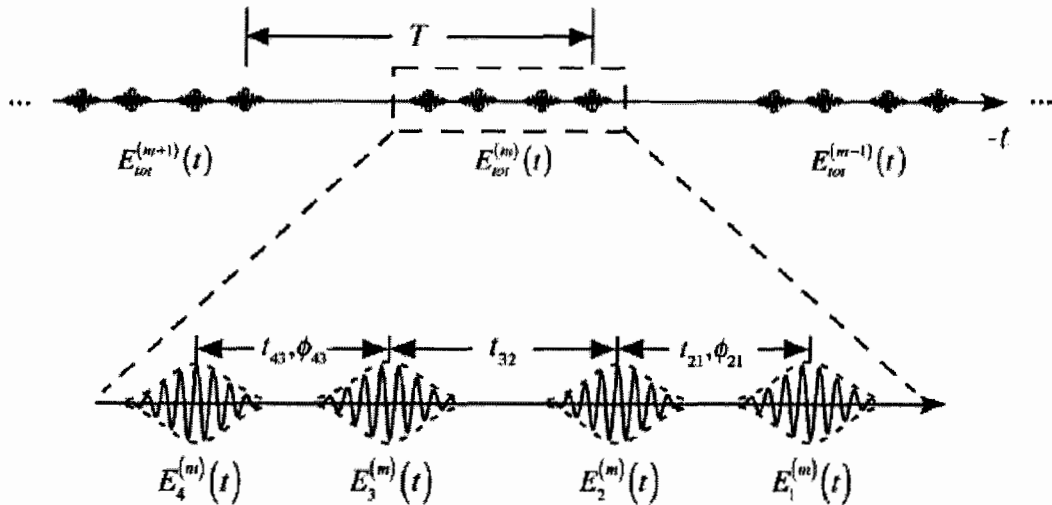
Figure 2.1: Illustration of a train of four sequential phase-modulated pulses. Each pulse sequence is labeled by the superscript m; the individual pulses are labeled by the subscripts 1 – 4. A pulse sequence is characterized by the interpulse delays $t_{21} = t_2 - t_1$, $t_{32} = t_3 - t_2$, and $t_{43} = t_4 - t_3$, and the relative temporal phases $\phi_{21} = \phi_2 - \phi_1$ and $\phi_{43} = \phi_4 - \phi_3$.

Hamiltonian of an 'n' Excited State Monomeric System

To fully describe the interaction of the previously defined pulse sequence with a monomeric system, we use knowledge of the system Hamiltonian and third-order perturbation theory to determine the excited state population after the four field-matter interactions.

The time-dependent Hamiltonian operator is defined as

$$\underset{\sim}{H}(t) = \underset{\sim}{H}_0 + \underset{\sim}{V}(t),\tag{2.6}$$

where $\underset{\sim}{H}_0$ is the Hamiltonian in the absence of an interaction and $\underset{\sim}{V}(t)$ is the time-dependent potential due to the perturbative action of the laser fields. In the unperturbed eigenbasis, the Hamiltonian is defined as

$$\underset{\sim}{H}_0 = \varepsilon_g |g\rangle\langle g| + \sum_n \varepsilon_n |n\rangle\langle n|,\tag{2.7}$$

with ε_g being the energy of the ground state and ε_n the energy of the nth excited electronic energy level as shown in Fig. 2.2. The perturbation contribution to the Hamiltonian is given by the electric dipole approximation

$$\underset{\sim}{V}(t) = -\underset{\sim}{\mu}E(t),\tag{2.8}$$

where $\underset{\sim}{\mu}$ is the transition dipole moment operator that couples the ground and n^{th} excited electronic energy levels,

$$\underset{\sim}{\mu} = \sum_n |n\rangle \mu_{ng} \langle g |,$$

(2.9)

where $\mu_{ng} = \mu_{gn}^*$. In Eq. (2.9) we have made the assumption that the energy level spacing between excited electronic energy levels is small compared to that between the ground and excited electronic energy levels, and is therefore non-resonant, making the transition dipole moments $\mu_{nn'} = 0$ ($n \neq n'$) with respect to the excitation fields.
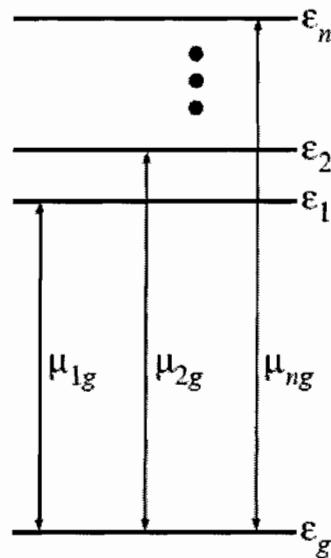
Figure 2.2: Energy level diagram for a system with one common ground state and n electronic excited states. Transition dipole matrix elements between the ground state and excited states are labeled next to the relevant arrow.

Third Order Time-Dependent Perturbation Theory

We describe the interaction of the four pulses with the system by working in the interaction picture and utilizing perturbation theory.[12-13] To work in the interaction picture instead of the Schrödinger picture, as we have until now, we use the transformations

$$\left|\psi^I(t)\right\rangle = e^{iH_0 t}\left|\psi^S(t)\right\rangle \tag{2.10}$$

and

$$\underset{\sim}{V}^I(t) = e^{iH_0 t}V^S(t)e^{-iH_0 t}, \tag{2.11}$$

where the interaction picture and Schrödinger picture operators are denoted by the superscripts I and S, respectively. The temporal evolution of the system in the interaction picture is given by the equation of motion

$$\frac{i\partial\left|\psi^I(t)\right\rangle}{\partial t} = \underset{\sim}{V}^I(t)\left|\psi^I(t)\right\rangle, \tag{2.12}$$

which one will notice is similar to the Schrödinger picture equation of motion with $\underset{\sim}{H}$ replaced by $\underset{\sim}{V}^I(t)$. This means that the state ket is fixed in time in the absence of the potential $\underset{\sim}{V}^I(t)$. For a small (perturbative) potential, this equation has the solution

$$\left|\psi^I(t)\right\rangle \cong \left|\psi^I_{(0)}(t)\right\rangle + \left|\psi^I_{(1)}(t)\right\rangle + \left|\psi^I_{(2)}(t)\right\rangle + \left|\psi^I_{(3)}(t)\right\rangle, \tag{2.13}$$

where the numerical subscripts denote the order of the interaction with $V^I(t)$. This solution is a Dyson series with the individual terms, up to third order, having the forms

$$\left|\psi^I_{(0)}(t)\right\rangle = \left|g\right\rangle, \tag{2.14}$$

$$\left|\psi^I_{(1)}(t)\right\rangle = -i\int_{-t_0}^{t} dt' \underset{\sim}{V}^I(t')\left|g\right\rangle, \tag{2.15}$$

$$\left|\psi^I_{(2)}(t)\right\rangle = \int_{-t_0}^{t} dt' \int_{-t_0}^{t'} dt'' \underset{\sim}{V}^I(t')\underset{\sim}{V}^I(t'')\left|g\right\rangle, \tag{2.16}$$

$$\left|\psi^I_{(3)}(t)\right\rangle = -i\int_{-t_0}^{t} dt' \int_{-t_0}^{t'} dt'' \int_{-t_0}^{t''} dt''' \underset{\sim}{V}^I(t')\underset{\sim}{V}^I(t'')\underset{\sim}{V}^I(t''')\left|g\right\rangle, \tag{2.17}$$

for a state initially in its ground state, $\left|g\right\rangle = \left|\Psi^I(t_0)\right\rangle$.

The zero and second order terms do not contribute to fluorescence, as they are ground state terms. The first order and third order terms create populations on the excited states, contributing to the fluorescence signal. By assuming that the system is in the ground state before the first laser pulse is incident and the state of the system is measured long after the fourth pulse, we can set the lower and upper limits of integration to

negative and positive infinity, respectively. Invoking the rotating wave approximation for rapidly oscillating terms,[12] the third order superposition state is

$$\left|\psi_{mlk}(t)\right\rangle = -i\int_{-\infty}^{\infty}dt'\int_{-\infty}^{t'}dt''\int_{-\infty}^{t''}dt'''\underset{\sim}{\mu^I}(t')\underset{\sim}{\mu^I}(t'')\underset{\sim}{\mu^I}(t''')E_m(t')E_l(t'')E_k(t''')\left|g\right\rangle. \qquad (2.18)$$

The subscripts designate this as a superposition state formed on the electronic excited state manifold due to the interactions with pulses k, l, and m where $k,l,m \in \{1,2,3,4\}$. More explicitly, this is a superposition state caused by excitation from the ground state to the electronic excited manifold by pulse k, followed by de-excitation back to the ground state by pulse l, and excitation to the excited state manifold once again by pulse m.

Generally, for a sequence of pulses the indices k, l, and m may repeat, meaning that a single pulse interacts with the sample multiple times, as long as the indices maintain proper time ordering. This reduces the indices to four separate cases for consideration: case i, where a single pulse interacts with the sample three times, $k=l=m$; case ii, where a single pulse interacts with the sample twice prior to a second pulse interacting with the sample, case iii, $k=l\neq m$; where a pulse interacts with a sample once and a subsequent pulse interacts with the sample twice, $k\neq l=m$; and case iv, where three separate pulses interact a single time with the sample, $k\neq l\neq m$. We require the pulses to act in a time-ordered manner such that $t_1\leq t_2\leq t_3\leq t_4$, and therefore $k\leq l\leq m$, where t_i is the arrival time of the ith pulse. Additionally, we make the approximation that the pulses act in the impulsive limit, ignoring the effects of pulse overlap and allowing us to approximate

$|\psi_{mlk}(t)\rangle$ as a product of three independent Fourier transforms. We thus extend the remaining upper limits of intergration in Eq. (2.18) to infinity.

Since we are interested only in the terms linear in each of the excitation fields, we will only be interested in the terms generated in case *iv*. These terms are given as $|\psi_{321}(t)\rangle, |\psi_{421}(t)\rangle, |\psi_{431}(t)\rangle$, and $|\psi_{432}(t)\rangle$ (for *k≠l≠m*), which will create an overlap that is linear in each of the four fields when combined with the appropriate one-pulse contribution from the jth pulse. In conjunction with this information, we use Eq. (2.18) along with Eqs. (2.3) – (2.5), (2.8), (2.9) to find

$$
\begin{aligned}
|\psi_{mlk}(t)\rangle &= i\int_{-\infty}^{\infty}dt'\int_{-\infty}^{\infty}dt''\int_{-\infty}^{\infty}dt'''\sum_{a,b}\mu_{ag}\mu_{gb}\mu_{bg}e^{i\omega_{ag}t'}e^{-i\omega_{gb}t''}e^{i\omega_{bg}t'''}E_m(t')E_l(t'')E_k(t'')|a\rangle \\
&\cong i\sum_{a,b}\mu_{ag}\mu_{bg}^2\hat{E}_m^{(-)}(\omega_{ag})\hat{E}_l^{(+)}(-\omega_{bg})\hat{E}_k^{(-)}(\omega_{bg})|a\rangle \\
&= i\sum_{a,b}\mu_{ag}\mu_{bg}^2\alpha_m(\omega_{ag})\alpha_l(-\omega_{bg})\alpha_k(\omega_{bg})e^{i\omega_{ag}t_m+i\omega_{bg}(t_l-t_k)}e^{-i(\phi_m-\phi_l+\phi_k)}|a\rangle,
\end{aligned}
\tag{2.19}
$$

where $a,b\in\{1,2,...,n\}$. It can similarly be shown that a one-pulse contribution takes the form

$$
|\psi_j(t)\rangle = i\sum_{n}\mu_{ng}\alpha_j(\omega_{ng})e^{i\omega_{ng}t_j}e^{-i\phi_j}|n\rangle .
\tag{2.20}
$$

Transitions from the ground state to an excited electronic state involve positive frequencies and transitions from an excited electronic state to the ground state involve negative frequencies. The rotating wave approximation leaves only the $\hat{E}^{(-)}(\omega)$ component for positive frequency transitions and the $\hat{E}^{(+)}(\omega)$ component of the excitation field for negative frequency transitions. The pulse-imparted phase of this state follows the same rules – a positive phase contribution for upwards transitions and a negative phase contribution for downward transitions. In the following sections we demonstrate how this phase information is employed to isolate fluorescence contributions that are linear in each of the four laser fields.

Quadrilinear Overlaps and Populations

The total amplitude on the electronic excited state manifold after the sequence of four laser pulses is a sum of the one-pulse and three-pulse contributions,

$$|\psi(t \gg t_4)\rangle = \sum_{j=1}^{4} |\psi_j(t)\rangle + \sum_{m>l>k\in\{1,2\}}^{4} |\psi_{mlk}(t)\rangle. \tag{2.21}$$

The population on the excited state manifold is given by the inner product of Eq. (2.21) with itself,

$$\langle\psi(t \gg t_4)|\psi(t \gg t_4)\rangle \cong \sum_{j,j'=1}^{4} \langle\psi_j|\psi_{j'}\rangle + \sum_{\substack{m>l>k=1 \\ j=1}}^{4} \left(\langle\psi_j|\psi_{mlk}\rangle + \langle\psi_{mlk}|\psi_j\rangle\right). \tag{2.22}$$

We have dropped the explicit time dependence on the right hand side of the equation for brevity. The first term on the right hand side of Eq. (2.22) is the linear contribution to the signal and the second term is the third order contribution. Additionally, there is a fifth-order contribution to the overall signal (sixth-order in the fields), but it is comparatively negligible. As stated above, we are only interested in the terms linear in each of the four signal fields. These quadrilinear terms are those in which there is an interference between one of the three-pulse superposition states with a one-pulse contribution. These overlaps are represented as $\langle \psi_j | \psi_{mlk} \rangle$ and their respective conjugates in Eq. (2.22). They can be determined from Eq. (2.19) and Eq. (2.20) to be

$$\langle \psi_{432} | \psi_1 \rangle = \sum_{a,b} \mu_{ag}^2 \mu_{bg}^2 \alpha^2 (\omega_{ag}) \alpha^2 (\omega_{bg}) e^{-i(\omega_{ag} t_{43} + \omega_{ag} t_{21} + (\omega_{ag} - \omega_{bg}) t_{32})} e^{i(\phi_{43} + \phi_{21})} , \qquad (2.23)$$

$$\langle \psi_{431} | \psi_2 \rangle = \sum_{a,b} \mu_{ag}^2 \mu_{bg}^2 \alpha^2 (\omega_{ag}) \alpha^2 (\omega_{bg}) e^{-i(\omega_{ag} t_{43} - \omega_{bg} t_{21} + (\omega_{ag} - \omega_{bg}) t_{32})} e^{i(\phi_{43} - \phi_{21})} , \qquad (2.24)$$

$$\langle \psi_{421} | \psi_3 \rangle = \sum_{a,b} \mu_{ag}^2 \mu_{bg}^2 \alpha^2 (\omega_{ag}) \alpha^2 (\omega_{bg}) e^{-i(\omega_{ag} t_{43} - \omega_{bg} t_{21})} e^{i(\phi_{43} - \phi_{21})} , \qquad (2.25)$$

$$\langle \psi_4 | \psi_{321} \rangle = \sum_{a,b} \mu_{ag}^2 \mu_{bg}^2 \alpha^2 (\omega_{ag}) \alpha^2 (\omega_{bg}) e^{-i(\omega_{ag} t_{43} + \omega_{bg} t_{21})} e^{i(\phi_{43} + \phi_{21})} , \qquad (2.26)$$

for $a, b \in \{1, 2, ..., n\}$. Here we have defined $\phi_{21} = \phi_2 - \phi_1$ and $\phi_{43} = \phi_4 - \phi_3$. It is useful to recall that the phase contribution from a transition from the ground state to an excited state on the bra side is negative while on the ket side it is positive. Eqs. (2.23) − (2.26) reveal that the first and fourth overlaps have the same phase factor imparted to them by the four pulse sequence, as do the second and third overlaps. This allows us to separate the third-order population into two phase-distinct contributions - $2\,\mathrm{Re}\{\langle \psi_{432} | \psi_1 \rangle + \langle \psi_4 | \psi_{321} \rangle\}$, with a phase of $i(\phi_{43} + \phi_{21})$, and $2\,\mathrm{Re}\{\langle \psi_{431} | \psi_2 \rangle + \langle \psi_{421} | \psi_3 \rangle\}$, with a phase of $i(\phi_{43} - \phi_{21})$. We refer to these phases as occurring at the sum and difference frequency, respectively.

Pulse Interaction Diagrams

We represent the four general wave packet pathways that lead to nonlinear signals in a simple three level model system using the pulse ladder diagrams in Fig. 2.3. These diagrams, which are similar in spirit to Feynman diagrams, are useful bookkeeping tools to visually represent the eigenstate pathways and their associated phases as defined in equations (2.23) − (2.26). In these diagrams, vertical arrows represent transitions between energy levels due to pulse interactions at the times t_1, t_2, t_3, and t_4. Horizontal arrows represent free evolution on the associated state between pulse interactions. Gray and white arrows designate actions by third-order and first-order wave packets, respectively. In the context of the atomic rubidium experiments of chapter III, the term 'wave packet' refers to a superposition of excited states, while in chapter VI 'wave packet' refers to a

molecular wave packet evolving on a potential energy surface. Above each vertical arrow we indicate the phase imparted to the wave packet by interaction with the respective pulses. For these phases we adopt the conventions for the ket (bra) side that upward (downward) transitions acquire a negative (positive) phase and downward (upward) transitions acquire a positive (negative) phase. Additionally, the phase accumulated during free evolution is positive for kets and negative for bras, as defined in Eq. (2.12). We define the difference between pulse pair phase factors as $\phi_{ij} = \phi_i - \phi_j$. For example, Fig. 2.3A shows the pulse phase accumulated from the overlap $\langle \psi_{432} | \psi_1 \rangle$. The upward transitions on the bra side of the overlap, pulses 2 and 4, impart positive phases $i\phi_2$ and $i\phi_4$, respectively, while the upward transition on the ket side (pulse 1) and the downward transition on the bra side (pulse 3) impart negative phases $i\phi_1$ and $i\phi_3$, respectively. These phases combine as $i\phi_4 - i\phi_3 + i\phi_2 - i\phi_1 = i\phi_{43} + i\phi_{21}$, a sum reference phase signature. From these diagrams it is evident that the four non-linear populations depend on the laser pulse phase according to $\langle \psi_{432} | \psi_1 \rangle \sim e^{i(\phi_{43} + \phi_{21})}$, $\langle \psi_4 | \psi_{321} \rangle \sim e^{i(\phi_{43} + \phi_{21})}$, $\langle \psi_{431} | \psi_2 \rangle \sim e^{i(\phi_{43} - \phi_{21})}$, and $\langle \psi_{421} | \psi_3 \rangle \sim e^{i(\phi_{43} - \phi_{21})}$, as further demonstration of the sum, $\phi_{43} + \phi_{21}$, and difference, $\phi_{43} - \phi_{21}$, relative phase factor associations.

One may note that these 'sum' and 'difference' terms satisfy identical momentum conservation conditions as the non-rephasing and rephasing signals collected in four-wave mixing experiments using non-collinear excitation geometries[11,14-24] and phase-cycling techniques that utilize collinear geometry.[3-7] These rephasing and non-rephasing designations can be understood when considering the sum and difference terms

separately in Fig. 2.3. The difference terms evolve on Hermitian conjugate pathways during the time delays t_{21} and t_{43}, satisfying the rephasing, "echo" condition.[12] Conversely, the sum terms evolve on non-conjugate pathways during the same time intervals, consistent with the non-rephasing condition.

Each of the general diagrams in Fig. 2.3 has four separate, distinct eigernstate pathways that contribute to it. In Fig. 2.4 we display the four pathways that contribute to an example system with two excited electronic levels ($n = 2$) for the general overlap in Fig. 2.3B, corresponding to $\langle \psi_{431} | \psi_2 \rangle$. For a system with n excited states, there will be n^2 distinct eigenstate pathways. We display the phases accumulated during each of the periods of free evolution and the amplitude associated with the transitions between ground and excited state due to the transition dipole strengths, maintaining prior phase and evolution conventions. In the first two panels, Fig 2.4A and 2.4B, there are interactions between the ground and a single excited state ($|g\rangle \leftrightarrow |2\rangle$ and $|g\rangle \leftrightarrow |1\rangle$, respectively). These are single mode contributions, which lead to diagonal features in the third-order susceptibility. The latter two panels, Fig. 2.4C and 2.4D, involve transitions between the ground state and each of the excited states. These pathways involve a ground-state mediated transition between the two distinct excited states, which leads to contributions to off-diagonal features in the resulting non-linear spectra. The explicit pathway contributions for the remaining three quadrilinear overlaps are shown in Figs. 2.5 – 2.7.
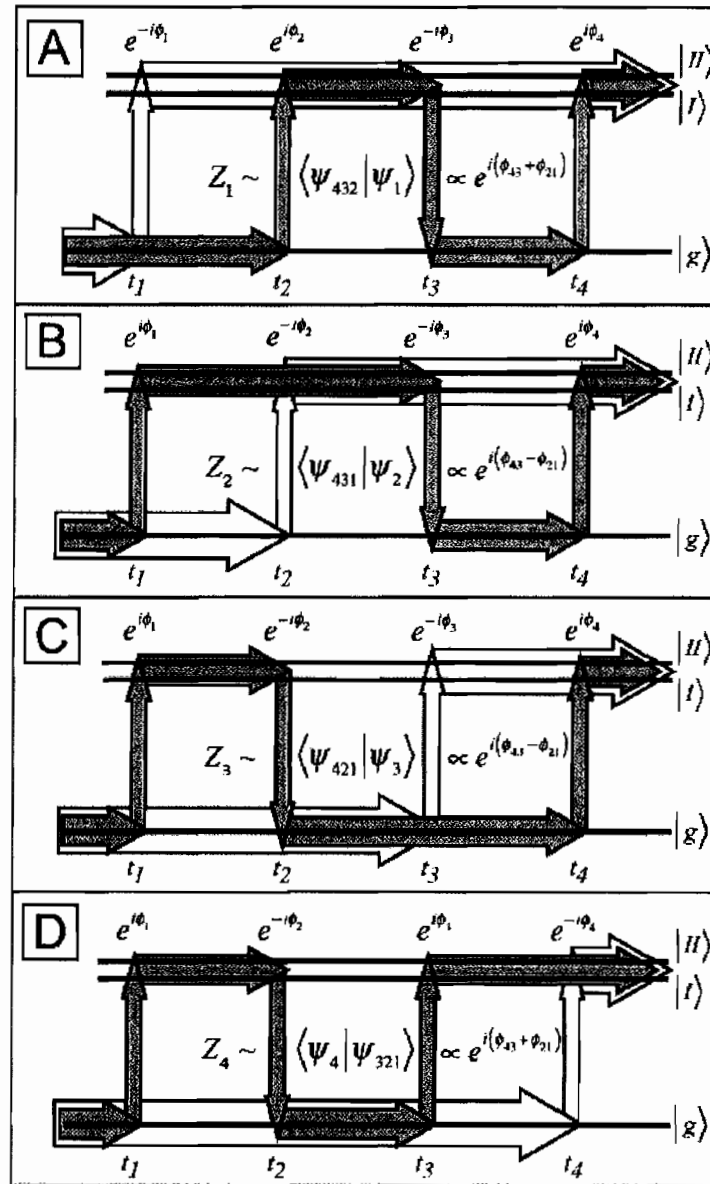
Figure 2.3: Wave packet pathway diagrams for the four non-linear population terms isolated by PM-ECS (described in text). Separate panels illustrate the pathways for (a) $Z_1 \propto \langle \psi_{432} | \psi_1 \rangle$, (b) $Z_2 \propto \langle \psi_{431} | \psi_2 \rangle$, (c) $Z_3 \propto \langle \psi_{421} | \psi_3 \rangle$, and (d) $Z_4 \propto \langle \psi_4 | \psi_{321} \rangle$. The overlaps described in panels (a) and (d) contribute to our 'sum-signal,' and the overlaps described in panels (b) and (c) contribute to our 'difference-signal.' This is a general diagram for any number of excited states, regardless of the fact that there are two labeled.
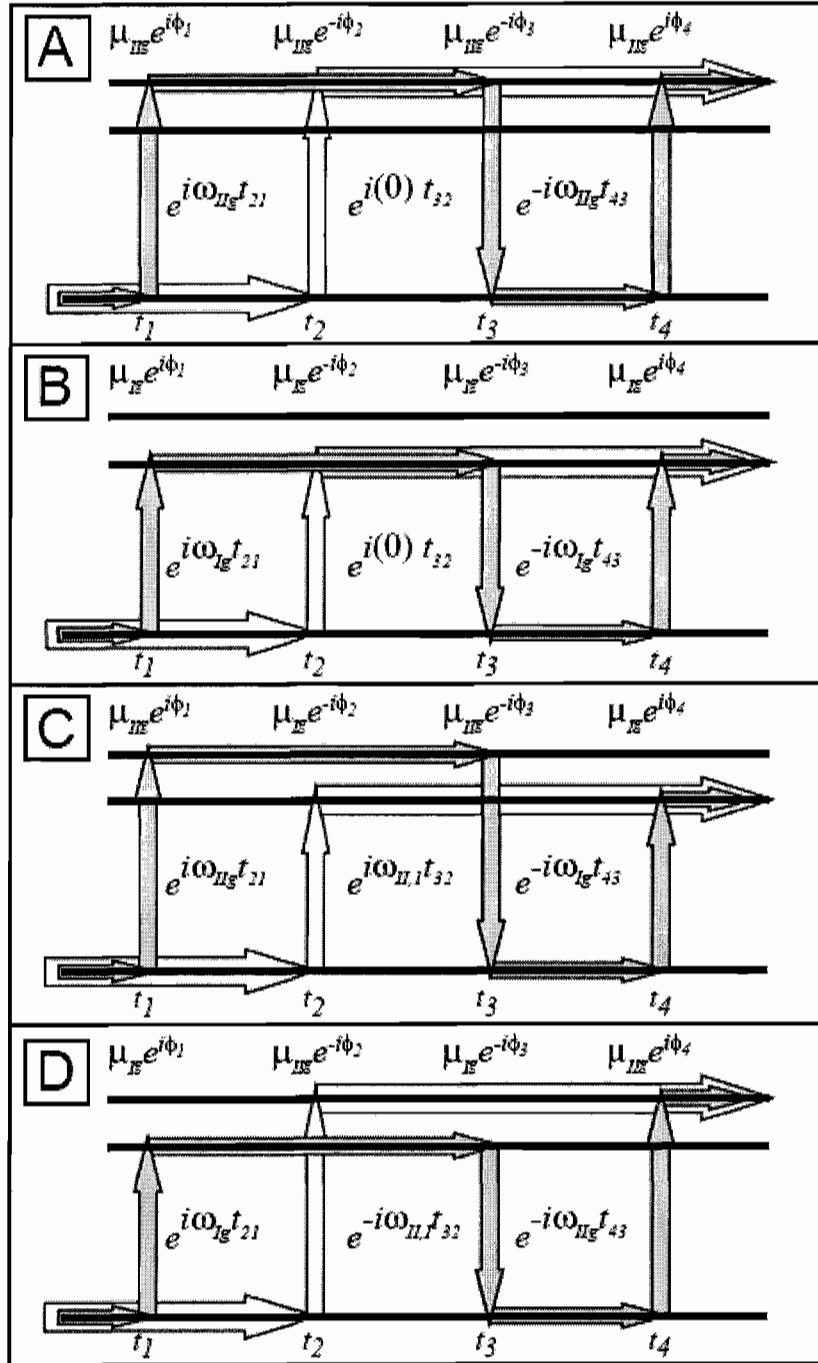
Figure 2.4: Diagrams illustrating the four distinct wave packet pathways that contribute to the $\langle \psi_{431} | \psi_2 \rangle$ overlap in a three-level system (described in text). The pathways depicted in panels (A) and (B) are 'single mode' pathways, while those depicted in panels (C) and (D) are 'coupling' pathways.
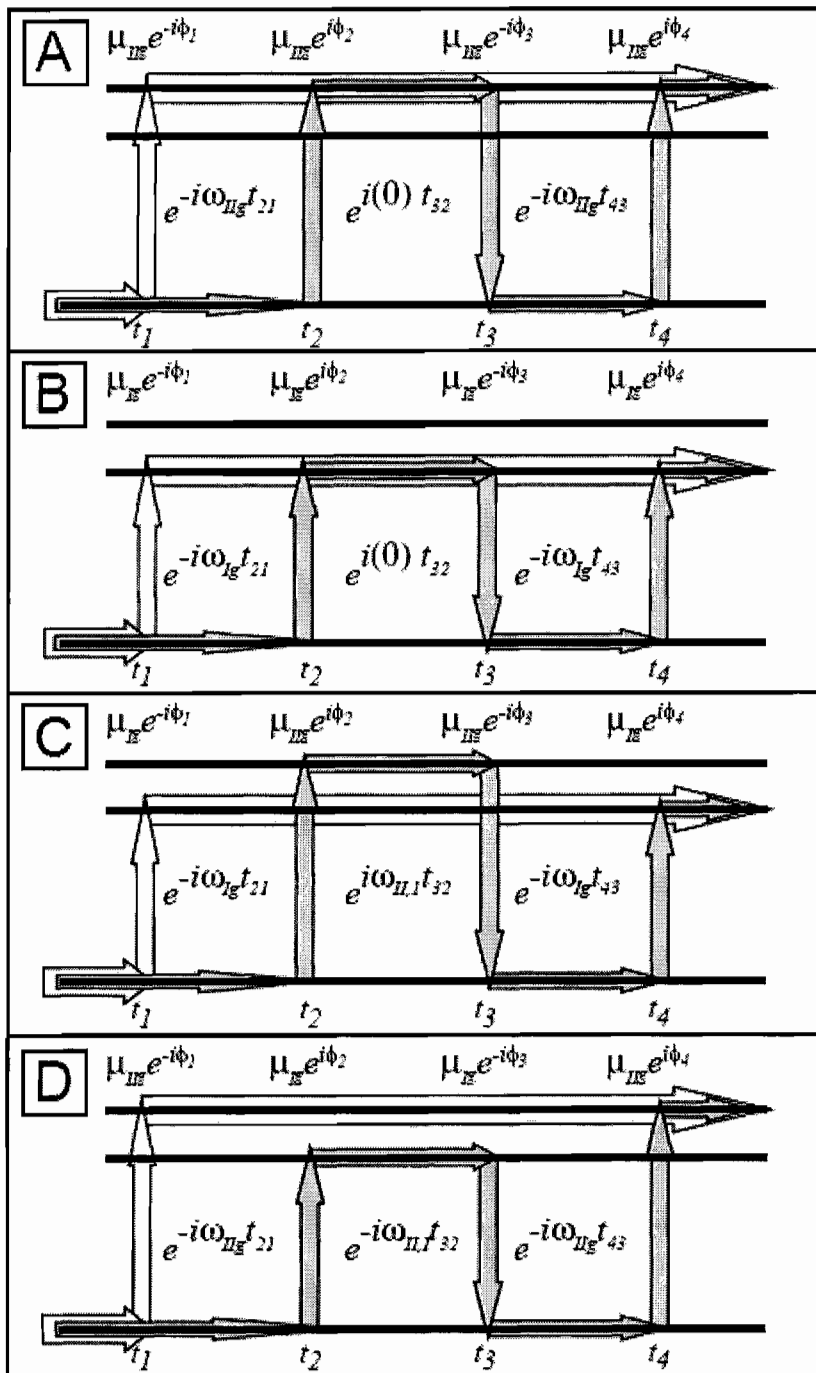
Figure 2.5: Diagrams illustrating the four distinct wave packet pathways that contribute to the $\langle \psi_{432} | \psi_1 \rangle$ overlap in a three-level system. The pathways depicted in panels (A) and (B) are 'single mode' pathways, while those depicted in panels (C) and (D) are 'coupling' pathways.
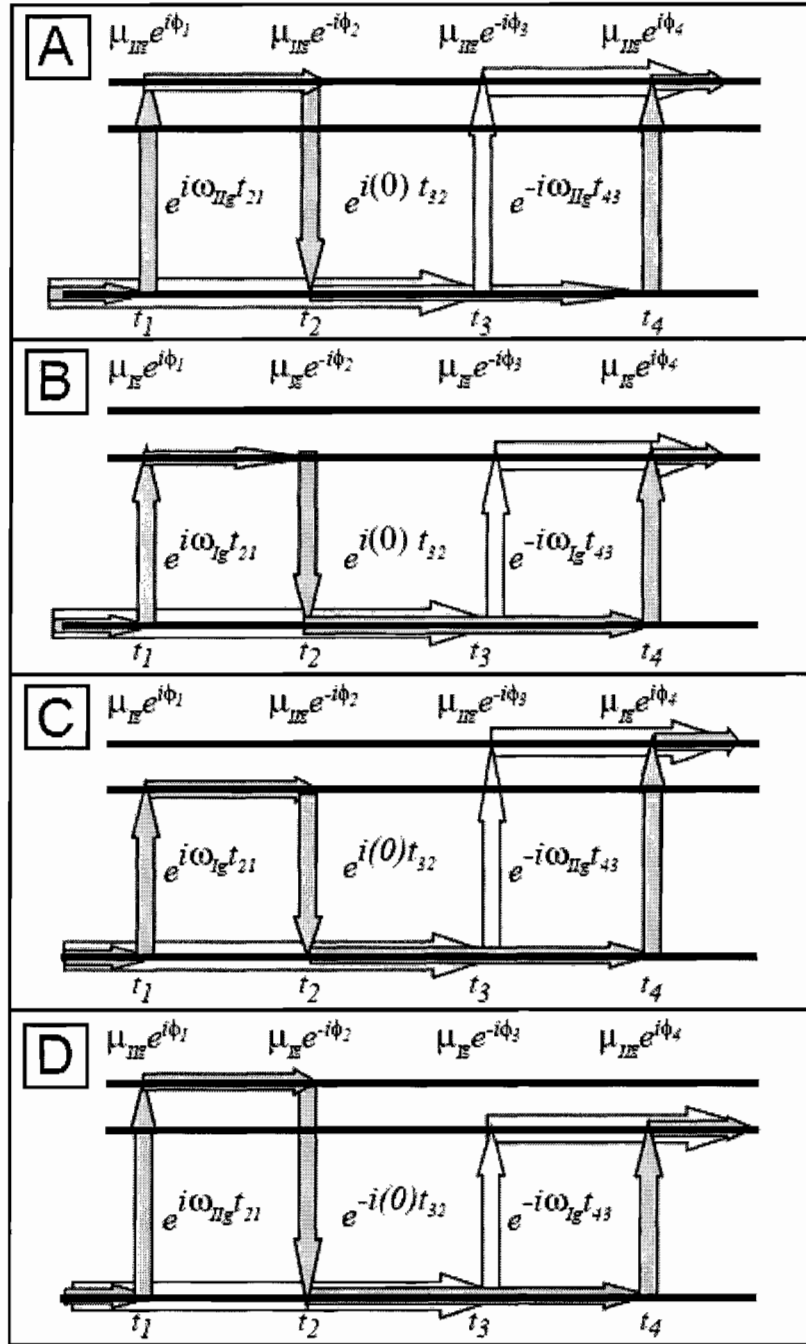
Figure 2.6: Diagrams illustrating the four distinct wave packet pathways that contribute to the $\langle \psi_{421} | \psi_3 \rangle$ overlap in a three-level system. The pathways depicted in panels (A) and (B) are 'single mode' pathways, while those depicted in panels (C) and (D) are 'coupling' pathways.
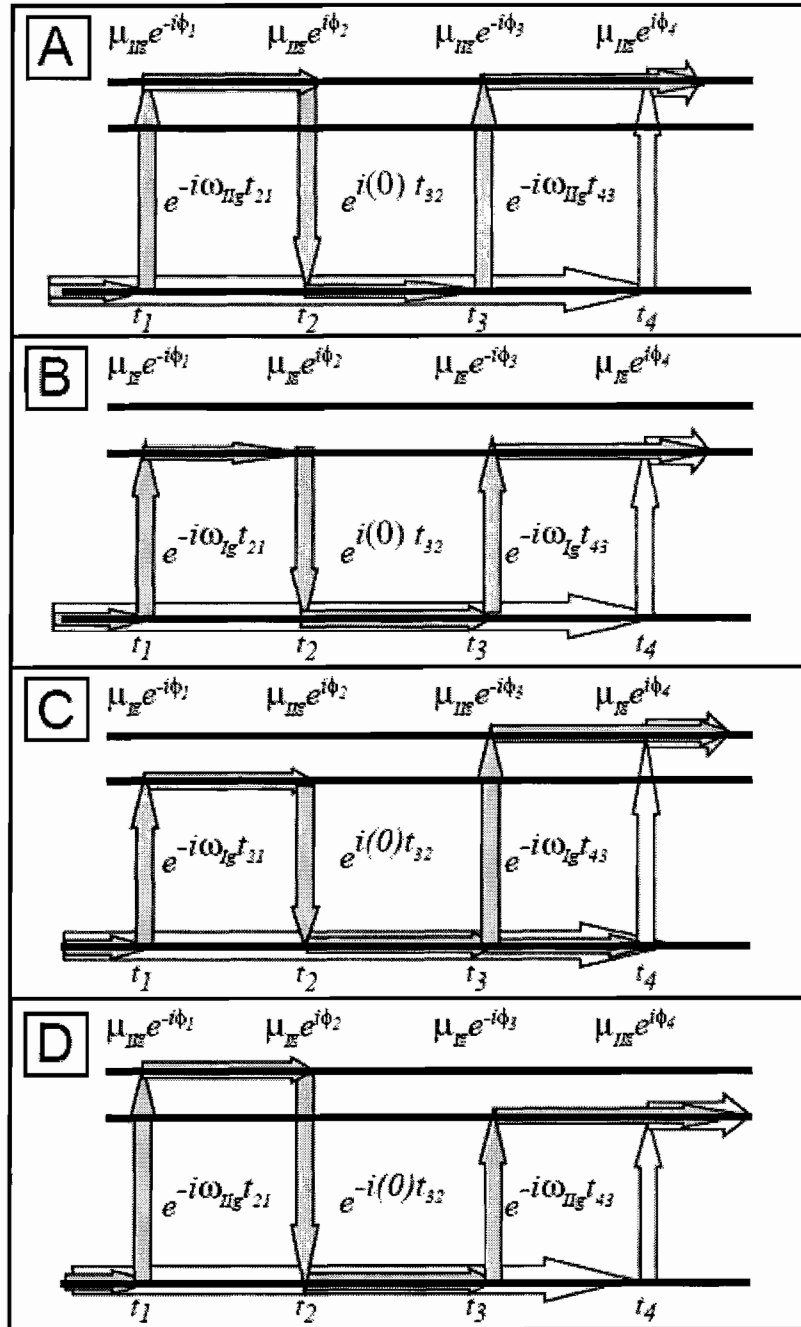
Figure 2.7: Diagrams illustrating the four distinct wave packet pathways that contribute to the $\langle \psi_4 | \psi_{321} \rangle$ overlap in a three-level system. The pathways depicted in panels (A) and (B) are 'single mode' pathways, while those depicted in panels (C) and (D) are 'coupling' pathways.

Acousto-Optic Phase Modulation in Two Dimensions

In these 2D PM-ECS experiments, we split a mode-locked pulse train into four collinear pulse trains in order to excite non-linear populations in a system. We use acousto-optic phase modulation to apply a linear sweep to the temporal phases between pulses 1 and 2 ($\phi_{21} = \phi_2 - \phi_1$), and between pulses 3 and 4 ($\phi_{43} = \phi_4 - \phi_3$). These phases are modulated at the difference frequencies of two paired sets of acousto-optics, driven at difference frequencies of $\Omega_{21}/2\pi \cong 5$ kHz and $\Omega_{43}/2\pi \cong 8$ kHz. Here, $\phi_{21} = \Omega_{21}t' + \phi_{21}^\circ$ and $\phi_{43} = \Omega_{43}t' + \phi_{43}^\circ$, where t' a quasi-continuous time variable, and ϕ_{21}° and ϕ_{43}° are constant phases. The resulting phase-modulated pulse train creates excited state populations, within which are the non-linear signal components described by Eqs. (2.23) – (2.26) modulated at the sum ($\Omega_{43} + \Omega_{21}$) or the difference ($\Omega_{43} - \Omega_{21}$) frequencies. These signals, as described in further detail below and in chapter III, are demodulated in lock-in amplifiers at the sum and difference frequencies to isolate the quadriliear overlap terms defined previously.

From Fig 2.1, we see that the individual pulses in a set are labeled with the indices $j \in \{1,2,3,4\}$, while successive sets of four pulses are indexed with $m \in \{1,2,...\}$ and separated by the repetition rate period T (not the population time T). It can be shown that the resulting sequences of pulses in the frequency domain,

$$E_{m,j}(t) = A_j(t - t_j - mT)\cos\left[\gamma_{m,j}(t - t_j - mT)\right], \qquad (2.27)$$

can be substituted into Eqs. (2.19) and (2.20), and using the fact that we detect the steady-state fluorescence accumulated over many repetitions, we obtain the interference signals as described by Eqs. (2.23) – (2.26),

$$S_{sum}\left(t_{43},t_{32},t_{21};t'\right)=2\operatorname{Re}\left\{\left\langle\psi_4|\psi_{321}\right\rangle+\left\langle\psi_{432}|\psi_1\right\rangle\right\}\propto\cos\left(\phi_{43}+\phi_{21}\right) \qquad (2.28)$$

and

$$S_{dif}\left(t_{43},t_{32},t_{21};t'\right)=2\operatorname{Re}\left\{\left\langle\psi_{421}|\psi_3\right\rangle+\left\langle\psi_{431}|\psi_2\right\rangle\right\}\propto\cos\left(\phi_{43}-\phi_{21}\right) \qquad (2.29)$$

with $\phi_{43}+\phi_{21}=\left(\Omega_{43}+\Omega_{21}\right)t'$ and $\phi_{43}-\phi_{21}=\left(\Omega_{43}-\Omega_{21}\right)t'$. Here, $t'=mT$ is a discrete, quasi-continuous, time variable with $m=0$, 1, 2, ... Thus, for fixed values of the interpulse delays, the phase of the sum and difference signals are swept in time at the frequencies $\Omega_{43}+\Omega_{21}$ and $\Omega_{43}-\Omega_{21}$, respectively. This leads to, for the values of $\Omega_{21}/2\pi$ and $\Omega_{43}/2\pi$ defined above, the combination frequencies of $\left(\Omega_{43}-\Omega_{21}\right)/2\pi\sim 3$ kHz and $\left(\Omega_{43}+\Omega_{21}\right)/2\pi\sim 13$ kHz. The frequencies of 5 kHz and 8kHz are chosen so that modulations between pulse pairs other than 1 and 2, or 3 and 4, occur at frequencies outside of the acceptance bandwidth of the lock-in amplifiers. This insures that no signal contributions are detected from overlaps other than those defined in Eqs. (2.23) – (2.26).

Phase-Sensitive Signal Detection with Acousto-Optic Phase Modulation

With these linearly modulated phase relationships we utilize monochromators and lock-in amplifiers to isolate fluorescence signal contributions generated solely from combinations of quadrilinear overlap terms, $\langle \psi_{432} | \psi_1 \rangle + \langle \psi_4 | \psi_{321} \rangle$ and $\langle \psi_{431} | \psi_2 \rangle + \langle \psi_{421} | \psi_3 \rangle$. We use lock-in amplifiers to demodulate the ac sum and difference signals into the Cartesian components, $X_{sum(dif)}(t_{43}, t_{32}, t_{21})$ and $Y_{sum(dif)}(t_{43}, t_{32}, t_{21})$, of the complex signals $Z_{sum(dif)}(t_{43}, t_{32}, t_{21})$ defined by the phase-sensitive detection method.[25]

Reference waveforms, to be used for demodulation of the fluorescence signal in the lock-in amplifiers, are generated from monochromators – one for pulses 1 and 2, and one for pulses 3 and 4. The monochromators act as narrow spectral filters of the power spectrum of the pulse pairs. For pulses 1 and 2 the power spectrum is given by $\left| \hat{E}_1^{(+)}(\omega;t') + \hat{E}_2^{(+)}(\omega;t') \right|^2$, and for pulses 3 and 4 it is given by $\left| \hat{E}_3^{(+)}(\omega;t') + \hat{E}_4^{(+)}(\omega;t') \right|^2$. The intensities transmitted by the monochromator slit are these power spectral densities evaluated at the monochromator's set frequency, $\bar{\omega}_{21}$ for pulses 1 and 2, and $\bar{\omega}_{43}$ for pulses 3 and 4. The reference signals are defined by the interference contributions to the pulse-pair power spectra at the monochromator settings,

$$R(t_{21}, t') = 2 \operatorname{Re} \hat{E}_1^{(+)*} \hat{E}_2^{(+)} (\bar{\omega}_{21}; t_{21}, t') \propto \cos \left[\bar{\omega}_{21} t_{21} - \phi_{21}(t') \right] \tag{2.30}$$

and

$$R(t_{43}, t') = 2 \operatorname{Re} \hat{E}_3^{(+)*} \hat{E}_4^{(+)} (\bar{\omega}_{43}; t_{43}, t') \propto \cos \left[\bar{\omega}_{43} t_{43} - \phi_{43}(t') \right]. \tag{2.31}$$

According to Eqs. (2.30) and (2.31), the phase of each reference varies with interpulse delay at the corresponding monochromator frequency.[26-27] For fixed delay, the reference phase varies in real time at the corresponding AO difference frequency. The sum and difference reference waveforms generated by mixing these harmonic waveforms are given by

$$R_{sum(dif)}\left(t_{43},t_{21};t'\right)=\cos\left[\overline{\omega}_{43}t_{43}\pm\overline{\omega}_{21}t_{21}-\left(\Omega_{43}\pm\Omega_{21}\right)t'-\theta_R^{sum(dif)}+\theta_{LI}^{sum(dif)}\right],\qquad(2.32)$$

where the $\pm$ sign assumes the positive or the negative value for R_{sum} or R_{dif}, respectively. In Eq. (2.32), $\theta_R^{sum(dif)}$ are constant reference phases, while $\theta_{LI}^{sum(dif)}$ are additional arbitrary phases applied by the lock-in amplifiers.

Experimentally, the fluorescence signal is simultaneously sent to two lock-in amplifiers so that both sum and difference signals are collected concurrently. The function of each lock-in amplifier is to multiply its ac signal input (from by Eqs. (2.28) and (2.29)) by the appropriate reference waveform (Eq. (2.32)), followed by application of a low-pass filter to remove remaining ac components. The demodulated in-phase ($\theta_R^{sum(dif)}=0°$) and in-quadrature ($\theta_R^{sum(dif)}=90°$) signal components are given by the integrals:

$$X_{sum(dif)}\left(t_{43}, t_{32}, t_{21}\right)$$

$$= \frac{1}{\tau_{LI}} \int_0^\infty dt' S_{sum(dif)}\left(t_{43}, t_{32}, t_{21}; t'\right) \cos\left[\bar{\omega}_{43} t_{43} \pm \bar{\omega}_{21} t_{21} - \left(\Omega_{43} \pm \Omega_{21}\right) t'\right] e^{-t'/\tau_{LI}} , \tag{2.33}$$

and

$$Y_{sum(dif)}\left(t_{43}, t_{32}, t_{21}\right)$$

$$= \frac{1}{\tau_{LI}} \int_0^\infty dt' S_{sum(dif)}\left(t_{43}, t_{32}, t_{21}; t'\right) \sin\left[\bar{\omega}_{43} t_{43} \pm \bar{\omega}_{21} t_{21} - \left(\Omega_{43} \pm \Omega_{21}\right) t'\right] e^{-t'/\tau_{LI}} , \tag{2.34}$$

where τ_{LI} (= 200 ms) is the integration time constant associated with the low-pass filter of the lock-in. In Eqs. (2.33) and (2.34), we have assumed the value for the lock-in phase $\theta_{LI}^{sum(dif)} = 0^\circ$. If $\theta_{LI}^{sum(dif)}$ was to deviate from zero, it would have the effect of shifting the $X_{sum(dif)}$ and $Y_{sum(dif)}$ interferograms by this value. Using the demodulated signals described by Eqs. (2.33) and (2.34), we construct the complex-valued functions

$$\begin{aligned}
Z_{dif}\left(t_{43}, t_{32}, t_{21}\right) &= X_{dif}\left(t_{43}, t_{32}, t_{21}\right) + i Y_{dif}\left(t_{43}, t_{32}, t_{21}\right) \\
&= e^{i\left(\bar{\omega}_{43} t_{43} - \bar{\omega}_{21} t_{21}\right)} \left[\langle \psi_{431} | \psi_2 \rangle + \langle \psi_{421} | \psi_3 \rangle\right] \\
&\equiv Z_2\left(t_{43}, t_{32}, t_{21}\right) + Z_3\left(t_{43}, t_{32}, t_{21}\right),
\end{aligned} \tag{2.35}$$

and

$$\begin{aligned}
Z_{sum}\left(t_{43}, t_{32}, t_{21}\right) &= X_{sum}\left(t_{43}, t_{32}, t_{21}\right) + i Y_{sum}\left(t_{43}, t_{32}, t_{21}\right) \\
&= e^{i\left(\bar{\omega}_{43} t_{43} + \bar{\omega}_{21} t_{21}\right)} \left[\langle \psi_4 | \psi_{321} \rangle + \langle \psi_{432} | \psi_1 \rangle\right] \\
&\equiv Z_4\left(t_{43}, t_{32}, t_{21}\right) + Z_1\left(t_{43}, t_{32}, t_{21}\right),
\end{aligned} \tag{2.36}$$

where we have defined the terms $Z_j(t_{43}, t_{32}, t_{21})$ with $j \in \{1,2,3,4\}$. In Eqs. (2.35) and (2.36), the overlap terms $\langle \psi_{432} | \psi_1 \rangle$, $\langle \psi_{431} | \psi_2 \rangle$, $\langle \psi_{421} | \psi_3 \rangle$, and $\langle \psi_4 | \psi_{321} \rangle$ are defined by Eqs. (2.23) – (2.26), with the phases imparted by the laser pulses changed to $\phi_{43} = \bar{\omega}_{43} t_{43}$ and $\phi_{21} = \bar{\omega}_{21} t_{21}$. The effect of the phase modulation/detection procedure is to replace the relative phases between laser pulse pairs with those of the reference phases determined by the monochromator settings. The detected overlaps are multiplied by the functions $e^{i(\bar{\omega}_{43} t_{43} \pm \bar{\omega}_{21} t_{21})}$, which are determined by the monochromator sum and difference phase factors. The demodulated signals are thus sums of sine and cosine functions, which vary with respect to the time intervals t_{21}, t_{32}, and t_{43} at frequencies *down-shifted* by the monochromator reference frequencies (for example, see Eqs. (3.1) – (3.4) in the following chapter). This relatively slowly varying signal is similar to the systematically under-sampled signals obtained using phase-locked pulses.[19,28-31] The process of downshifting the overlap frequencies by the monochromator reference frequencies introduces a number of highly beneficial advantages: systematic undersampling of the data allows for a fully characterized data set to be collected with fewer data points, the signal-to-noise ratio is significantly enhanced by passive stabilization and reduction of mechanical instability effects, simultaneous collection of both rephasing and nonrephasing data sets, and filtering of *1/f* noise by the lock-in amplifiers.

Determination of the Third-Order Susceptibilities

The primary observables of time-domain nonlinear optical spectroscopy are the nonlinear response functions of the system. Here, we will demonstrate the process for transforming the collected time-domain data of the nonlinear response functions[12] into the corresponding frequency-dependent third-order susceptibilities. The complex population terms, Z_{dif} and Z_{sum} (Eqs. 2.35 and 2.36), are related to the nonlinear susceptibilities via linear response theory, which describes the polarization induced in the sample by resonant interactions with the four excitation fields.

The polarization can be generally expressed as the mean expectation of the transition dipole moment operator

$$P(t) = \left\langle \Psi^I(t) \left| \underset{\sim}{\mu}^I(t) \right| \Psi^I(t) \right\rangle. \tag{2.37}$$

The polarization is the radiation emitted by the system due to its resonance with the electric fields. It can be expressed as the convolution of the optical response function with the applied field. Upon substitution of Eq. (2.13) into Eq. (2.41), we obtain

$$P^{(3)}(t) = \int_0^\infty d\tau \int_0^\infty d\tau' \int_0^\infty d\tau'' \chi^{(3)}(\tau'',\tau',\tau) E(t-\tau) E(t-\tau-\tau') E(t-\tau-\tau'-\tau''). \tag{2.38}$$

Equation (2.38) describes the polarization to third-order as the triple convolution of the response function $\chi^{(3)}(\tau'',\tau',\tau)$ in terms of three field-matter interactions, separated by

three distinct time intervals. The real-valued response function can be written as the sum of two complex-valued functions:

$$\chi^{(3)}\left(\tau'',\tau',\tau\right)=\sum_{j=1}^{4}(-i)\left\{\Re_j\left(\tau'',\tau',\tau\right)-\Re_j^*\left(\tau'',\tau',\tau\right)\right\},\tag{2.39}$$

where the $\Re_j$'s are expectations of the time-ordered transition dipole correlation functions:

$$\Re_1\left(\tau'',\tau',\tau\right)=\left\langle g\left|\underset{\sim}{\mu}^I\left(t-\tau-\tau'\right)\underset{\sim}{\mu}^I\left(t-\tau\right)\underset{\sim}{\mu}^I\left(t\right)\underset{\sim}{\mu}^I\left(t-\tau-\tau'-\tau''\right)\right|g\right\rangle,\tag{2.40}$$

$$\Re_2\left(\tau'',\tau',\tau\right)=\left\langle g\left|\underset{\sim}{\mu}^I\left(t-\tau-\tau'-\tau''\right)\underset{\sim}{\mu}^I\left(t-\tau\right)\underset{\sim}{\mu}^I\left(t\right)\underset{\sim}{\mu}^I\left(t-\tau-\tau'\right)\right|g\right\rangle,\tag{2.41}$$

$$\Re_3\left(\tau'',\tau',\tau\right)=\left\langle g\left|\underset{\sim}{\mu}^I\left(t-\tau-\tau'-\tau''\right)\underset{\sim}{\mu}^I\left(t-\tau-\tau'\right)\underset{\sim}{\mu}^I\left(t\right)\underset{\sim}{\mu}^I\left(t-\tau\right)\right|g\right\rangle,\tag{2.46}$$

and

$$\Re_4\left(\tau'',\tau',\tau\right)=\left\langle g\left|\underset{\sim}{\mu}^I\left(t\right)\underset{\sim}{\mu}^I\left(t-\tau\right)\underset{\sim}{\mu}^I\left(t-\tau-\tau'\right)\underset{\sim}{\mu}^I\left(t-\tau-\tau'-\tau''\right)\right|g\right\rangle.\tag{2.47}$$

In Eqs. (2.40) – (2.43), transition dipole interactions occur at the times $t-\tau-\tau'-\tau''$, $t-\tau-\tau'$, $t-\tau$, and t. In the context of this theory the emitted polarization defined in Eq. (2.42) is detected at time t with the fourth pulse acting as a heterodyne field. We neglect the effects of pulse overlap and assign the time intervals τ, τ', and τ'',

respectively, to our experimental inter-pulse delays t_{43}, t_{32}, and t_{21}. We calculate explicit forms for the third-order response functions (Eqs. (2.44) – (2.47)) using the system Hamiltonian (Eq. (2.6)) and the dipole operator (Eq. (2.9))

$$\Re_1\left(t_{21},t_{32},t_{43}\right)=\sum_{a,b}\mu_{ag}^2\mu_{bg}^2 e^{-i\omega_{ag}\left(t_{43}+t_{21}\right)}e^{-i\left(\omega_{ag}-\omega_{bg}\right)t_{32}}\ , \tag{2.44}$$

$$\Re_2\left(t_{21},t_{32},t_{43}\right)=\sum_{a,b}\mu_{ag}^2\mu_{bg}^2 e^{-i\omega_{ag}t_{43}}e^{i\omega_{bg}t_{21}}e^{-i\left(\omega_{ag}-\omega_{bg}\right)t_{32}}\ , \tag{2.45}$$

$$\Re_3\left(t_{21},t_{32},t_{43}\right)=\sum_{a,b}\mu_{ag}^2\mu_{bg}^2 e^{-i\omega_{ag}t_{43}}e^{i\omega_{bg}t_{21}}\ , \tag{2.46}$$

and

$$\Re_4\left(t_{21},t_{32},t_{43}\right)=\sum_{a,b}\mu_{ag}^2\mu_{bg}^2 e^{-i\omega_{ag}t_{43}}e^{-i\omega_{bg}t_{21}}\ . \tag{2.47}$$

In Eqs. (2.44) – (2.47), we have used the indices $a,b \in \{1,2,...,n\}$, and omitted the possibility of non-resonant transitions between excited states. We see from comparison between Eqs. (2.44) – (2.47) and our expressions for the non-linear populations in Eqs. (2.23) – (2.26) that each of the four response functions can be assigned to an individual overlap term: $\Re_1 \leftrightarrow \langle \psi_{432}|\psi_1 \rangle$, $\Re_2 \leftrightarrow \langle \psi_{431}|\psi_2 \rangle$, $\Re_3 \leftrightarrow \langle \psi_{421}|\psi_3 \rangle$, and $\Re_4 \leftrightarrow \langle \psi_4|\psi_{321} \rangle$. It follows that our detected signals, Z_{dif} and Z_{sum} (Eqs. (2.35) and (2.36)) correspond to the rephasing and non-rephasing contributions to the resonant response functions (i.e,

$2\operatorname{Im}(\Re_2 + \Re_3)$ and $2\operatorname{Im}(\Re_1 + \Re_4)$, respectively), weighted by the pulse spectral densities at the transition frequencies, and modulated by the phase factors $e^{i(\bar{\omega}_{43}t_{43} - \bar{\omega}_{21}t_{21})}$ and $e^{i(\bar{\omega}_{43}t_{43} + \bar{\omega}_{21}t_{21})}$, respectively.

We define the complex third-order susceptibility $\hat{\chi}^{(3)}(\omega_{21}, t_{32}, \omega_{43})$ as the partial Fourier transform of the response function with respect to the variable time-delays t_{21} and t_{43}.

$$\hat{\chi}^{(3)}(\omega_{21}, t_{32}, \omega_{43}) = \int_0^\infty dt_{43} \int_0^\infty dt_{21} \chi^{(3)}(t_{21}, t_{32}, t_{43}) e^{i\omega_{21}t_{21}} e^{i\omega_{43}t_{43}} \,. \tag{2.48}$$

Since the response function, Eq. (2.39), is real-valued, symmetry considerations imply[12] that the susceptibility is a sum of positive and negative frequency components, i.e.,

$$\hat{\chi}^{(3)}(\omega_{21}, t_{32}, \omega_{43}) = \hat{\chi}_+^{(3)}(\omega_{21}, t_{32}, \omega_{43}) + \hat{\chi}_-^{(3)}(\omega_{21}, t_{32}, \omega_{43}), \quad \text{with} \quad \hat{\chi}_-^{(3)}(\omega_{21}, t_{32}, \omega_{43})$$

$$= \left[\hat{\chi}_+^{(3)}(-\omega_{21}, t_{32}, -\omega_{43}) \right]^* \text{ and}$$

$$\hat{\chi}_+^{(3)}(\omega_{21}, t_{32}, \omega_{43}) = \sum_{j=1}^4 (-i) \int_{-\infty}^\infty dt_{43} \int_{-\infty}^\infty dt_{21} \Re_j(t_{21}, t_{32}, t_{43}) e^{i\omega_{21}t_{21}} e^{i\omega_{43}t_{43}} \tag{2.49}$$

$$= \sum_{j=1}^4 (-i) \hat{\Re}_j(\omega_{21}, t_{32}, \omega_{43}).$$

We can further separate $\hat{\chi}_{+}^{(3)}\left(\omega_{21},t_{32},\omega_{43}\right)$ into rephasing and non-rephasing contributions:

$$\hat{\chi}_{+RP}^{(3)}\left(\omega_{21},t_{32},\omega_{43}\right)=-i\left[\hat{\Re}_{2}\left(\omega_{21},t_{32},\omega_{43}\right)+\hat{\Re}_{3}\left(\omega_{21},t_{32},\omega_{43}\right)\right] \tag{2.50}$$

and

$$\hat{\chi}_{+NRP}^{(3)}\left(\omega_{21},t_{32},\omega_{43}\right)=-i\left[\hat{\Re}_{1}\left(\omega_{21},t_{32},\omega_{43}\right)+\hat{\Re}_{4}\left(\omega_{21},t_{32},\omega_{43}\right)\right]. \tag{2.51}$$

To connect the rephasing and non-rephasing susceptibilities in Eqs. (2.50) and (2.51) to our PM-ECS measurements, we Fourier transform the complex signals Z_{dif} and Z_{sum} given by Eqs. (2.35) and (2.36). The resulting expressions are related to the functions $\hat{\Re}_{j}\left(\omega_{21},t_{32},\omega_{43}\right)$, after compensating for the frequency down-shifting imposed by the monochromator settings:

$$\frac{\hat{Z}_{dif}\left(\omega_{21}+\overline{\omega}_{21},t_{32},\omega_{43}-\overline{\omega}_{43}\right)}{\alpha^{2}\left(\omega_{21}\right)\alpha^{2}\left(\omega_{43}\right)}\cong\hat{\Re}_{2}\left(\omega_{21},t_{32},\omega_{43}\right)+\hat{\Re}_{3}\left(\omega_{21},t_{32},\omega_{43}\right) \tag{2.52}$$

$$=i\hat{\chi}_{+RP}^{(3)}\left(\omega_{21},t_{32},\omega_{43}\right)$$

and

$$\frac{\hat{Z}_{sum}\left(\omega_{21}-\overline{\omega}_{21},t_{32},\omega_{43}-\overline{\omega}_{43}\right)}{\alpha^{2}\left(\omega_{21}\right)\alpha^{2}\left(\omega_{43}\right)}\cong\hat{\Re}_{1}\left(\omega_{21},t_{32},\omega_{43}\right)+\hat{\Re}_{4}\left(\omega_{21},t_{32},\omega_{43}\right) \tag{2.53}$$

$$=i\hat{\chi}_{+NRP}^{(3)}\left(\omega_{21},t_{32},\omega_{43}\right).$$

Equations (2.53) and (2.54) describe the resonant rephasing and non-rephasing third-order susceptibilities, in terms of our sum and difference population contributions. In contrast to linear susceptibility,[32] absorptive and dispersive contributions to the third-order susceptibility are not clearly partitioned by the real and imaginary signal components, but it has been demonstrated that a simple transformation of the rephasing and nonrephasing spectra, $\hat{\chi}_C^{(3)}\left(\omega_{21},t_{32},\omega_{43}\right) = \hat{\chi}_{NRP}^{(3)}\left(\omega_{21},t_{32},\omega_{43}\right) + \hat{\chi}_{RP}^{(3)}\left(\omega_{21},t_{32},-\omega_{43}\right)$, allows for approximate separation into absorptive and dispersive contributions.[23,24] The real (imaginary) part of $\hat{\chi}_C^{(3)}$ corresponds to the change in absorption (dispersion) at the detection frequency ω_{43}, which is induced by excitation at the frequency ω_{21}.

Summary

In this chapter we have presented the theory behind two-dimensional phase-modulation electronic coherence spectroscopy. Through third-order perturbation theory and acousto-optic phase modulation, we have demonstrated the ability to isolate the time-domain quadrilinear overlap contributions to the total fluorescence signal (by demodulation in lock-in amplifiers) resulting from a collinear four-pulse sequence and Fourier transform them into the corresponding complex third-order susceptibility. The experimental viability of the 2D PM-ECS technique will be demonstrated in the following chapter on a simple three level atomic system.

CHAPTER III

TWO-DIMENSIONAL ELECTRONIC COHERENCE SPECTROSCOPY

EXPERIMENTS PERFORMED ON ATOMIC RUBIDIUM

Having developed the theoretical formalism for 2D PM-ECS experiments in Chapter II, we now demonstrate its efficacy by performing a series of experiments on atomic rubidium vapor. This chapter contains material co-authored with P.F. Tekavec and A.H. Marcus.

Atomic Rubidium as a Model System

We demonstrate 2D PM-ECS by performing proof-of-principle experiments on a well-defined, simple model system – atomic rubidium. Rubidium (Rb) has an absorption spectrum with two narrow optical transitions (D_1 with $\lambda_1 = 794.7$ nm and D_2 with $\lambda_2 = 780.0$ nm, see Fig. 3.1) spanned by the Ti:Sa laser bandwidth. In Table 3.1 we list the spectroscopic parameters of the Rb D line transitions.[1] Each of the three electronic states ($5^2S_{1/2}$, $5^2P_{1/2}$, and $5^2P_{3/2}$) are associated with degenerate magnetic sub-levels and hyperfine sub-levels introduced by nuclear spin – electron spin orbit coupling. Nevertheless, in our experiments these degeneracies and splittings are not resolved. We therefore regard the atom as an effective three-level system. We label $5^2S_{1/2}$ as the

Table 3.1: Physical constants associated with ^{87}Rb optical D line transitions. n is the transition index, ω_{ng} is the transition frequency, λ_{ng} is the transition wavelength, μ_{ng} is the transition dipole moment (in units of Debye), τ is the lifetime, and Γ is the natural line width (Johansson 1961).

N	label	ω_{ng} (rad fs^{-1})	λ_{ng} (nm)	μ_{ng} (ea$_0$)	τ (ns)	Γ ($2\pi \cdot$ MHz)
1	D$_1$	2.370	794.7	2.992	27.70	5.747
2	D$_2$	2.414	780.0	4.227	26.24	6.066
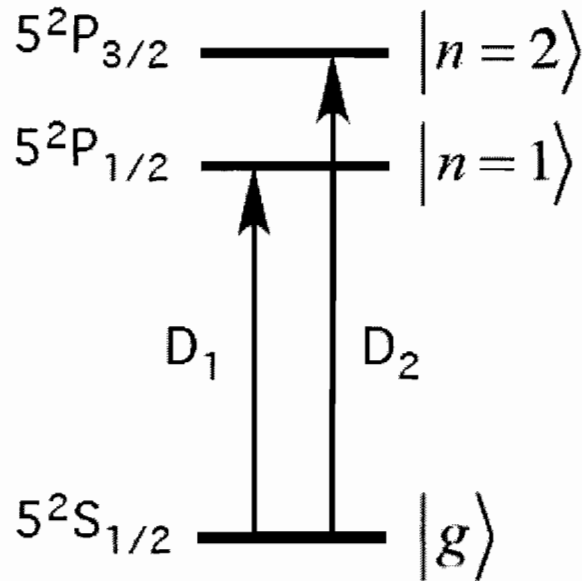
Figure 3.1: Energy level diagram for the rubidium D line transitions accessible by Ti:Sapphire laser spectrum. The system can be treated as a three level system for these experiments, with a single ground state and two excited states that are non-resonantly coupled.

ground state $|g\rangle$, $5^2 P_{1/2}$ as the first excited state $|n=1\rangle$, and $5^2 P_{3/2}$ as the second excited state $|n=2\rangle$. Because of the relative simplicity of the system Hamiltonian, our data can be easily compared to theoretical predictions.

<u>Experimental Apparatus and Procedure</u>

In Fig. 3.2, we show a schematic diagram of the experimental apparatus used for the Rb experiments. A full account of the experimental apparatus can be found in Ref. [2], and the similar, current apparatus will be described in full in chapter VI. Briefly, we use the 800kHz output of a cavity dumped Ti:Sapphire oscillator to generate a sequence of four laser pulses in the separate arms of two identical Mach-Zender interferometers. Each of these beams is focused through a TeO_2 acousto-optic, imparting the specific phase relationships described in chapter II. Three computer controlled delay stages control the relative arrival times at the sample for each of the four pulses in the sequence. The beams, once recombined collinearly, are focused into a Rb vapor cell, and a portion of the resulting fluorescence is collected by an amplified photo-diode. Additionally, a part of the pulse pair from each interferometer is sent into a used to generate a reference signal in a monochromator, as described in chapter II.

The fluorescence and reference signals are multiplied together in two lock-in amplifiers, isolating the fluorescence contributions oscillating at the sum and difference reference frequencies. The demodulated sum and difference signals are collected via computer.

Two-dimensional arrays of time-domain data are collected by varying the time

delays between pulses 1 & 2, the coherence time t_{21}, and the time delay between pulses 3

& 4, the detection time t_{43}. The time delay between the two pulse pairs, the population

time t_{32}, is held fixed for any particular experiment. In-phase and in-quadrature data is
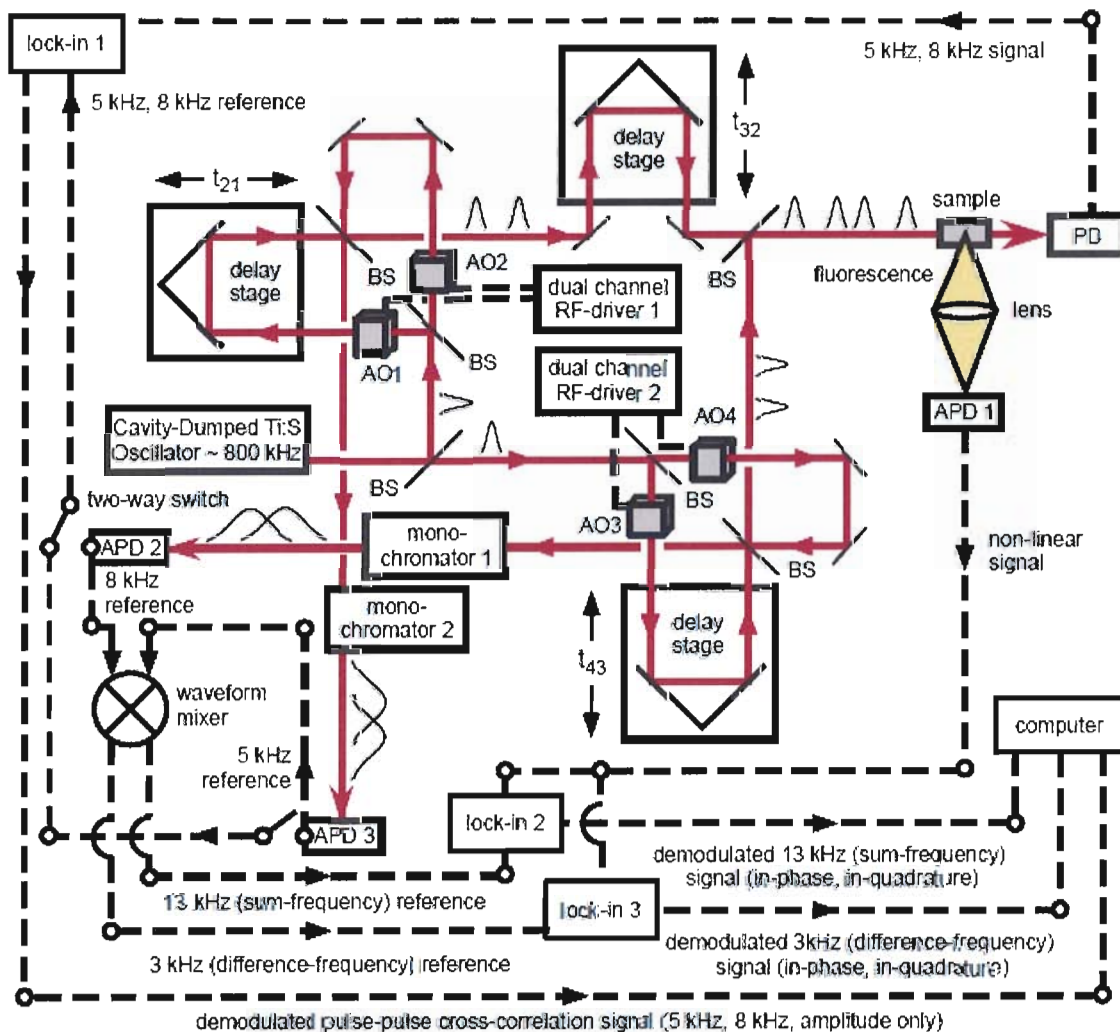
Figure 3.2: Schematic diagram of the experimental setup for phase modulation (PM-) ECS (described in text). Abbreviations have the following meanings. APD: amplified photodiode; PD: pin photodiode; AO: acousto-optic Bragg cell; BS: beam splitter.

collected for both sum and difference signals, allowing for construction of the complex

valued functions $Z_{sum(dif)} = X_{sum(dif)} + iY_{sum(dif)}$.

To collect these signals in a properly phased manner,[3] the arbitrary relative phases

of the lock-in amplifiers, $\theta_{LI}^{sum(dif)}$, are set such that the in-quadrature

signals $Y_{sum(dif)}(0,t_{32},0) = 0$ at the time origin $t_{43} = t_{21} = 0$ and the in-phase signals are

positively maximized, resulting in the fluorescence signals $X_{sum(dif)}(t_{43},t_{32},t_{21})$ and

$Y_{sum(dif)}(t_{43},t_{32},t_{21})$ given in Eqs. (2.33) and (2.34), respectively.

Time-Domain Interferograms

By demodulating the fluorescence signal and collecting the terms that are

modulated at the sum and difference frequencies, we isolate all signal contributions from

interferences between a one-pulse and three-pulse wave packet that are linear in each of

the four excitation fields, given by the downshifted complex valued response functions

$$Z_{dif} = Z_2 + Z_3 = e^{i(\bar{\omega}_{43}t_{43} - \bar{\omega}_{21}t_{21})} \times \left[\langle \psi_{431}|\psi_2 \rangle + \langle \psi_{421}|\psi_3 \rangle \right] \text{ and}$$

$$Z_{sum} = Z_1 + Z_4 = e^{i(\bar{\omega}_{43}t_{43} + \bar{\omega}_{21}t_{21})} \left[\langle \psi_{432}|\psi_1 \rangle + \langle \psi_4|\psi_{321} \rangle \right] \text{ for difference and sum signals,}$$

respectively (Eqs. (2.35) and (2.36)). The rapidly oscillating wave packet overlaps of the

system, as a function of interpulse delay, are downshifted by the respective reference

frequencies in the demodulation process, creating relatively slowly oscillating data

waveforms. Rewriting Eqs. (2.23) – (2.26) for a three level system with indirectly

coupled excited states and multiplying by the reference signals, the downshifted complex valued response functions are expected to have the forms

$$Z_2 = \mu_{1g}^4 \alpha^4 \left(\omega_{1g} \right) e^{-i\left(\omega_{1g} - \bar{\omega}_{43} \right) t_{43} + i\left(\omega_{1g} - \bar{\omega}_{21} \right) t_{21}} + \mu_{2g}^4 \alpha^4 \left(\omega_{2g} \right) e^{-i\left(\omega_{2g} - \bar{\omega}_{43} \right) t_{43} + i\left(\omega_{2g} - \bar{\omega}_{21} \right) t_{21}}$$

$$+\mu_{1g}^2 \mu_{2g}^2 \alpha^2 \left(\omega_{1g} \right) \alpha^2 \left(\omega_{2g} \right) e^{-i\left(\omega_{1g} - \bar{\omega}_{43} \right) t_{43} + i\left(\omega_{2g} - \bar{\omega}_{21} \right) t_{21} - i\left(\omega_{1g} - \omega_{2g} \right) t_{32}}$$

$$+\mu_{1g}^2 \mu_{2g}^2 \alpha^2 \left(\omega_{1g} \right) \alpha^2 \left(\omega_{2g} \right) e^{-i\left(\omega_{2g} - \bar{\omega}_{43} \right) t_{43} + i\left(\omega_{1g} - \bar{\omega}_{21} \right) t_{21} - i\left(\omega_{2g} - \omega_{1g} \right) t_{32}} \qquad (3.1)$$

and

$$Z_3 = \mu_{1g}^4 \alpha^4 \left(\omega_{1g} \right) e^{-i\left(\omega_{1g} - \bar{\omega}_{43} \right) t_{43} + i\left(\omega_{1g} - \bar{\omega}_{21} \right) t_{21}} + \mu_{2g}^4 \alpha^4 \left(\omega_{2g} \right) e^{-i\left(\omega_{2g} - \bar{\omega}_{43} \right) t_{43} + i\left(\omega_{2g} - \bar{\omega}_{21} \right) t_{21}}$$

$$+\mu_{1g}^2 \mu_{2g}^2 \alpha^2 \left(\omega_{1g} \right) \alpha^2 \left(\omega_{2g} \right) e^{-i\left(\omega_{2g} - \bar{\omega}_{43} \right) t_{43} + i\left(\omega_{1g} - \bar{\omega}_{21} \right) t_{21}}$$

$$+\mu_{1g}^2 \mu_{2g}^2 \alpha^2 \left(\omega_{1g} \right) \alpha^2 \left(\omega_{2g} \right) e^{-i\left(\omega_{1g} - \bar{\omega}_{43} \right) t_{43} + i\left(\omega_{2g} - \bar{\omega}_{21} \right) t_{21}} \qquad (3.2)$$

for the difference signal, and

$$Z_1 = \mu_{1g}^4 \alpha^4 \left(\omega_{1g} \right) e^{-i\left(\omega_{1g} - \bar{\omega}_{43} \right) t_{43} - i\left(\omega_{1g} - \bar{\omega}_{21} \right) t_{21}} + \mu_{2g}^4 \alpha^4 \left(\omega_{2g} \right) e^{-i\left(\omega_{2g} - \bar{\omega}_{43} \right) t_{43} - i\left(\omega_{2g} - \bar{\omega}_{21} \right) t_{21}}$$

$$+\mu_{1g}^2 \mu_{2g}^2 \alpha^2 \left(\omega_{1g} \right) \alpha^2 \left(\omega_{2g} \right) e^{-i\left(\omega_{1g} - \bar{\omega}_{43} \right) t_{43} - i\left(\omega_{1g} - \bar{\omega}_{21} \right) t_{21} - i\left(\omega_{1g} - \omega_{2g} \right) t_{32}}$$

$$+\mu_{1g}^2 \mu_{2g}^2 \alpha^2 \left(\omega_{1g} \right) \alpha^2 \left(\omega_{2g} \right) e^{-i\left(\omega_{2g} - \bar{\omega}_{43} \right) t_{43} - i\left(\omega_{2g} - \bar{\omega}_{21} \right) t_{21} - i\left(\omega_{2g} - \omega_{1g} \right) t_{32}} \qquad (3.3)$$

and

$$Z_4 = \mu_{1g}^4 \alpha^4\left(\omega_{1g}\right)e^{-i\left(\omega_{1g}-\bar{\omega}_{43}\right)t_{43}-i\left(\omega_{1g}-\bar{\omega}_{21}\right)t_{21}} + \mu_{2g}^4 \alpha^4\left(\omega_{2g}\right)e^{-i\left(\omega_{2g}-\bar{\omega}_{43}\right)t_{43}-i\left(\omega_{2g}-\bar{\omega}_{21}\right)t_{21}} \qquad (3.4)$$
$$+\mu_{1g}^2\mu_{2g}^2\alpha^2\left(\omega_{1g}\right)\alpha^2\left(\omega_{2g}\right)e^{-i\left(\omega_{2g}-\bar{\omega}_{43}\right)t_{43}-i\left(\omega_{1g}-\bar{\omega}_{21}\right)t_{21}}$$
$$+\mu_{1g}^2\mu_{2g}^2\alpha^2\left(\omega_{1g}\right)\alpha^2\left(\omega_{2g}\right)e^{-i\left(\omega_{1g}-\bar{\omega}_{43}\right)t_{43}-i\left(\omega_{2g}-\bar{\omega}_{21}\right)t_{21}}$$

for the sum signal. The system and pulse parameters involved in Eqs. (3.1) – (3.4) are either well known (Rb parameters in Table 3.1) or easily measured (center wavelength of 787 nm, FWHM bandwidth of 33 nm, Gaussian pulse width of 31.5 fs, and time-bandwidth product of 0.51).

Having defined the four downshifted quadrilinear overlaps in Eqs. (3.1) – (3.4), it is beneficial to examine each of the four specific pulse-energy level pathways that contribute to each Z_i term. It is clear that each contribution to each Z_i term accumulates phase uniquely as a function of the three interpulse delays. If we consider each panel in Figs. 2.4 – 2.7, we see that the first term in each of Eqs. (3.1) – (3.4) corresponds to panel B in the corresponding figure, while the second term corresponds to the A panels. The third and fourth terms in each Z_i sum correspond to the C and D panels respectively. The first two terms in each of Eqs. (3.1) – (3.4), evolving on the ground state and only a single ($n = 1$ or $n = 2$) of the two excited states during the three interpulse delays, while the latter two terms in each of Eqs. (3.1) – (3.4) will involve evolution on each of the two excited states, yielding information about ground state mediated coupling processes. Population transfer does not contribute on the timescales of these experiments.

Let us consider the phase factor of the difference signals, $e^{i\left(\bar{\omega}_{43}t_{43}-\bar{\omega}_{21}t_{21}\right)}e^{-i\left(\omega_{ag}t_{43}-\omega_{bg}t_{21}\right)}$, where $a,b \in \{1,2\}$. For a positive phase accumulation during t_{21}, there is a corresponding

negative phase accumulation during t_{43} (and vice versa). This is a result of the Hermitian conjugate pathways traversed during these time periods by the wave packets. This is also clear from examination of the difference signal contribution pathways shown in Fig. 2.3 These conjugate pathways cause the wave packet phases to "rephase," analogous to the rephasing contributions to a 2D NMR or photon echo experiment;[4,5] therefore, these difference signal contributions are interchangeably referred to as rephasing (RP) or echo signal contributions. Similarly, we consider the phase factor of the sum signals,

$e^{i(\overline{\omega}_{43}t_{43}+\overline{\omega}_{21}t_{21})}e^{-i(\omega_{ag}t_{43}+\omega_{bg}t_{21})}$. During the time periods t_{21} and t_{43}, we see that the phase accumulation of the wave packets is additive in the situations described above. The sum signal contributions are also referred to as the non-rephasing (NRP) signal contributions.

For a three level system such as Rb, only the ground state mediated coupling pathways from the Z_1 and Z_2 overlaps have non-zero t_{32} dependence. These are the only pathways in which the bra and ket wave packets evolve on separate energy levels during t_{32}. These signal contributions are referred to as "stimulated emission" contributions because the fourth pulse acts as a probe of the evolution of the system during t_{32} and the action of the third pulse, which stimulates emission by driving amplitude from the three pulse wave packet from an excited state to the ground state. The coupling contributions to Z_3 and Z_4 are both in the ground state during t_{32}. These are referred to as "ground state bleach" pathways because the fourth pulse probes the system after the third pulse drives amplitude in the three pulse wave packet from the ground state to one of the excited states. As we will see excitonic systems or systems in which transitions can be driven

between excited electronic energy levels, there is a third kind of contribution that does not contribute to the Rb signal, referred to as "excited state absorption."

We expect the rephasing and non-rephasing signals to oscillate with a period of the inverse of the frequency difference between the two excited energy levels of rubidium, $2\pi/\left(\omega_{2g}-\omega_{1g}\right)$ = 140 fs, so for the remainder of this discussion we will display and discuss the results for t_{32} = 140 fs and the half-period difference at t_{32} = 210 fs. Figure 3.3 shows the calculated (panels A-D) and experimentally collected (panels E-H) 2D interferograms for the difference signal, $Z_{dif} = Z_2 + Z_3$. The left-hand column shows the in-phase ("real") component and the right-hand column shows the in-quadrature ("imaginary") component of the difference signal contribution to the fluorescence. The top row in both theory and data plots is for t_{32} = 140 fs, and the bottom row for t_{32} = 210 fs. Figure 3.4 shows the equivalent theory and data interferograms for the sum signal component, $Z_{sum} = Z_1 + Z_4$. We immediately note that in both cases, the experimental data is in exceptional agreement with the calculated interferograms. The change in structure between t_{32} = 140 fs and t_{32} = 210 fs interferograms can be understood as a 90° phase shift of the t_{32} dependent phase factor in relation to those independent of t_{32}.

53
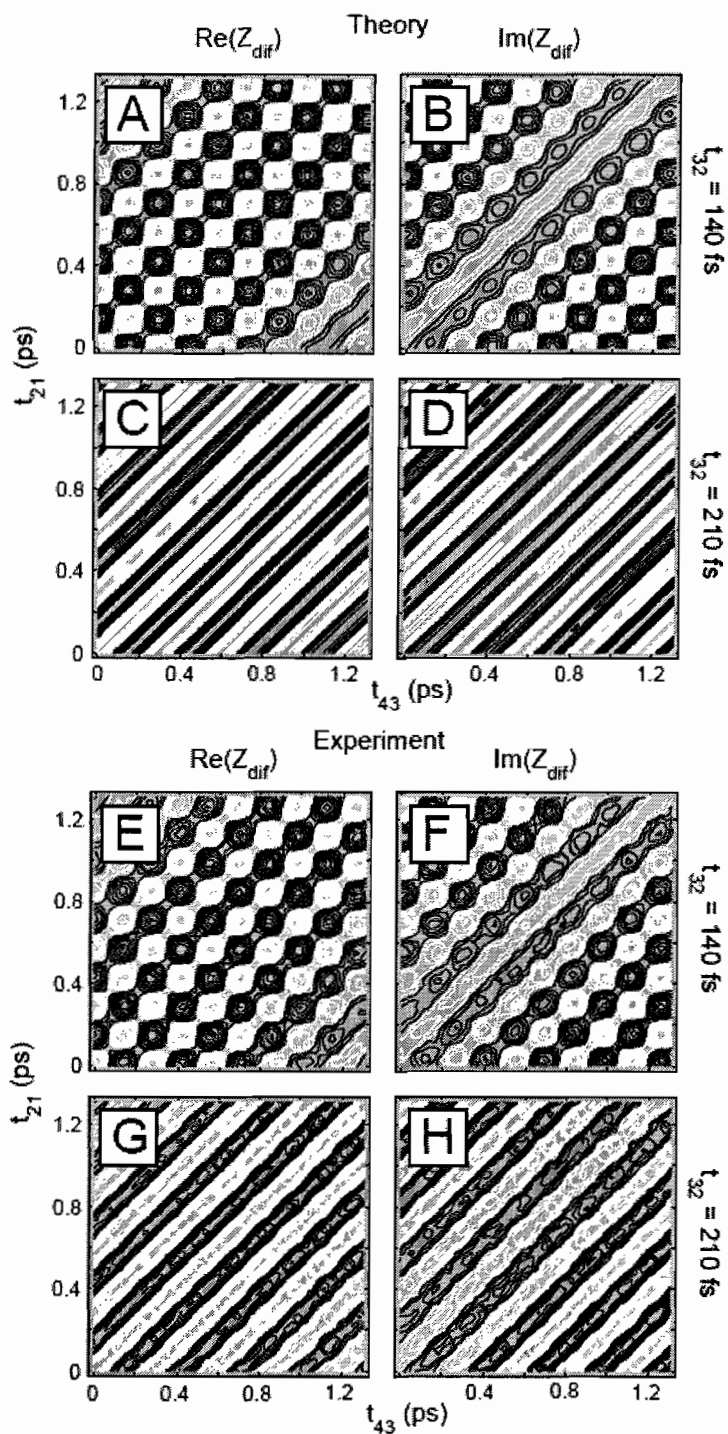
Figure 3.3: Comparison between theoretical calculations (panels (A) – (D)) and experimental data (panels (E) – (H)) for the difference-signal interferograms obtained by PM-ECS (described in text).
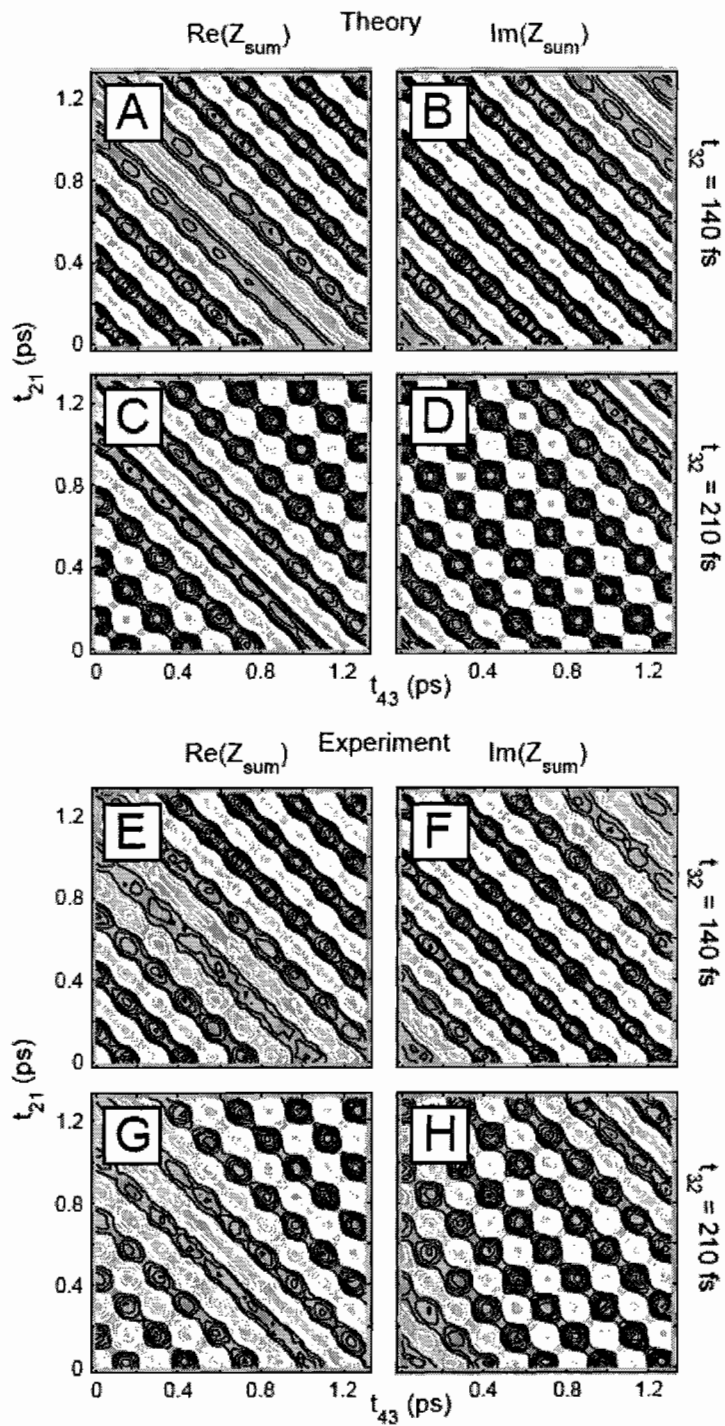
Figure 3.4: Comparison between theoretical calculations (panels (A) – (D)) and experimental data (panels (E) – (H)) for the sum-signal interferograms obtained by PM-ECS (described in text).

Third-Order Susceptibilities

Ultimately, we wish to relate the results of the collected nonlinear response functions to the nonlinear susceptibility, as discussed in chapter II, where we described how to construct the complex signals $Z_{sum(dif)}\left(t_{43},t_{32},t_{21}\right) =$

$X_{sum(dif)}\left(t_{43},t_{32},t_{21}\right) +iY_{sum(dif)}\left(t_{43},t_{32},t_{21}\right)$ from the collected in-phase and in-quadrature interferograms, Fourier transforming the results in accordance with Eqs. (2.49) – (2.51) to generate the complex rephasing and non-rephasing third-order susceptibilities,

$\hat{\chi}^{(3)}_{+RP}\left(\omega_{21},t_{32},\omega_{43}\right)$ and $\hat{\chi}^{(3)}_{+NRP}\left(\omega_{21},t_{32},\omega_{43}\right)$, described explicitly in Eqs. (2.52) and (2.53) for properly phased data. The experimental data are multiplied by a slow decaying windowing function[6] (standard deviation ~3.5 ps) to force the time-domain interferograms to decay towards zero in the longest timescales accessed by our experiments (~10 ps). This will artificially broaden the transition lineshapes, so it is important to choose windowing function timescales appropriately.

The complex-valued rephasing and non-rephasing third-order susceptibilities, as defined in Eqs. (2.52) and (2.53), are shown in Figs. 3.5 and 3.6, respectively. Again, we compare theoretical calculations (panels A-D) to the experimental results (panels E-H). The real and imaginary parts of the third-order susceptibilities are shown in the left and right columns of the figures, respectively, for population times of t_{32} = 140 fs and t_{32} = 210 fs as labeled. As in the case of the time-domain results, the expected spectra agree very well with experimental results. We note that real and imaginary data contributions agree well with theoretical calculations, confirming proper phasing of the data during

collection. 2D spectra can be understood as the change in absorption (or dispersion) of a system from resonant interactions at the frequency ω_{43}, due to preceding excitations at frequency ω_{21}, and separated by t_{32}.[7] Diagonal features, occurring at the same value on both the ω_{21} and ω_{43} axes, correspond to contributions from those pathways that only interact with a single of the two excited states (e.g. the first two terms in each Z_i sum, and panels A and B in Figs. 2.4 – 2.7), and occur at sites in agreement with the well known fundamental frequencies.

Off-diagonal features in the 2D spectra occur at coordinates that couple the fundamental transition frequencies, $(\omega_{1g}, \omega_{2g})$ and $(\omega_{2g}, \omega_{1g})$, and are defined by the latter two terms in each Z_i sum, and panels C and D of Figs. 2.4 – 2.7. In the rephasing signal $\hat{\chi}^{(3)}_{+RP}$, corresponding to the Fourier transforms of Z_2 and Z_3, the off-diagonal terms will oscillate as a function of t_{32} for the reasons described in the previous section. These coherent oscillations arise because each of the static off-diagonal ground state bleach contributions (Z_3) has a corresponding off-diagonal stimulated emission term (Z_2) that is oscillatory as a function of t_{32}. These ground state bleach and stimulated emission terms have equivalent amplitudes, and therefore are expected to oscillate between zero and the diagonal peak amplitudes with a period of $2\pi\big/\left(\omega_{2g} - \omega_{1g}\right) = 140$ fs, in agreement with the observed results of maximized off-diagonal features at $t_{32} = 140$ fs, and minimized off-diagonal features at $t_{32} = 210$ fs in $\hat{\chi}^{(3)}_{+RP}$.

Similar observations may be made about the non-rephasing signal, $\hat{\chi}^{(3)}_{+NRP}$, shown in Fig. 3.6 and comprised of Fourier transforms of Z_1 (stimulated emission contributions)

and Z_4 (ground state bleach contributions). We note from equation 3.3 that all terms in Z_1 have identical frequencies during the coherence and detection periods, meaning that Z_1 contributes solely to the diagonal features in the spectra with both static and oscillatory terms. Z_4, being a ground state bleach term, contains only static terms that contribute to both the diagonal and off-diagonal features. The oscillatory diagonal terms cause the diagonal features to oscillate as a function of time, but with less contrast than the oscillatory features in the rephasing spectra. The diagonal features are maximized for t_{32} = 140 fs and minimized for t_{32} = 210 fs in the $\hat{\chi}^{(3)}_{+NRP}$ diagrams.

As discussed at the end of chapter II, the rephasing and non-rephasing spectra each contain mixed absorptive and dispersive contributions amongst the real and imaginary parts. If one wishes to separate absorptive and dispersive contributions from one another, it can be done by the linear transformation

$$\hat{\chi}^{(3)}_C \left(\omega_{21}, t_{32}, \omega_{43} \right) = \hat{\chi}^{(3)}_{NRP} \left(\omega_{21}, t_{32}, \omega_{43} \right) + \hat{\chi}^{(3)}_{RP} \left(\omega_{21}, t_{32}, -\omega_{43} \right). \tag{3.5}$$

The resulting two dimensional correlation spectra $\hat{\chi}^{(3)}_C$ has real and imaginary parts corresponding to absorptive and dispersive contributions to the third-order susceptibility, respectively.[8,9] In Fig. 3.7 we compare theoretical calculations (panels A-D) to our experimental results (panels E-H), and once again find excellent agreement. The left and right columns show the absorptive (real) and dispersive (imaginary) components of $\hat{\chi}^{(3)}_C$. By combining the rephasing and non-rephasing spectra, we create spectra in which all

four features oscillate as a function of the population time (though the off-diagonal features still oscillate to a larger degree of their maximum value), with maximized features in the data set for $t_{32} = 140$ fs and minimized in the $t_{32} = 210$ fs data set. The correlation spectra are related to the conditional probability that the system undergoes successive transitions at the frequencies ω_{21} and ω_{43}, separated by the population time t_{32}.

Summary

We have presented proof-of-principle results for 2D phase-modulation electronic coherence spectroscopy (PM-ECS), a novel fluorescence detected phase-selective technique for measuring 2D spectra with femtosecond resolution. We utilize acousto-optic phase modulation to generate a sequence of four collinear phase-related optical pulses which generate a multitude of coherences in the sample. We are able to isolate specific linear combinations of the fluorescence contributions that are linear with respect to each of the four excitation fields, often referred to as the rephasing and non-rephasing contributions. The time-domain data is Fourier transformed to generate 2D spectra that have excellent agreement with theoretical calculations. We will use this technique to obtain 2D spectral information in biologically relevant systems, such as molecular excitons created by porphyrin dimers, whose theoretical background and experimental results are presented in chapter VI.
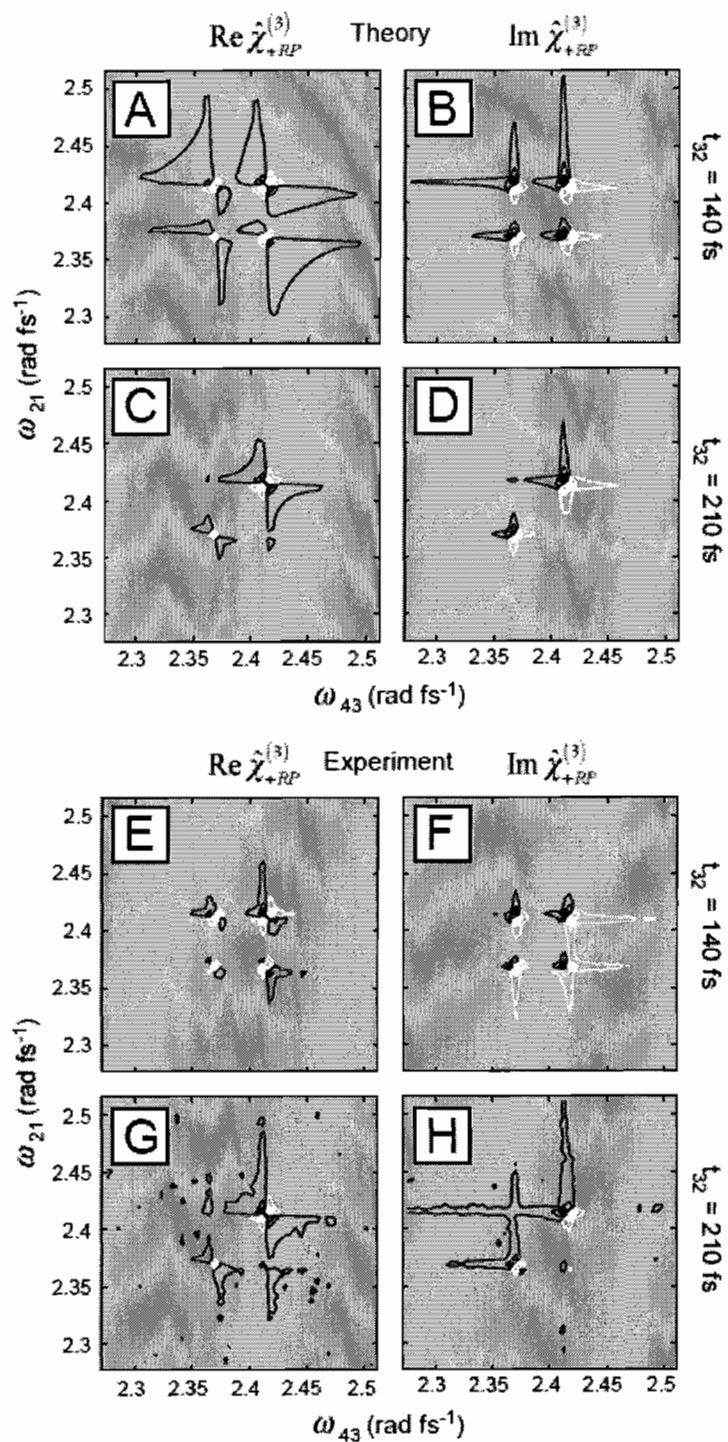
Figure 3.5: Comparison between theoretical calculations (panels (A) – (D)) and experimental data (panels (E) – (H)) for the rephasing susceptibility obtained by PM-ECS (described in text).
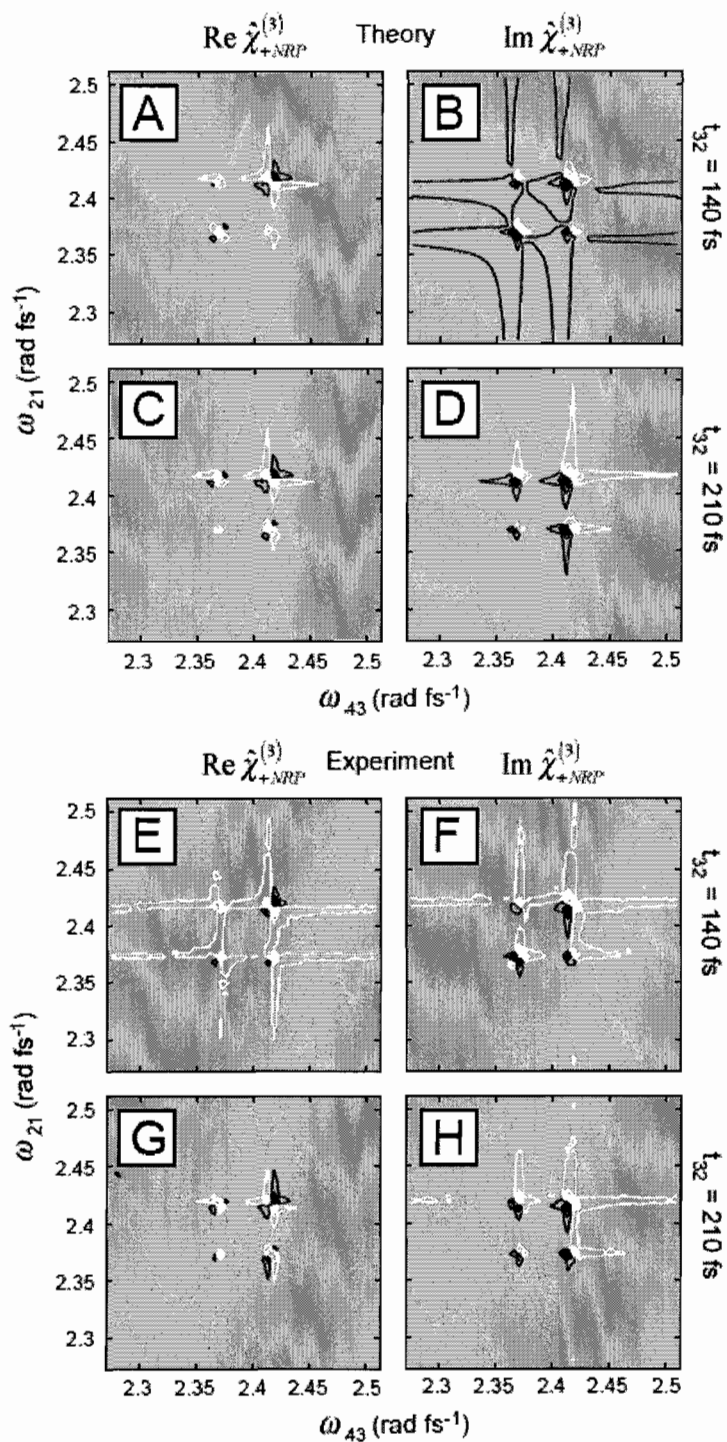
Figure 3.6: Comparison between theoretical calculations (panels (A) – (D)) and experimental data (panels (E) – (H)) for the non-rephasing susceptibility obtained by PM-ECS (described in text).
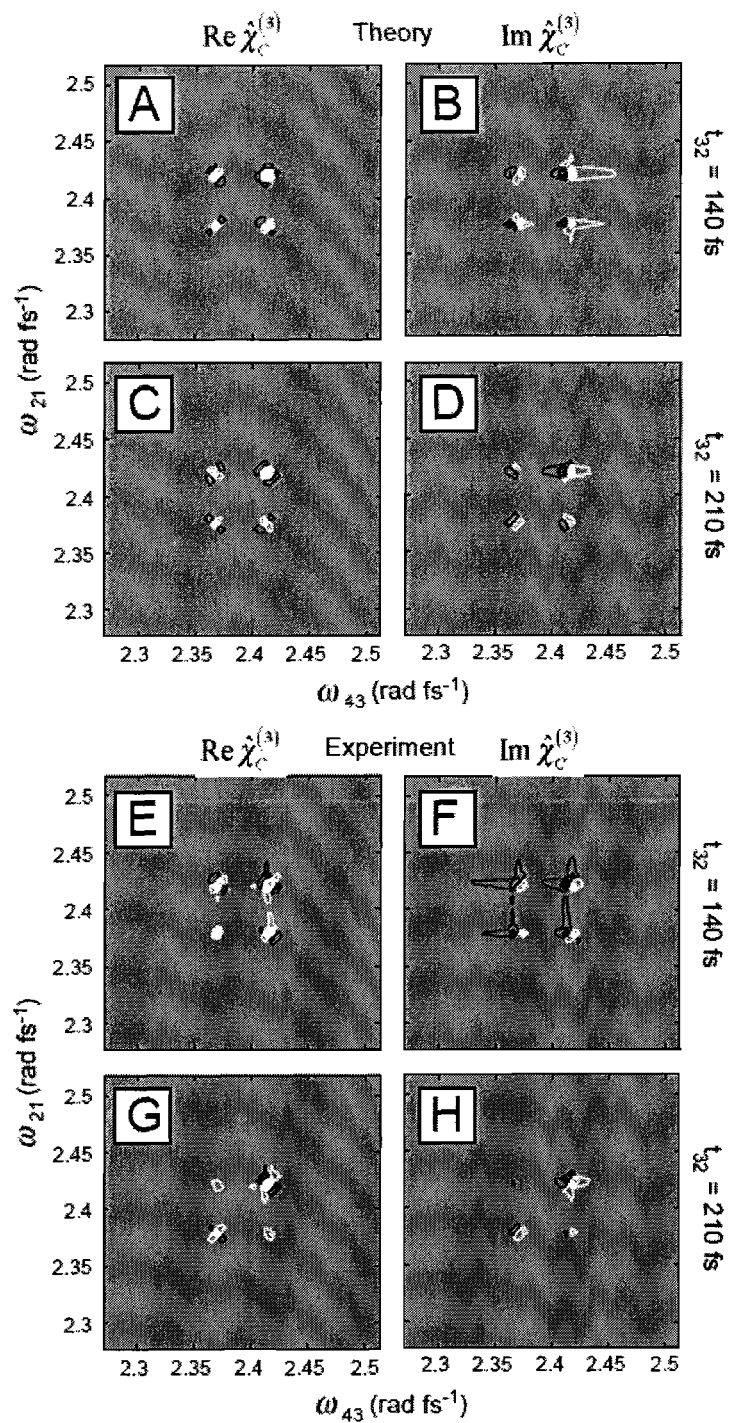
Figure 3.7: Comparison between theoretical calculations (panels (A) – (D)) and experimental data (panels (E) – (H)) for the two-dimensional correlation spectra obtained by PM-ECS (described in text).

CHAPTER IV

CONFORMATIONAL DYNAMICS OF BIOLOGICAL MACROMOLECULES BY

POLARIZATION-MODULATED FOURIER IMAGING CORRELATION

SPECTROSCOPY

Motivation

In the following experiments, we examine the slow polarized fluorescence

fluctuations that result from conformational transitions of DsRed, a multicolored

fluorescent protein derived from the coral *Discosoma sp*. Fluorescent proteins (FPs) are

widely used in biotechnological applications as reporters of gene expression and other

singular events of cell activity [1]. It has been hypothesized that FPs from reef-building

corals function as part of an adaptive mechanism to optically interact and to regulate the

symbiotic relationship between corals and photosynthetic algae [2]. It is therefore

interesting to examine the conformational transitions that affect the protein's ability to

transfer optical excitation energy. DsRed is an efficient fluorophore, with an

exceptionally high extinction coefficient ($\varepsilon = 3 \times 10^5$ cm^{-1} M^{-1}, $\lambda_{ex} \sim 532$ nm), orange-

red emission that is easily separated from excitation light, and a relatively high

fluorescence quantum yield ($q_f = 0.79$) [3]. Much is known about DsRed's structure [4-6], its

photo-physical properties [7-13], and its behavior as a molecular energy transfer complex [7, 8,]

[10, 11], making it a suitable system to demonstrate the utility of the polarization-modulation Fourier imaging correlation spectroscopy (PM-FICS) approach.

In the remainder of this paper we outline the basic experimental implementation of PM-FICS, including a brief theoretical description of the observables. Using DsRed as a model test system, we demonstrate how PM-FICS can separately and simultaneously measure partially averaged molecular center-of-mass and conformational coordinate fluctuations over a wide range of time scales (1 ms – 500 s) much longer than the excited state lifetime.

This chapter contains material co-authored with E.N. Senning, M.C. Fink, and A.H. Marcus.

Experimental Methods

In Fig. 4.1A is shown a schematic diagram of the PM-FICS apparatus. Additional details about instrumentation, sample preparation, and data collection are described by Fink *et al.* [14]. We cross left and right elliptically polarized laser beams to simultaneously generate an intensity interference fringe pattern and a linear polarization grating at the focal plane of a fluorescence microscope. The wave vector of the optical pattern $\mathbf{k}_G$ is oriented along the $\hat{\alpha}$ direction, as shown. The laser resonantly excites freely diffusing DsRed molecules in 95% glycerol / water solution (λ_{ex} = 532 nm, sample thickness ~ 10 μm, excitation intensity at sample = 1.27×10^{-4} $\mu W\,\mu m^{-2}$). The concentration of DsRed is dilute enough (~ 10 nM) so that the mean separation between molecules nearly matches the experimentally adjustable fringe spacing (d_G ~ 1 μm). The phase Φ of the

spatially modulated intensity pattern is swept at the frequency ~ 1 MHz, much faster than

a molecule can undergo a measurable change in its conformation, or in its center-of-mass

position, but much slower than the rate of fluorescence (τ_f ~ 3.2 ns) [10]. The back-emitted

fluorescence, which is detected through the focusing objective, is similarly modulated at

the sweep frequency. A polarizing beam splitter separates the emission into orthogonal

plane polarized channels, which are simultaneously and phase-synchronously detected.
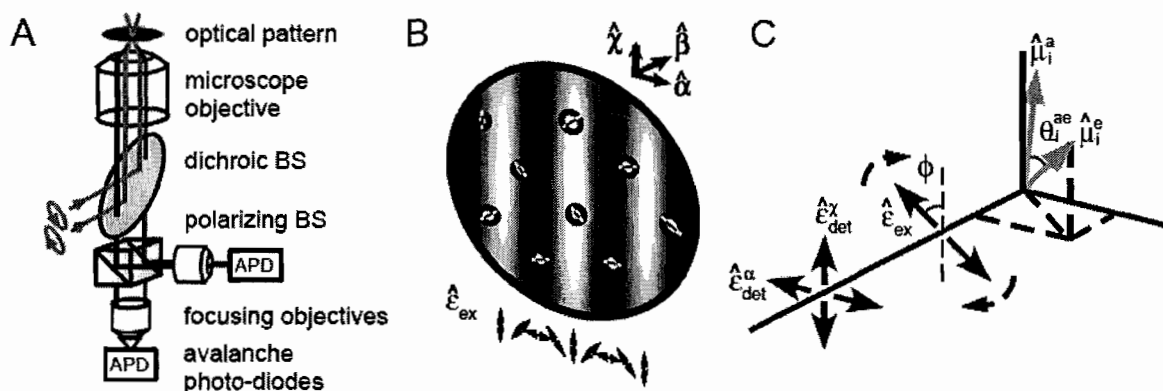
Figure 4.1: (A) Schematic of the experimental apparatus. Two orthogonal, elliptically polarized laser beams are crossed at the sample plane of a fluorescence microscope. The spatially and temporally integrated fluorescence is split using a polarizing beam-splitter (BS), and detected in parallel using avalanche photo-diodes. (B) At the sample, the superposition of the two laser beams creates (simultaneously) a spatially modulated intensity interference pattern and a plane polarization grating. A 180° rotation of the polarization vector coincides to a full cycle modulation of the intensity pattern. Molecular chromophores are depicted as white circles bisected by line segments, indicating the orientations of transition dipoles. (C) Each optical chromophore is characterized by its absorption and emission dipole moments ($\hat{\mu}_n^a$ and $\hat{\mu}_n^e$, respectively), and its depolarization angle θ_n^{ae}. The polarized emission is projected onto orthogonal laboratory frame axes. The rotating polarization of the exciting field imparts a modulation to the detected depolarization angle.

PM-FICS Observables and Theory for DsRed

Consider the fluorescence intensity from the nth DsRed molecule illuminated by the exciting laser beams (see Figs. 4.1B and 4.1C). If the molecule is initially excited at time $t = 0$, its fluorescence intensity at time t is proportional to [15]

$$\left\langle \left| \hat{\varepsilon}_{ex}(\phi) \cdot \hat{\mu}_n^a(0) \right|^2 \left| \hat{\varepsilon}_{det}^{\alpha,\chi} \cdot \hat{\mu}_n^e(t) \right|^2 \right\rangle. \tag{4.1}$$

Here, $\hat{\mu}_n^a$ and $\hat{\mu}_n^e$ are the absorption and emission transition dipole moments of optically coupled sites in the DsRed conformation, respectively. The angle brackets $\langle ... \rangle$ indicate an orientational average over the isotropic distribution of absorption and emission dipoles, assuming a fixed angle θ_n^{ae} between the two. We assume that the fluorescence lifetime ($\tau_f \sim 3.2$ ns) is much shorter than the rotational diffusion time of DsRed in 95% glycerol / water ($\tau_R \sim 100$ ns), the orientation of the emission dipole moment at the detection time is approximately the same as its orientation at the time of its excitation. Hence, it is assumed that $\hat{\mu}_n^e(t) \simeq \hat{\mu}_n^e(0)$. As shown in Fig. 4.1C, the unit vectors $\hat{\alpha}$, $\hat{\beta}$, and $\hat{\chi}$ define the laboratory frame coordinate system. The rotating excitation electric field direction $\hat{\varepsilon}_{ex}(\phi)$ lies in the $\hat{\alpha}$ - $\hat{\chi}$ plane, and is oriented relative to the $\hat{\chi}$-direction by the polar angle ϕ. The detection electric field directions, $\hat{\varepsilon}_{det}^{\alpha}$ and $\hat{\varepsilon}_{det}^{\chi}$, lie fixed and parallel to the $\hat{\alpha}$ - and $\hat{\chi}$-directions, respectively.

A standard approach is applied to calculate Eq. (4.1) for the experimental geometry [16]. First, it is necessary to calculate the probability $W(\theta,\varphi,\phi)d\theta d\varphi$ that the excited molecule has absorption dipole oriented with polar angle θ and azimuthal angle φ:

$$\left|\hat{\varepsilon}_{ex}(\phi)\cdot\hat{\mu}_n^a(\theta,\varphi)\right|^2 = W(\theta,\varphi,\phi)d\theta d\varphi = \frac{\cos^2(\theta+\phi)\sin\theta d\theta d\varphi}{\int_0^{2\pi}\int_0^{\pi}\cos^2(\theta+\phi)\sin\theta d\theta d\varphi}. \qquad (4.2)$$

The denominator of the above expression, $\int_0^{2\pi}\int_0^{\pi}\cos^2(\theta+\phi)\sin\theta d\theta d\varphi$ $=(-2\pi/3)\left[-3+\cos(2\phi)\right]$, counts over all possible orientations of $\hat{\mu}_n^a$. Note that this normalization recovers the standard value of $4\pi/3$ for $\phi=0$. In the remaining calculations, it is useful to approximate the factor $\left[-3+\cos(2\phi)\right]^{-1}$ using the truncated expansion $-\frac{1}{3}-\frac{1}{9}\cos(2\phi)$.

To obtain the probability of detecting the nth excited molecule's emission, polarized along the $\hat{\alpha}$- and $\hat{\chi}$-directions, one multiples Eq. (4.2) by the factor $\left|\hat{\varepsilon}_{det}^{\alpha,\chi}\cdot\hat{\mu}_n^e\right|^2$, and then integrates over all possible orientations. For the $\hat{\alpha}$-direction, this factor is equal to $\left[\sin(\theta+\theta_n^{ae})\cos\varphi\right]^2$; for the $\hat{\chi}$-direction, it is equal to $\cos^2(\theta+\theta_n^{ae})$. The integrated intensities are

$$A_n^\alpha\left(\theta_n^{ae},\phi\right)=\int_0^{2\pi}\int_0^\pi W\left(\theta,\varphi,\phi\right)\sin^2\left(\theta+\theta_n^{ae}\right)\cos^2\varphi\,d\theta d\varphi \tag{4.3}$$

and

$$A_n^\chi\left(\theta_n^{ae},\phi\right)=\int_0^{2\pi}\int_0^\pi W\left(\theta,\varphi,\phi\right)\cos^2\left(\theta+\theta_n^{ae}\right)d\theta d\varphi. \tag{4.4}$$

Equations (4.3) and (4.4) are tested for the case of vertical polarization ($\phi = 0$). Substitution of Eq. (4.2) into Eqs. (4.3) and (4.4), and using the normalization approximation stated above, leads to

$$A_n^\alpha\left(\theta_n^{ae},\phi=0\right)\simeq\frac{2}{9}-\frac{2}{45}\cos\left(2\theta_n^{ae}\right) \tag{4.5}$$

and

$$A_n^\chi\left(\theta_n^{ae},\phi=0\right)\simeq\frac{4}{9}+\frac{4}{45}\cos\left(2\theta_n^{ae}\right). \tag{4.6}$$

Equations (4.5) and (4.6) are first-order approximations to the exact solutions that would have been obtained [i.e., $A_n^\alpha\left(\theta_n^{ae},\phi=0\right)=\frac{1}{4}-\frac{1}{20}\cos\left(2\theta_n^{ae}\right)$ and $A_n^\chi\left(\theta_n^{ae},\phi=0\right)$

$$= \frac{1}{2} + \frac{1}{10}\cos\left(2\theta_n^{ae}\right)]$$ had the approximation to the normalization factor not been used.

Equations (4.3) and (4.4) are next evaluated for the general case $\phi \neq 0$.

$$A_n^\alpha\left(\theta_n^{ae},\Phi\right) \simeq \left|\hat{\mu}_n^a\right|^2 \left|\hat{\mu}_n^e\right|^2 \left[\frac{17}{72} + \frac{23}{360}\cos\left(2\theta_n^{ae}\right) - \frac{1}{9}\cos\left(2\theta_n^{ae} - \Phi\right) + \frac{1}{45}\cos\left(2\theta_n^{ae} + \Phi\right)\right.$$

$$\left. - \frac{1}{72}\cos\left(2\Phi\right) - \frac{1}{48}\cos\left(2\theta_n^{ae} - 2\Phi\right) + \frac{1}{720}\cos\left(2\theta_n^{ae} + 2\Phi\right)\right],$$

(4.7)

and

$$A_n^\chi\left(\theta_n^{ae},\Phi\right) \simeq \left|\hat{\mu}_n^a\right|^2 \left|\hat{\mu}_n^e\right|^2 \left[\frac{17}{36} - \frac{23}{180}\cos\left(2\theta_n^{ae}\right) + \frac{2}{9}\cos\left(2\theta_n^{ae} - \Phi\right) - \frac{2}{45}\cos\left(2\theta_n^{ae} + \Phi\right)\right.$$

$$\left. - \frac{1}{36}\cos\left(2\Phi\right) + \frac{1}{24}\cos\left(2\theta_n^{ae} - 2\Phi\right) - \frac{1}{360}\cos\left(2\theta_n^{ae} + 2\Phi\right)\right].$$

(4.8)

In Eqs. (4.7) and (4.8), the excitation polarization angle ϕ is expressed in terms of the phase of the intensity grating, $\Phi = 2\phi$. In the current experiments, a linear sweep is applied to the phase Φ at the frequency $\Omega/2\pi \sim 1$ MHz. Equations (4.7) and (4.8) show that the polarized intensities contain oscillating terms at the modulation frequency and at twice the modulation frequency.

In a FICS experiment the optical fringe spacing, d_g, is typically between 0.5 and 5 μm. The beam waist w at the sample plane, on the order of 50-100 μm, typically spans at

least ten fringe spacings. Since $w >> d_g$, we can approximate the excitation intensity pattern as an infinite plane wave, $I_L(\mathbf{r},\phi_G) = I_0\left[1+\cos\left(\mathbf{k}_G \cdot \mathbf{r}+\phi_G\right)\right]$. Here, we define I_0 as the amplitude of the intensity grating, ϕ_G is the intensity grating phase, and $k_G = \left(2\pi/d_G\right)$ is the wavevector of the intensity grating. The total fluorescence collected from the N molecules is given by [14]

$$I_f^{\alpha,\chi} = \int_{-\infty}^{\infty} I_L(\mathbf{r},\Phi)n^{\alpha,\chi}(\mathbf{r},\theta^{ae})d\mathbf{r}, \qquad (4.9)$$

where

$$n^{\alpha,\chi}(\mathbf{r},\theta^{ae}) = \frac{1}{V}\sum_{n=1}^{N} A_n^{\alpha,\chi}(\theta_n^{ae})\delta(\theta^{ae}-\theta_n^{ae})\delta(\mathbf{r}-\mathbf{r}_n). \qquad (4.10)$$

is the polarization-dependent optical density of the sample. We can see that the total fluorescence collected is proportional to the spatial overlap of the excitation fringe pattern and the fluorescent particle sites. Carrying out the spatial integration leads to

$$I_f^{\alpha,\chi}(\mathbf{k}_G,\Phi) = \frac{I_0}{V}\sum_{n=1}^{N} A_n^{\alpha,\chi}(\theta_n^{ae},\Phi)\left[1+\cos\left(\mathbf{k}_G \cdot \mathbf{r}_n+\Phi\right)\right]. \qquad (4.11)$$

The phase $\Phi(t') = \Omega t' + \Phi_0$ is swept at the carrier frequency $\Omega/2\pi = 1$ MHz. The period of the modulation is much longer than the fluorescence lifetime and the rotational

reorientation time, but short in comparison to the center-of-mass and conformational fluctuations of interest.

Substitution of Eqs. (4.7) and (4.8) into Eq. (4.9), and retaining only the terms that are third-order in Φ leads to

$$I_f^\alpha\left(k_G,\Phi\right) \propto \frac{1}{6}\cos\left(k_G x_n + 3\Phi\right) + \frac{1}{4}\cos\left(k_G x_n - 2\theta_n^{ae} + 3\Phi\right) - \frac{1}{60}\cos\left(k_G x_n + 2\theta_n^{ae} + 3\Phi\right) \tag{4.12}$$

and

$$I_f^\chi\left(k_G,\Phi\right) \propto \frac{1}{3}\cos\left(k_G x_n + 3\Phi\right) - \frac{1}{2}\cos\left(k_G x_n - 2\theta_n^{ae} + 3\Phi\right) + \frac{1}{30}\cos\left(k_G x_n + 2\theta_n^{ae} + 3\Phi\right) \tag{4.13}$$

Using phase sensitive detection techniques described in reference [14], the above signals are demodulated at three times the carrier frequency. One thus determines the in-phase [$X_{k_G}^{\alpha,\chi} = I_f^{\alpha,\chi}\left(k_G, 3\Phi = 0\right)$] and in-quadrature [$Y_{k_G}^{\alpha,\chi} = I_f^{\alpha,\chi}\left(k_G, 3\Phi = \pi/2\right)$] projections of the polarized fluorescence. These components are combined according to $Z_{k_G}^{\alpha,\chi} = X_{k_G}^{\alpha,\chi} + iY_{k_G}^{\alpha,\chi}$ to obtain the complex-valued signals

$$Z_{k_G}^\alpha \propto \frac{1}{6}\exp i\left(\mathbf{k}_G \cdot \mathbf{r}_n\right) + \frac{1}{4}\exp i\left(\mathbf{k}_G \cdot \mathbf{r}_n - 2\theta_n^{ae}\right) - \frac{1}{60}\exp i\left(\mathbf{k}_G \cdot \mathbf{r}_n - 2\theta_n^{ae}\right) \tag{4.14}$$

and

$$Z^{\chi}_{k_G} \propto \frac{1}{3}\exp i\left(\mathbf{k}_G \cdot \mathbf{r}_n\right) - \frac{1}{2}\exp i\left(\mathbf{k}_G \cdot \mathbf{r}_n - 2\theta^{ae}_n\right) + \frac{1}{30}\exp i\left(\mathbf{k}_G \cdot \mathbf{r}_n - 2\theta^{ae}_n\right). \qquad (4.15)$$

Because the final three terms of Eqs. (4.14) and (4.15) are small in comparison to the leading terms, the complex signals are well approximated by

$$Z^{\alpha}_{\mathbf{k}_G} \simeq \frac{I_0}{V}\sum_{n=1}^{N}\left|\hat{\mu}^a_n\right|^2\left|\hat{\mu}^e_n\right|^2\left[\tfrac{1}{6}\exp i\left(\mathbf{k}_G \cdot \mathbf{r}_n\right) + \tfrac{1}{4}\exp i\left(\mathbf{k}_G \cdot \mathbf{r}_n - 2\theta^{ae}_n\right)\right] \qquad (4.16)$$

and

$$Z^{\chi}_{\mathbf{k}_G} \simeq \frac{I_0}{V}\sum_{n=1}^{N}\left|\hat{\mu}^a_n\right|^2\left|\hat{\mu}^e_n\right|^2\left[\tfrac{1}{3}\exp i\left(\mathbf{k}_G \cdot \mathbf{r}_n\right) - \tfrac{1}{2}\exp i\left(\mathbf{k}_G \cdot \mathbf{r}_n - 2\theta^{ae}_n\right)\right].$$

$$(4.17)$$

In Eqs. (4.16) and (4.17), $\hat{\mu}^a_n$ and $\hat{\mu}^e_n$ are the absorption and emission transition dipole moments of optically coupled sites in the DsRed conformation, and θ^{ae}_n is the angle (assumed fixed on the time scale of fluorescence) between the two dipole moments. The two transition dipoles are assumed to couple via a resonant incoherent Förster mechanism. Because the fluorescence lifetime ($\tau_f \sim 3.2$ ns) is much shorter than the rotational diffusion time of DsRed in 95% glycerol / water (viscosity ~ 780 cP, $\tau_R \sim 100$ ns), the polarized fluorescence signals do not depend on the rotational diffusion of DsRed, but are sensitive to the conformation angle θ^{ae}_n.

Linear combinations of Eqs. (4.16) and (4.17) are used to isolate either the first or second of the two terms. The local number density observable $Z_{k_G}^{ND} \equiv Z_{\mathbf{k}_G}^{\chi} + 2Z_{\mathbf{k}_G}^{\alpha} \propto \langle \exp i(k_G x) \rangle$, and the local anisotropy density observable $Z_{k_G}^{AD} \equiv Z_{\mathbf{k}_G}^{\chi} - 2Z_{\mathbf{k}_G}^{\alpha} \propto \langle \exp i(k_G x - 2\theta^{ae}) \rangle$ are thus defined, where the angle brackets indicate the sum over N molecules. As discussed further below, the complex signals contain information about partially averaged molecular center-of-mass and anisotropy coordinates.

Cumulant Approximation

We assign a microscopic interpretations to the number density and the anisotropy density using standard methods of statistical mechanics and probability theory [17, 18]. It is convenient to begin with a discussion of the number density. In the FICS experiment, the parameter $Z_{k_G}^{ND}(t)$ is sequentially sampled over time. Because the grating wave vector $\mathbf{k}_G$ points in the $\hat{\alpha}$-direction, only the x-components of the N molecular center-of-mass positions contribute to the signal. The positions $\{x_1(t), x_2(t), ..., x_N(t)\}$ behave as continuous random variables, and fluctuate about their mean according to $x_n(t) = \delta x_n(t) + \langle x \rangle_{eq}$. We define the equilibrium probability $P_{eq}(x)$ of observing a randomly selected molecule with coordinate x, with mean $\langle x \rangle_{eq} = \int_{-\infty}^{\infty} x P_{eq}(x) dx = 0$ and variance $\sigma_{eq}^2 = \int_{-\infty}^{\infty} x^2 P_{eq}(x) dx$. At a given instant, the FICS observable samples a Fourier

73

component of a subset $P_N[x;t] = \frac{1}{N}\sum_{n=1}^{N} A_n(t)\delta[x - x_n(t)]$ of the equilibrium

distribution. According to the central limit theorem, the sampled distribution has mean

value $\bar{x}_N(t) = \int_{-\infty}^{\infty} x P_N[x_n;t]dx = \frac{1}{N}\sum_{n=1}^{N} x_n(t)A_n(t)$ and variance $\sigma_N^2 = \left[\delta\bar{x}_N(t)\right]^2$

$= \sum_{n=1}^{N} x_n^2(t)A_n(t) \propto \sigma_{eq}^2/N$, which is narrowed relative to the equilibrium distribution by

the factor N^{-1} [17]. The number density fluctuation $Z_{k_G}^{ND}(t)$ is the Fourier transform (also

known as the characteristic function) of the sampled distribution $P_N[x;t]$. We

approximate $Z_{k_G}^{ND}(t)$ using a cumulant expansion of the sampled distribution, truncated

to second order [17]:

$$Z_{k_G}^{ND}(t) \simeq \exp\left\{ik_G\bar{x}_N(t) - \frac{1}{2}k_G^2\left[\delta\bar{x}_N(t)\right]^2\right\}. \tag{4.18}$$

For the current situation in which center-of-mass motion is expected to occur through a

free diffusion mechanism, the above approximation is expected to be accurate, since the

equilibrium distribution is well characterized as Gaussian [18]. In such cases, higher-order

moments of $P_{eq}(x)$ are negligible. Equation (4.18) expresses the phase and amplitude of

$Z_{k_G}^{ND}(t)$ in terms of the mean value and the variance of the sampled distribution $P_N[x;t]$,

respectively. Thus, in the cumulant approximation the number density samples the

distribution size N, and the deviation of the sampled mean position about the equilibrium

distribution, $\delta\bar{x}_N(t) = \bar{x}_N(t) - \langle x\rangle_{eq}$.

In analogy to the above treatment for the number density, an approximation for the anisotropy density is

$$Z_{k_G}^{AD}(t) \simeq \exp\left\{ i\left[k_G \bar{x}_N(t) + 2\bar{\theta}_N^{ae}(t) \right] - \frac{1}{2}\left[k_G \delta\bar{x}_N(t) + 2\delta\bar{\theta}_N^{ae}(t) \right]^2 \right\}. \tag{4.19}$$

Similar interpretations apply to the phase and amplitude of $Z_{k_G}^{AD}(t)$ as to those for the number density, but with the additional contributions from the mean depolarization angle of the sampled distribution $\bar{\theta}_N^{ae}(t) = \sum_{n=1}^{N} \theta_n^{ae}(t) P_N\left[\theta_n^{ae}(t) \right]$ and the variance $\left[\delta\bar{\theta}_N^{ae}(t) \right]^2$. The argument of Eq. (4.19) generally contains coupling terms proportional to $k_G^2 \left[\delta\bar{x}_N(t) \right]^2 \left[\delta\bar{\theta}_N^{ae}(t) \right]^2$. Such terms vanish if it is assumed that the molecular center-of-mass positions are statistically uncorrelated with the depolarization angles. In this case, an additional approximation for the anisotropy density is given by $Z_{k_G}^{AD}(t) = Z_{k_G}^{ND}(t) Z^A(t)$, where the anisotropy is defined by $Z^A(t) \equiv Z_{k_G}^{AD}(t) / Z_{k_G}^{ND}(t) \propto \left\langle \exp i\left[2\theta_n^{ae}(t) \right] \right\rangle$. This factorization is invoked for the remainder of the paper. While both the number density and the anisotropy density are k_G-dependent, the anisotropy depends only on internal molecular degrees of freedom, and is independent of the specifically probed length scale.

The accuracy of the approximations given by Eqs. (4.18) and (4.19) depends on the relative importance of higher moments of the equilibrium distributions, $P_{eq}(x)$ and

$P_{eq}(\theta^{ae})$. Were the equilibrium distributions nearly Gaussian, their higher moments would be small, and in such cases the second-order cumulant is an adequate model. For distributions with greater complexity, the second order cumulant approximation does not necessarily account for signal contributions from non-zero higher moments. Nevertheless, such higher moments may be less important when considering the time-dependent fluctuations of the optical signals. This point can be investigated through computer simulation and experiment. In the current study, we regard equations (4.18) and (4.19) as convenient starting points for the development of future models to interpret PM-FICS data.

Two-Point Time Correlation and Distribution Functions

Two-point time-correlation functions (TCFs) provide a useful characterization of the average time intervals over which statistically correlated events occur in equilibrium systems [18]. The TCF of the complex-valued operator $Z(t)$ is defined as

$\langle Z^*(0) Z(t_{21}) \rangle = \lim_{\tau \to \infty} \frac{1}{\tau} \int_0^\tau Z^*(t') Z(t_{21} + t') dt'$, where the angle brackets indicate the

integration over time, and $t_{21} = t_2 - t_1 \geq 0$ is the time interval separating two successive measurements. Using the cumulant approximations of Eqs. (4.18) and (4.19), the number density and the anisotropy density TCFs are written

$$C_{ND}^{(2)}(t_{21}) = \langle Z_{k_G}^{ND*}(0) Z_{k_G}^{ND}(t_{21}) \rangle = \langle \exp\left[-\tfrac{1}{2} k_G^2 \delta \Delta \bar{x}_N^2(t_{21})\right] \rangle \langle \exp i\left[k_G \Delta \bar{x}_N(t_{21})\right] \rangle \qquad (4.20)$$

and

$$C_{AD}^{(2)}(t_{21}) = \left\langle Z_{k_G}^{AD*}(0) Z_{k_G}^{AD}(t_{21}) \right\rangle = C_{ND}^{(2)}(t_{21})\, C_A^{(2)}(t_{21}). \qquad (4.21)$$

The second term on the right hand side of Eq. (4.21) is the anisotropy TCF, given by

$$C_A^{(2)}(t_{21}) = \left\langle Z^{A*}(0) Z^A(t_{21}) \right\rangle = \left\langle \exp\left[-2\delta\Delta\bar{\theta}_N^{ae2}(t_{21})\right]\right\rangle \left\langle \exp i\left[2\Delta\bar{\theta}_N^{ae}(t_{21})\right]\right\rangle. \qquad (4.22)$$

Equation (4.20) defines the mean center-of-mass displacement $\Delta\bar{x}_N(t_{21}) = \bar{x}_N(t_{21}) - \bar{x}_N(0)$ of the sampled distribution during the time interval t_{21}, and the variance $\delta\Delta\bar{x}_N^2(t_{21}) = \left[\Delta\bar{x}_N(t_{21})\right]^2$. Similar definitions hold for the mean depolarization displacement $\Delta\bar{\theta}_N^{ae}(t_{21})$ and its variance $\delta\Delta\bar{\theta}_N^{ae2}(t_{21})$ given by Eq. (4.22). Equations (4.20) – (4.22) assume statistical independence between the means and variances of the sampled distributions. The TCFs are generally complex-valued, with phase factors that depend on the mean coordinate displacements, and amplitudes that depend on the variances. These functions decay, on average, on a time scale for which the magnitude of the phase displacement exceeds $\sim \pi/4$. The number density TCF described by Eq. (4.20) is known as the self-part of the intermediate scattering function of liquid state theory. In the absence of long range molecular interactions, this expression can be further simplified using the Gaussian model for single particle motion [18]. In this approximation, Eq. (4.20) becomes $C_{ND}^{(2)}(t_{21}) \propto \exp\left[-k_G^2 D_S t_{21}\right]$, where D_S is the self-

diffusion coefficient. Equation (4.21) suggests that the anisotropy TCF can be determined by the ratio $C_{AD}^{(2)}(t_{21})/C_{ND}^{(2)}(t_{21})$.

While TCFs convey the average time scales of molecular coordinate displacements, more detailed information about the weights and magnitudes of the sampled displacements are contained in two-point distribution functions (DFs). We define $P_N^{(2)}\left[\Delta \bar{x}_N(t_{21})\right]d\Delta \bar{x}_N$ as the probability of sampling N molecules whose mean center-of-mass coordinate has undergone a displacement in the range $\Delta \bar{x}_N$ and $\Delta \bar{x}_N + d\Delta \bar{x}_N$, during the time interval t_{21}. We construct this distribution by sampling pair-wise products of the form $Z_{k_G}^{ND*}(0)Z_{k_G}^{ND}(t_{21})$

$$= \exp\left[-\tfrac{1}{2}k_G^2\delta\Delta\bar{x}_N^2(t_{21})\right]\exp i\left[k_G\Delta\bar{x}_N(t_{21})\right].$$ From the two-point products we compile histograms of the displacements $\Delta \bar{x}_N(t_{21})$, weighted by the sampled inverse variance ($\propto N$). Referring to the central limit theorem, if $\Delta \bar{x}_N(t)$ behaves as a Gaussian random variable, $P_N^{(2)}\left[\Delta \bar{x}_N(t_{21})\right]$ is expected to be Gaussian with center $\langle\Delta \bar{x}_N\rangle = 0$. Furthermore, the variance of this distribution should scale linearly with time according to $\delta\Delta\bar{x}_N^2(t_{21}) = 2D_s t_{21}$, in analogy to the self-part of the van Hove function [18].

We similarly define the joint probability $P_N^{(2)}\left[\Delta \bar{x}_N(t_{21}); \Delta \bar{\theta}_N^{ae}(t_{21})\right]$ of sampling N molecules with mean depolarization angle $\Delta \bar{\theta}_N^{ae}(t_{21})$ and mean displacement $\Delta \bar{x}_N(t_{21})$ during the time interval t_{21}. $P_N^{(2)}\left[\Delta \bar{x}_N(t_{21}); \Delta \bar{\theta}_N^{ae}(t_{21})\right]$ is constructed from the anisotropy density according to $Z_{k_G}^{AD*}(0)Z_{k_G}^{AD}(t_{21}) = Z_{k_G}^{ND*}(0)Z_{k_G}^{ND}(t_{21}) Z^{A*}(0)Z^A(t_{21})$, where we

assume no correlation between molecular positions and depolarization angles. An absence of coupling between the parameters $\Delta \bar{x}_N (t_{21})$ and $\Delta \bar{\theta}_N^{ae} (t_{21})$ implies that $P_N^{(2)} \left[\Delta \bar{x}_N (t_{21}); \Delta \bar{\theta}_N^{ae} (t_{21}) \right] = P_N^{(2)} \left[\Delta \bar{x}_N (t_{21}) \right] P_N^{(2)} \left[\Delta \bar{\theta}_N^{ae} (t_{21}) \right]$. The DF for the anisotropy fluctuations is thus determined by the ratio $P_N^{(2)} \left[\Delta \bar{\theta}_N^{ae} (t_{21}) \right]$ $= P_N^{(2)} \left[\Delta \bar{x}_N (t_{21}); \Delta \bar{\theta}_N^{ae} (t_{21}) \right] / P_N^{(2)} \left[\Delta \bar{x}_N (t_{21}) \right]$.

DsRed Results and Discussion

In Fig. 4.2 are shown experimental trajectories of the continuously sampled observables $Z_{k_G}^{ND} (t)$ and $Z_{k_G}^{AD} (t)$ taken at acquisition frequency 1 kHz, and with fringe spacing $d_G = 1.06 \ \mu$m. Data runs were recorded over a period of 512 s. As in our previous work, [14] signal count rates were typically in the range 250,000 – 400,000 cps using laser excitation intensity (measured at the sample) of $1.27 \times 10^{-4} \ \mu$W μm^{-2}. In the left column are shown the number density, and in the right column, the anisotropy density. In panels 4.2A and 4.2B, the observables are presented in terms of their corresponding phases, while in panels 4.2C – 4.2F, they are represented as real and imaginary parts. As shown in Fig. 4.2A, fluctuations of the mean center-of-mass coordinate on the order of $\sim$ 10 nm are discernible. Similarly, Fig. 4.2B shows that fluctuations of the phase of the anisotropy density on the order of $\sim$ 2° can be resolved. While both $Z_{k_G}^{ND} (t)$ and $Z_{k_G}^{AD} (t)$ exhibit rapid sub-second fluctuations, the anisotropy density contains at least one additional, slowly varying contribution on the time scale of
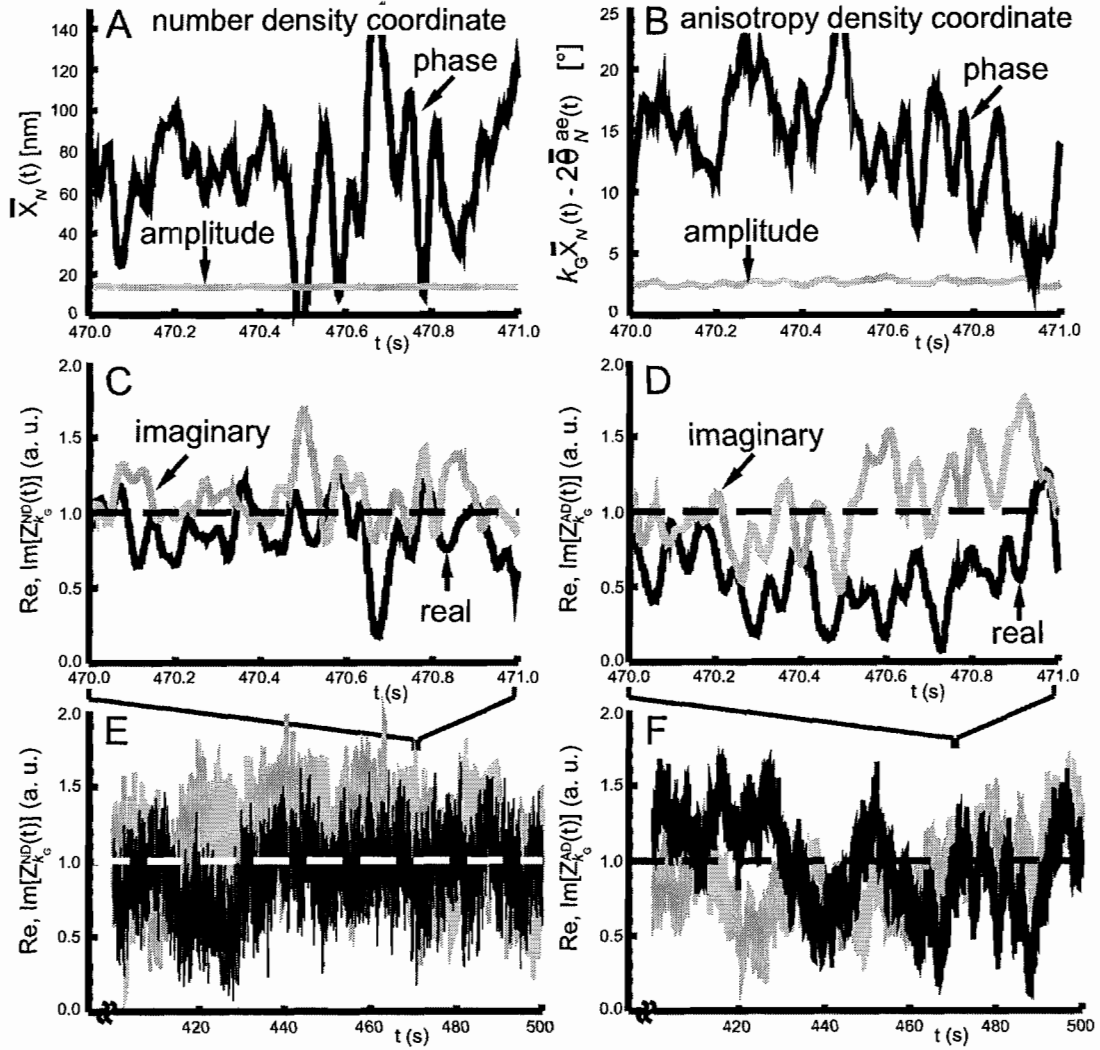
Figure 4.2: Experimental trajectories of the number density fluctuation $Z_{k_G}^{ND}(t)$ and the anisotropy density fluctuation $Z_{k_G}^{AD}(t)$, constructed from the demodulated polarized fluorescence signals, with $d_G = 2.12$ μm. These measurements are recorded from a 10 nM solution of DsRed in 95% glycerol / water, at a frequency of 1 kHz, and over an acquisition period of 512 s. In panels (E) and (F), the final 100 seconds of the data run are shown. In panels (A) – (D), the time axis is expanded to show the variation over a 1 second time window. In panels (A) and (B), the signals are represented in terms of the amplitudes and phases. In panels (C) – (F), the two signal quadratures are shown.

several seconds. From Figs. 4.2E and 4.2F, it appears that photo-bleaching of the signal is not significant over the 512 s data acquisition period.

Following the numerical procedure described by Fink et al. [14], we calculate the number density and anisotropy density TCFs, defined by Eqs. (4.20) and (4.22). These calculations were repeated using independently acquired data sets, to insure their reproducibility. The TCFs are presented in Figs. 4.3A and 4.3B, displaced vertically for the five different fringe spacings d_G = 1.6, 1.75, 2.12, 2.56, and 2.92 μm. In Fig. 4.3A, the decays for $C_{ND}^{(2)}(t_{21})$ (black curves) are compared to model curves for single particle diffusion (white). The model curves are given by the function $\exp(-k_G^2 D_S t_{21})$ where the value used for the self-diffusion coefficient ($D_S = 3.7 \times 10^{-10}$ cm^2 s^{-1}) is consistent with previous measurements of DsRed self-diffusion in 95% glycerol / water solution [14]. For each of the five fringe spacings, the time constants of the decays increase with increasing length scale. The excellent agreement between data and the Gaussian model strongly suggests that molecular interactions are negligible, and that center-of-mass motions are uncorrelated. The assumption that the two coordinate displacements $\Delta \bar{x}_N(t_{21})$ and $\Delta \bar{\theta}_N^{ae}(t_{21})$ are statistically uncorrelated is tested by comparing results for $C_{AD}^{(2)}(t_{21})$ to model decays, which account for the factorization between the anisotropy and the number density [see Eq. (4.21)]. For this purpose, a single exponential decay, $\exp(-t_{21}/\tau_A)$, is used to represent the anisotropy TCF $C_A^{(2)}(t_{21})$. In Fig. 4.3B, results for $C_{AD}^{(2)}(t_{21})$ are compared to the model decays, $\exp\left[-\left(k_G^2 D_S + \frac{1}{\tau_A}\right)t_{21}\right]$, with $\tau_A = 8$ s. Note that the TCFs
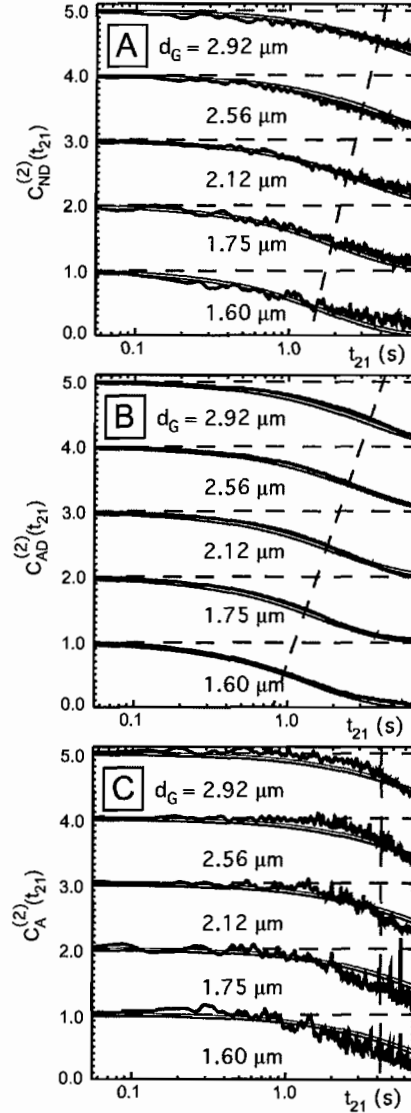
Figure 4.3: Fringe spacing dependent two-point time-correlation functions (2P-TCFs) of the number density and the anisotropy density fluctuations, $C_{ND}^{(2)}(t_{21})$ and $C_{AD}^{(2)}(t_{21})$, respectively. Decays corresponding to different values of the fringe spacing d_G are vertically displaced. Diagonal and vertical dashed lines are guides to the eye to roughly indicate the decay time scale. In panel (A), we compare $C_{ND}^{(2)}(t_{21})$ to the Gaussian model for Fickian diffusion $\exp(-k_G^2 D_s t_{21})$, where $D_S = 3.7 \times 10^{-10}$ cm^2 s^{-1}. In panel (B), we compare $C_{AD}^{(2)}(t_{21})$ to the function $\exp\left[-\left(k_G^2 D_s + \frac{1}{\tau_A}\right)t_{21}\right]$, where $\tau_A = 8$ s is the average time scale of the anisotropy decay, due to protein conformation fluctuations that affect energy transfer efficiency. In panel (C), we compare the ratio of the data shown in panels (A) and (B), $C_A^{(2)}(t_{21}) = C_{AD}^{(2)}(t_{21})/C_{ND}^{(2)}(t_{21})$, to the model decay $\exp(-t_{21}/\tau_A)$.

$C_{AD}^{(2)}(t_{21})$ decay more rapidly than $C_{ND}^{(2)}(t_{21})$, and that the agreement between data and model curves is very good for all values of d_G. In Fig. 4.3C, the ratio of the decays $C_{AD}^{(2)}(t_{21})/C_{ND}^{(2)}(t_{21}) = C_A^{(2)}(t_{21})$, are compared to the model function $\exp(-t_{21}/\tau_A)$. The very favorable agreement between these results for $C_A^{(2)}(t_{21})$ and the single-exponential decay demonstrates a clear separation between the anisotropy and center-of-mass fluctuations. The value obtained for the relaxation time $\tau_A = 8$ s suggests this is the average time scale for internal conformational fluctuations of DsRed.

In Fig. 4.4 are presented DFs of the mean center-of-mass displacement $P_N^{(2)}\left[\Delta\bar{x}_N(t_{21})\right]$, and the depolarization angle $P_N^{(2)}\left[\Delta\bar{\theta}_N^{ae}(t_{21})\right]$. These DFs are constructed from the observables $Z_{k_G}^{ND}(t)$ and $Z_{k_G}^{AD}(t)$, measured with fringe spacing d_G = 2.12 μm. In both panels are shown the distributions vertically displaced for three different values of the time interval t_{21}. The sampled distributions are symmetric and centered about the origin, and their widths increase as a function of t_{21}. In Fig. 4.4A, the sampled distributions $P_N^{(2)}\left[\Delta\bar{x}_N(t_{21})\right]$ are compared to the self-part of the van Hove correlation function $G_S\left(\Delta\bar{x}_N, t_{21}\right) = \left(4\pi D t_{21}\right)^{-3/2}\exp\left(-\Delta\bar{x}_N^2/4D_s t_{21}\right)$ (dashed gray curves), where the value of D_S is the same as that used above for the model calculations of the number density TCF. The very good agreement between the van Hove function and the DF suggests that the Gaussian model provides an accurate picture of molecular self-diffusion in the DsRed system. It is important to emphasize that the comparison between theory and measurement at the level of the DFs is a more stringent test of the Gaussian
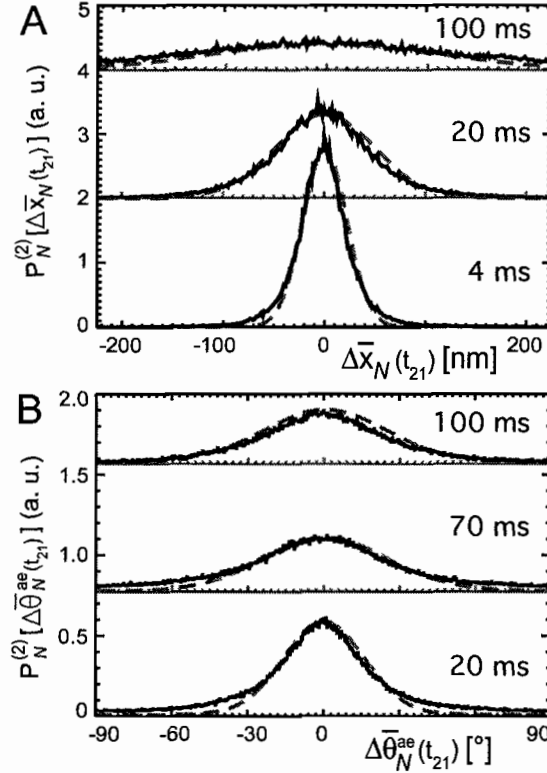
Figure 4.4: Two-point distribution functions of (A) the mean sampled center-of-mass displacement and (B) the mean sampled displacement of the depolarization angle. In each panel are shown distributions vertically displaced for three different time intervals. In panel (A) are comparisons between the measured distribution (black) and the self-part of the van Hove correlation function $G_S\left(\Delta\bar{x}_N, t_{21}\right) \propto \exp\left(-\Delta\bar{x}_N^2/4D_S t_{21}\right)$ with $D_S = 3.7$ $\times 10^{-10}$ cm^2 s^{-1}, (gray dashed curves). In panel (B), the distributions are compared to Gaussians with standard deviations 15.7°, 23°, and 23°.

model than the previous comparison at the level of the TCFs. The TCFs represent a statistical average over the distribution of sampled displacements, according to $C_{ND}^{(2)}\left(t_{21}\right)$

$$= \int_{-\infty}^{\infty} \exp\left[-\tfrac{1}{2}k_G^2 \delta\Delta\bar{x}_N^2\left(t_{21}\right)\right] \exp i\left[k_G \Delta\bar{x}_N\left(t_{21}\right)\right] P_N^{(2)}\left[\Delta\bar{x}_N\left(t_{21}\right)\right] d\Delta\bar{x}_N\left(t_{21}\right).$$ The DFs

provide dynamical information that is often obscured in the TCFs by the statistical

average. In Fig. 4.4B is shown the DF of the mean depolarization angle $P_N^{(2)}\left[\Delta\bar{\theta}_N^{ae}\left(t_{21}\right)\right]$.

Although this distribution is approximately Gaussian for the time intervals shown, the width of the distributions ceases to broaden on time scales greater than ~ 70 ms.

Summary

In this work, a novel phase-selective fluorescence fluctuation method, polarization-modulated Fourier imaging correlation spectroscopy (PM-FICS), was applied to simultaneously monitor molecular center-of-mass and anisotropy fluctuations. This approach allows for the study of internal conformational fluctuations of the fluorescent protein complex DsRed in the presence of diffusion. The phase-selectivity of PM-FICS enables the determination of two-point distribution functions (DFs) and time-correlation functions (TCFs).

Direct observations of the number density and the anisotropy density fluctuations, $Z_{k_G}^{ND}(t)$ and $Z_{k_G}^{AD}(t)$, show that thermally driven relaxation processes in DsRed occur over a broad range of time scales. A fringe spacing dependent analysis of the TCFs, $C_{ND}^{(2)}(t_{21})$, $C_{AD}^{(2)}(t_{21})$ and $C_A^{(2)}(t_{21})$, demonstrates that it is possible to simultaneously determine the effects of center-of-mass and anisotropy fluctuations. The Gaussian form of the mean center-of-mass displacement DF suggests that DsRed translational motion occurs by Fickian diffusion. For such systems, the translational components of the DFs and TCFs can be clearly identified and removed to isolate the components that depend on internal conformation. While the DF of the anisotropy fluctuations do not broaden on time scales greater than ~ 70 ms, the anisotropy TCF $C_A^{(2)}(t_{21})$ decays on the average

time scale of $\tau_A = 8$ s. The large disparity in relaxation time scales is consistent with a dynamically complex system composed of competing conformation processes that occur over a wide range of rates. A molecular level interpretation of these processes, and the role of heterogeneity in the DsRed system, is examined in more detail in our adjoining paper.

The information provided by the PM-FICS method should be useful to test fundamental models of protein dynamics. In the current work, the well-defined structure of the DsRed molecule and its favorable optical properties made this an appealing candidate to demonstrate the PM-FICS approach. Future extensions of the method should enable information-rich studies of the conformation dynamics of biological macromolecules of broad interest. The ability to perform such studies in solution and in cell compartments could facilitate future studies of *in vivo* enzymatic function.

CHAPTER V

KINETIC PATHWAYS OF SWITCHING OPTICAL CONFORMATIONS IN DSRED

BY 2D FOURIER IMAGING CORRELATION SPECTROSCOPY

In chapter IV, PM-FICS was demonstrated to be a useful tool for separating

internal conformation dynamics from translational dynamics in the naturally occurring

tetrameric energy transfer complex DsRed. In this chapter the PM-FICS technique will be

shown to be useful as a 2D electronic spectroscopy technique, with further experiments

on DsRed for the determination of distinct conformation transition pathways via

fluctuations in the degree of depolarization between separate spectral conformation

states. This chapter contains material co-authored with E.N. Senning, M.C. Fink, and

A.H. Marcus.

Background

A remarkable feature of proteins and nucleic acids is their unique ability to undergo

cooperative rearrangements in structure as part of mechanisms to regulate biological

activity. Rather than exist as a single, stable conformation, biological macromolecules

often exhibit a broad, heterogeneous distribution of sub-states in thermal equilibrium [1, 2].

Activation and inter-conversion between sub-states can span many decades over time [3].

Such systems exhibit complex spectra of relaxations, with principle time scales determined by transformations between sub-states, and exchange kinetics between different transition pathways [4].

The kinetics of conformational transitions and chemical exchange can be studied by two-dimensional (2D) NMR spectroscopy [4]. Transitions between conformations of biological macromolecules are reflected by the magnitudes of diagonal and off-diagonal peaks in 2D NMR spectra. In recent years, chemical exchange spectroscopy has been applied at infrared and visible frequencies [5]. 2D optical methods can investigate the inter-conversion between populations of chemical species that are spectroscopically non-equivalent. Such 2D optical experiments measure equilibrium chemical kinetics on the time scales of the excited state lifetimes of vibrational or electronic transitions.

In the current work, we show how polarization modulated Fourier imaging correlation spectroscopy (PM-FICS) can probe the pathways of optical switching conformations of the fluorescent protein complex, DsRed, over a broad range of time scales much longer than the excited state lifetime ($10^{-3} - 10^{2}$ s). The PM-FICS method, and its application to DsRed, is described in chapter IV. Similar to 2D optical and NMR methods, PM-FICS provides a phase-dependent optical signal that determines four-point time-correlation functions and the associated 2D spectra. Moreover, the information obtained from DsRed is sufficient to construct joint probability distributions of time-dependent conformational coordinates.

From a kinetic perspective, the DsRed protein is a dynamically complex heterogeneous system. Unlike monomeric variants of the green fluorescent protein

(GFP) [6], DsRed is an obligate tetramer of FP subunits [7]. FPs are single chains of ~ 230 amino acid residues, which form an 11-stranded β-barrel with dimensions ~ 3 nm × 4 nm. An α-helix inside the barrel contains the sequence of three residues that form the p-hydroxy-benzylidene-imidazolidinone chromophore. In DsRed, the π-π^* electron system of the chromophore is chemically and irreversibly extended to include an acylimine substituent, adjacent to the imidazolidinone [8, 9]. This so-called maturation process occurs over the course of several days and can be followed by a gradual gain in red photo-luminescence accompanied by a loss of green emission [8, 10]. Nevertheless, the maturation reaction does not run to completion, even after prolonged aging, so that a given DsRed molecule likely contains at least one 'immature' green chromophore [8, 11-13]. The red chromophore itself undergoes switching transitions, or 'flickering', between optical conformations of different emission wavelengths and intensities, and on time scales ranging between milliseconds and tens-of-seconds [14-17].

Although many studies have focused on the reversible, light induced pathways between 'bright' and 'dark' conformations [11, 14-17], thermally driven transitions between ground states are also possible [13, 16]. Detailed spectroscopic studies reveal that the red chromophore can reversibly interconvert, either through excited-state or ground-state pathways, between two brightly fluorescent red conformations (called 'red' and 'far-red'), and a relatively dim 'green' conformation [12, 13]. The energetic barriers mediating these transitions are on the order of ~ 1000 cm^{-1} (or 12 kJ mol^{-1} $\simeq$ 5 × $k_B T$ at ambient temperatures). Although the physical nature of the inter-conversion processes remains

unclear, possible mechanisms include isomerization of the protein-chromophore hydrogen-bonded network, cis-trans photo-isomerization, and ground state bond rotation [16, 18].

For our current purposes, we invoke a simplified model to interpret the conformational dynamics that influence excited state energy transfer between adjacent chromophores in the DsRed complex. Figure 5.1 depicts the DsRed molecule as four cylinders (arbitrarily labeled 1 – 4) with principle axes oriented approximately as in the crystal structure [7]. Crystallographic data suggest that there are three possible relationships between any pair of adjacent chromophores, given by the relative transition dipole orientations ($\theta^{24} = 41°$, $\theta^{23} = 47°$, and $\theta^{34} = 21°$) and the inter-dipole distances ($r^{24} = 43Å$, $r^{23} = 38Å$, and $r^{34} = 22Å$). By symmetry, the relationships between paired transition dipoles 2-4, 2-3, and 3-4 are the same as those between 1-3, 1-4, and 1-2, respectively [7].

As previously mentioned, most DsRed tetramers contain at least one immature green chromophore, which does not mature to red over the course of a PM-FICS measurement ($\sim$ 10 minutes). Of the sites that have matured to red (with absorption maximum $\lambda_{max} \sim$ 563 nm), these undergo reversible inter-conversion to the far-red conformation ($\lambda_{max} \sim$ 577 nm), or to the weakly fluorescent green conformation ($\lambda_{max} \sim$ 484 nm), on time scales of tens-of-milliseconds and longer. Figure 5.1 depicts a DsRed molecule with a single static (immature) green site at position 1 (shaded green), and three dynamically inter-converting red sites at positions 2 – 4. In the experiments presented

below, the red optical transitions ($\lambda_{ex} \sim 532$ nm) are selectively excited, and the integrated emission from both red and far-red states is detected. Both red and far-red
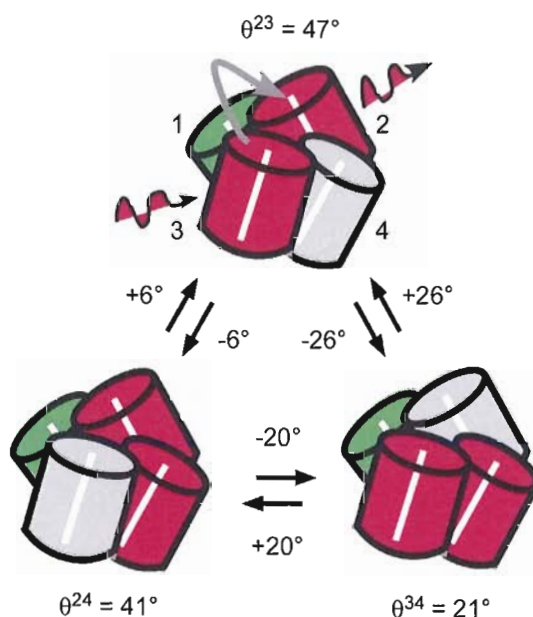
Figure 5.1: Optical conformational transitions of the 'mature' red chromophores in DsRed. DsRed is a tetrameric complex of cylindrically shaped fluorescent protein subunits, with relative orientations approximated in the figure. Each subunit has at its center an optical chromophore that can occupy one of two chemical states, corresponding to green or red emission. The green chromophores (shaded green) do not undergo chemical conversion to the red state on the time scales of our measurements. Red chromophores can inter-convert on millisecond time scales between two highly luminescent "bright" states (shaded red), and one "dark" state (shaded gray). From the crystallographic structure of DsRed, the relative angles θ^{ae} between adjacent absorption and emission transition dipole moments are known, and identified according to the numbering system shown on the top species. Polarization- and spectrally-selective excitation of the red chromophore subunits, mediated by electronic excitation transfer between coupled chromophores occupying adjacent sites, results in discrete transitions in the fluorescence depolarization angle $\Delta\theta^{ae}$.

conformations are considered bright states (shaded red in Fig. 5.1), while green states of the mature chromophore are dark (shaded gray). Thus, the immature green site at position 1 is pinned, while the red sites at positions 2 – 4 undergo reversible switching between bright and dark states. Because the distances and orientations between resonant optical transition dipoles are relatively small, an excited red chromophore can transfer its energy to one of its unexcited red or far-red neighbors by an energy transfer mechanism. When two sites in the DsRed complex are thus optically coupled, the emission polarization rotates by the angle θ^{ae}, which subtends the absorption dipole moment of the initially excited chromophore and the emission dipole moment of the emitting chromophore [14, 17]. Figure 5.1 illustrates the three possible pair-wise couplings between bright chromophore sites (for a molecule with one site pinned), and the associated depolarization angles. Also indicated are the six possible angular displacements $\Delta\theta^{ae}$ associated with conformational transitions between the three optically coupled states. Similar pair-wise couplings and transitions are possible for a molecule with all of its sites red (zero sites pinned). However, for a molecule with two or more of its sites pinned, transitions between distinct pair-wise coupled conformations are not possible, and such species are not expected to contribute to the fluctuating emission signals.

The model depicted in Fig. 5.1 is consistent with available experimental data for DsRed. However, little is known about the details of such thermally activated switching transitions, such as whether they occur at random or in a cooperative manner due to interactions between adjacent FP subunits. For example, a cooperative mechanism could involve a series of optical conformations, dynamically connected along multiple kinetic

pathways. The following work demonstrates how 2D PM-FICS can determine such information about the optical transitions of multi-colored FPs by monitoring the coordinate fluctuations of a finite population of molecules.

Experimental Methods

PM-FICS Observables: The equilibrium coordinate fluctuations of a finite population of DsRed molecules in 95% glycerol / water solution were monitored by the PM-FICS method, as described in chapter IV. The measurement observables are the number density $Z_{k_G}^{ND}(t) \propto \left\langle \exp i \left[k_G x(t) \right] \right\rangle$, and the anisotropy density $Z_{k_G}^{AD}(t)$ $\propto \left\langle \exp i \left[k_G x(t) - 2\theta^{ae}(t) \right] \right\rangle$, where the angle brackets indicate a sum over the $\sim 10^6$ molecules in the illuminated sample volume. In these expressions, $x(t)$ and $\theta^{ae}(t)$ are time-dependent position and conformation coordinates, respectively. We interpret these signals using the first order cumulant approximation (discussed in chapter IV).

Four-Point Time Correlation Functions: Four-point time correlation functions (TCF) for the number density and anisotropy density fluctuations were constructed from products of four sequential data points:

$$C_{ND}^{(4)}\left(t_{43}, t_{32}, t_{21}\right) \equiv \left\langle Z_{k_G}^{ND*}(0) Z_{k_G}^{ND}\left(t_{21}\right) Z_{k_G}^{ND}\left(t_{32} + t_{21}\right) Z_{k_G}^{ND*}\left(t_{43} + t_{32} + t_{21}\right) \right\rangle \qquad (5.1)$$

and

$$C_{AD}^{(4)}\left(t_{43},t_{32},t_{21}\right) \equiv \left\langle Z_{k_G}^{AD*}\left(0\right) Z_{k_G}^{AD}\left(t_{21}\right) Z_{k_G}^{AD}\left(t_{32}+t_{21}\right) Z_{k_G}^{AD*}\left(t_{43}+t_{32}+t_{21}\right)\right\rangle .$$

$$(5.2)$$

Equations (5.1) and (5.2) define the time intervals $t_{43}\left(=t_4-t_3\right)$, t_{32}, and t_{21} with $t_4 \geq t_3 \geq t_2 \geq t_1 \geq 0$. In the first-order cumulant approximation, Eqs. (5.1) and (5.2) can be written

$$C_{ND}^{(4)}\left(t_{43},t_{32},t_{21}\right) = \left\langle\exp\left[-\tfrac{1}{2}k_G^2\delta\Delta\bar{x}_N^2\left(t_{21}\right)\right]\right\rangle\left\langle\exp\left[-\tfrac{1}{2}k_G^2\delta\Delta\bar{x}_N^2\left(t_{43}\right)\right]\right\rangle$$
$$\times\left\langle\exp ik_G\left[\Delta\bar{x}_N\left(t_{43}\right)-\Delta\bar{x}_N\left(t_{21}\right)\right]\right\rangle$$

$$(5.3)$$

and

$$C_{AD}^{(4)}\left(t_{43},t_{32},t_{21}\right) = C_{ND}^{(4)}\left(t_{43},t_{32},t_{21}\right)C_A^{(4)}\left(t_{43},t_{32},t_{21}\right),$$

$$(5.4)$$

where

$$C_A^{(4)}\left(t_{43},t_{32},t_{21}\right) = \left\langle\exp\left[-2\delta\Delta\bar{\theta}_N^{ae2}\left(t_{21}\right)\right]\right\rangle\left\langle\exp\left[-2\delta\Delta\bar{\theta}_N^{ae2}\left(t_{43}\right)\right]\right\rangle$$
$$\times\left\langle\exp i2\left[\Delta\bar{\theta}_N^{ae}\left(t_{43}\right)-\Delta\bar{\theta}_N^{ae}\left(t_{21}\right)\right]\right\rangle .$$

$$(5.5)$$

Equation (5.3) defines the time-ordered displacements of the mean center-of-mass, $\Delta\bar{x}_N\left(t_{21}\right)\left[=\bar{x}_N\left(t_2\right)-\bar{x}_N\left(t_1\right)\right]$ and $\Delta\bar{x}_N\left(t_{43}\right)$, which occur during successive time intervals t_{21} and t_{43}, respectively. Similarly, Eq. (5.4) defines the time-ordered displacements of the mean depolarization angle, $\Delta\bar{\theta}_N^{ae}\left(t_{21}\right)$ and $\Delta\bar{\theta}_N^{ae}\left(t_{43}\right)$. Equation (5.4) suggests that the anisotropy   TCF   can   be   determined   from   the   ratio

$C_A^{(4)}\left(t_{43}, t_{32}, t_{21}\right) = C_{AD}^{(4)}\left(t_{43}, t_{32}, t_{21}\right) \big/ C_{ND}^{(4)}\left(t_{43}, t_{32}, t_{21}\right)$. These four-point TCFs have similar mathematical forms to those employed in two-dimensional optical and magnetic resonance spectroscopy [19]. Four-point TCFs contain information about correlations of events that occur during the intervals t_{43} and t_{21}, and decay on time scales for which the magnitudes of the collective phase displacements deviate by an amount $\sim \pi/4$. Such correlations diminish with increasing waiting period t_{32}, so that they appear indistinguishable from the products of functionally independent two-point TCFs. It is therefore useful to focus on the t_{32}-dependence of the difference correlation functions,

$$C^{(4)}\left(t_{43}, t_{32}, t_{21}\right) - C^{(2)}\left(t_{43}\right) C^{(2)}\left(t_{21}\right).$$

Two-Dimensional Spectral Densities: It is convenient to represent the four-point TCFs in the frequency domain, through their partial Fourier transform, with respect to t_{43} and t_{21}

$$S^{(4)}\left(v_{43}, t_{32}, v_{21}\right) = \int_0^\infty dt_{43} \int_0^\infty dt_{21} \left[C^{(4)}\left(t_{43}, t_{32}, t_{21}\right) - C^{(2)}\left(t_{43}\right) C^{(2)}\left(t_{21}\right) \right] e^{iv_{21}t_{21} + iv_{43}t_{43}}. \tag{5.6}$$

The 2D spectral density is given by the absolute value $\left| S^{(4)}\left(v_{43}, t_{32}, v_{21}\right) \right|$, plotted in the $v_{21} - v_{43}$ plane. The 2D spectral density is related to the joint probability that the system undergoes two successive coordinate displacements at the transition rates v_{21} and v_{43},

separated in time by the interval t_{32}. Such 2D spectra are similar to those obtained by magnetic resonance and optical techniques, and can provide information about the rates of chemical processes.

Two-Dimensional Distribution Functions: Information about weights and magnitudes of correlated displacements can be obtained from four-point distribution functions (DFs). We define $P^{(4)}\left[\Delta\bar{x}_N\left(t_{43}\right);\Delta\bar{x}_N\left(t_{21}\right)\right]$ as the joint probability density of sequentially sampling N molecules whose mean center-of-mass undergo two successive displacements, $\Delta\bar{x}_N\left(t_{21}\right)$ and $\Delta\bar{x}_N\left(t_{43}\right)$, during the intervals t_{21} and t_{43}, respectively. We construct the joint distributions by sampling four-point products of the form $Z_{k_G}^{ND*}\left(0\right)Z_{k_G}^{ND}\left(t_{21}\right)$

$$Z_{k_G}^{ND}\left(t_{32}+t_{21}\right)Z_{k_G}^{ND*}\left(t_{43}+t_{32}+t_{21}\right)=\exp\left[-\tfrac{1}{2}k_G^2\delta\Delta\bar{x}_N^2\left(t_{21}\right)\right]\exp\left[-\tfrac{1}{2}k_G^2\delta\Delta\bar{x}_N^2\left(t_{43}\right)\right]$$

$\times\exp ik_G\left[\Delta\bar{x}_N\left(t_{43}\right)-\Delta\bar{x}_N\left(t_{21}\right)\right]$. Such products are used to calculate 2D histograms of the joint probability to observe mean center-of-mass displacements during consecutive time intervals. As discussed in chapter IV, if the center-of-mass displacements are uncorrelated, then the joint distribution can be factored into a product of two-point DFs, i.e., $P^{(2)}\left[\Delta\bar{x}_N\left(t_{43}\right)\right]P^{(2)}\left[\Delta\bar{x}_N\left(t_{21}\right)\right]$. For such Brownian systems of diffusing molecules, the joint distribution is expected to be a two-dimensional Gaussian centered about the coordinate $\Delta\bar{x}_N\left(t_{43}\right)=\Delta\bar{x}_N\left(t_{21}\right)=0$.

2D distributions are similarly defined for displacements of the mean depolarization angle. $P^{(4)}\left[\Delta\bar{\theta}_N^{ae}(t_{43});\Delta\bar{\theta}_N^{ae}(t_{21})\right]$ is the joint distribution associated with consecutive displacements of conformation, which is constructed from four-point products of the anisotropy density $Z_{k_G}^{AD*}(0)Z_{k_G}^{AD}(t_{21})\ Z_{k_G}^{AD}(t_{32}+t_{21})Z_{k_G}^{AD*}(t_{43}+t_{32}+t_{21})\ =$

$$Z_{k_G}^{ND*}(0)Z_{k_G}^{ND}(t_{21})\ Z_{k_G}^{ND}(t_{32}+t_{21})\ Z_{k_G}^{ND*}(t_{43}+t_{32}+t_{21})$$

$Z^{A*}(0)Z^A(t_{21})\ Z^A(t_{32}+t_{21})\ Z^{A*}(t_{43}+t_{32}+t_{21})$. It is possible to divide the above expression by the contributions from the number density to isolate the anisotropy effects alone, i.e.,

$$Z^{A*}(0)Z^A(t_{21})\ Z^A(t_{32}+t_{21})Z^{A*}(t_{43}+t_{32}+t_{21}) = \exp\left[-2\delta\Delta\bar{\theta}_N^{ae2}(t_{21})\right]\exp\left[-2\delta\Delta\bar{\theta}_N^{ae2}(t_{43})\right]$$

$\times\exp i2\left[\Delta\bar{\theta}_N^{ae}(t_{43})-\Delta\bar{\theta}_N^{ae}(t_{21})\right]$. As we discuss below, such four-point DFs contain detailed information about correlated changes in the conformation of coupled dipoles of the DsRed complex.

Results and Discussion

In Fig. 5.2, we present results for the 2D spectral density and the joint DF of the mean center-of-mass displacements. In Fig. 5.2A is shown the logarithm of $\left|S_{ND}^{(4)}(\nu_{21},t_{32},\nu_{43})\right|$ in the $\nu_{21}-\nu_{43}$ plane, for t_{32} = 10 ms. Because the TCFs for DsRed translational motion decay exponentially, the Fourier transform-related spectral density (see Eq. (5.6)) is Lorentzian. For $t_{32}\le$ 20 ms, a minor feature is observed along the diagonal line $\nu_{21}=\nu_{43}$, indicating correlated motion on these relatively short time scales.

For $t_{32} > 20$ ms, the feature along the diagonal disappears (data not shown). In Fig. 5.2B is shown the joint distribution $P_N^{(4)}\left[\Delta \overline{x}_N (t_{21}); \Delta \overline{x}_N (t_{43})\right]$ evaluated at $t_{21} = t_{32} = t_{43} = 10$ ms. For all values of t_{32} investigated, the joint DF appears as a two-dimensional Gaussian consistent with Brownian motion. These results support the view that cooperative center-of-mass displacements do not play a significant role in DsRed dynamics on the time scales of the current measurements.

Having established an accurate picture of the center-of-mass dynamics for DsRed, it is possible to apply the factorization procedure outlined in the experimental methods section to determine the 2D spectrum of anisotropy fluctuations. In Fig. 5.3 is shown the logarithm of the two-dimensional spectral density $\left|S_A^{(4)}\left(\nu_{21}, t_{32}, \nu_{43}\right)\right|$ as a contour diagram in the $\nu_{21} - \nu_{43}$ plane, with $t_{32} = 20$ ms. Features that appear on the line diagonal to the spectrum ($\nu_{21} = \nu_{43}$) indicate sampled populations that maintain their rate of conformational transitions over the duration of the waiting period. Features that lie off the diagonal line, i.e. $\nu_{21} \neq \nu_{43}$, represent populations that undergo transitions between distinct regions of the spectrum during the waiting period. In Fig. 5.3, the magnitude of the spectrum evaluated at the diagonal line is projected onto the horizontal and vertical axes. The sampled populations are broadly distributed among transition rates ranging from $0 - 25$ Hz, and are roughly partitioned into two peaks centered at ~ 10 and 14 Hz. In Fig. 5.3, these peaks are labeled "slow" and "fast", and are indicated by vertical and horizontal dashed lines. At the intersections of the dashed lines are diagonal features associated with "slow" and "fast" populations. Off-diagonal features are labeled "slow-
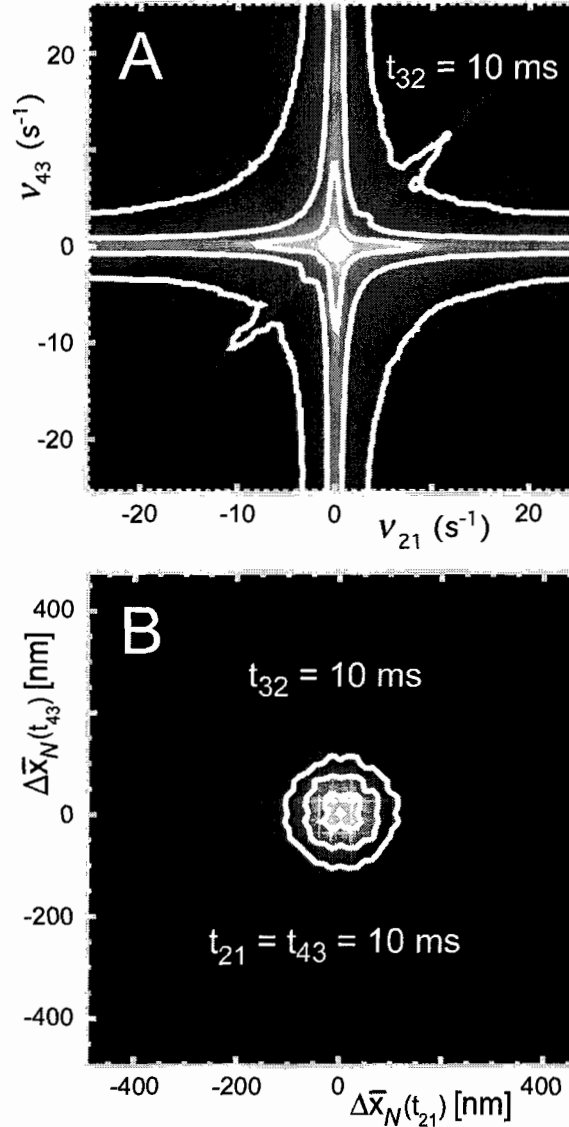
Figure 5.2: Contour diagrams of the two-dimensional spectral density, and the joint distribution function of center-of-mass displacements. In panel (A) is shown the logarithm of $\left|S_{ND}^{(4)}\left(\nu_{21}, t_{32}, \nu_{43}\right)\right|$ versus ν_{21} and ν_{43} for a single value of the waiting period $t_{32} = 10$ ms. The lineshape is nearly Lorentzian, centered at the peak value $\nu_{21} = \nu_{43} = 0$. In panel (B) is shown the joint distribution $P_N^{(4)}\left[\Delta\bar{x}_N\left(t_{21}\right), t_{32}, \Delta\bar{x}_N\left(t_{43}\right)\right]$ for the values $t_{21} = t_{32} = t_{43} = 10$ ms. The 2D distribution is approximately Gaussian, and centered about the origin with $\Delta\bar{x}_N\left(t_{21}\right) = \Delta\bar{x}_N\left(t_{43}\right) = 0$.
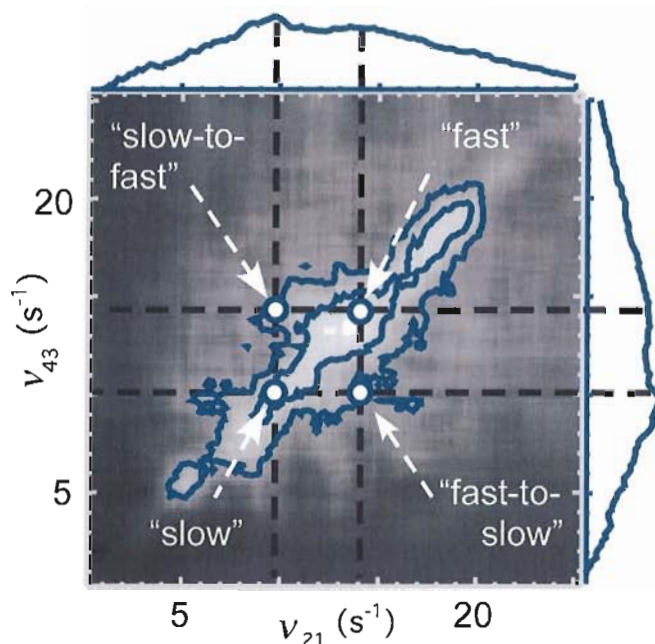
Figure 5.3: Logarithm of the two-dimensional spectral density of the mean depolarization angles $\left|S_A^{(4)}\left(v_{21}, t_{32}, v_{43}\right)\right|$, for waiting period $t_{32} = 20$ ms. Features along the diagonal line (labeled "fast" and "slow") indicate the distribution of conformational transition rates, while off-diagonal features indicate molecular populations that "exchange" between conformational transition rates. Along the horizontal and vertical axes is projected the magnitude of the spectrum, evaluated at the diagonal $v_{21} = v_{43}$. Contours are shown at 0.5 and 0.25 times the peak height.

to-fast" and "fast-to-slow," to indicate molecular sub-populations that make transitions between the two spectral regions. Because the 2D spectrum is narrow in the direction of the anti-diagonal ($v_{21} = -v_{43}$), the sampled populations do not readily exchange between fast and slow spectral regions on the time scale of ~ 20 ms.

We next determine joint DFs that contribute to the spectral line shape. In Figs. 5.4A – 5.4D are shown contour diagrams of $P^{(4)}\left[\Delta\bar{\theta}_N^{ae}\left(t_{43}\right); \Delta\bar{\theta}_N^{ae}\left(t_{21}\right)\right]$ corresponding to each of the four labeled points in the 2D spectrum shown in Fig. 5.3. Features in the joint DF can establish the existence of "pathways" between adjacent conformational

transitions. For each of the DFs shown in Fig. 5.4, the values of the intervals are $t_{32} = 20$ ms, and t_{21}, $t_{43} \in \{70 \text{ ms}, 100 \text{ ms}\}$, which were chosen to correspond to the labeled points in the spectral density. Along the horizontal and vertical axes are shown the projected magnitudes, which span the range $\pm 30°$. These DFs were constructed from histograms of $\sim 35,000$ four-point products. The procedure was repeated to insure reproducibility of independent data sets, and the results were averaged together to produce the DFs shown in Fig. 5.4.

For the two DFs representing diagonal features of the spectral density (labeled "fast" and "slow"), both exhibit mirror plane symmetry with respect to the diagonal line $[\Delta \bar{\theta}_N^{ae}(t_{21}) \simeq \Delta \bar{\theta}_N^{ae}(t_{43})]$. For the two DFs representing off-diagonal features (labeled "slow-to-fast" and "fast-to-slow"), each exhibits the projections of the "fast" and "slow" DFs onto one another. The joint DFs exhibit numerous peaks and shoulders, which undoubtedly reflect the conformational transitions of a complex heterogeneous system. In our current analysis, we focus on a subset of these peaks (indicated by vertical and horizontal dashed lines in Fig. 5.4). For the DF representing "slow" displacements (Fig. 5.4C), there are peaks centered at the coordinates $\left[\Delta \bar{\theta}_N^{ae}(t_{21}), \Delta \bar{\theta}_N^{ae}(t_{43}) \right] = \left(-6°, -6° \right)$, $\left(+2°, -6° \right)$ and $\left(-6°, +2° \right)$. For the distribution representing "fast" displacements (Fig. 5.4B), there are peaks at the coordinates $\left(+2°, +2° \right)$, $\left(+16°, +16° \right)$, $\left(+2°, +16° \right)$, $\left(+2°, -22° \right)$, $\left(+16°, +2° \right)$ and $\left(-22°, +2° \right)$. These peaks indicate correlated events, in which a change in molecular conformation of a given magnitude is temporally correlated

to that of another. The diagonal symmetry of the "fast" and "slow" DFs suggests that for the relatively short waiting period of $t_{32} = 20$ ms, there is no temporal bias to indicate which of the two correlated events precedes the other.
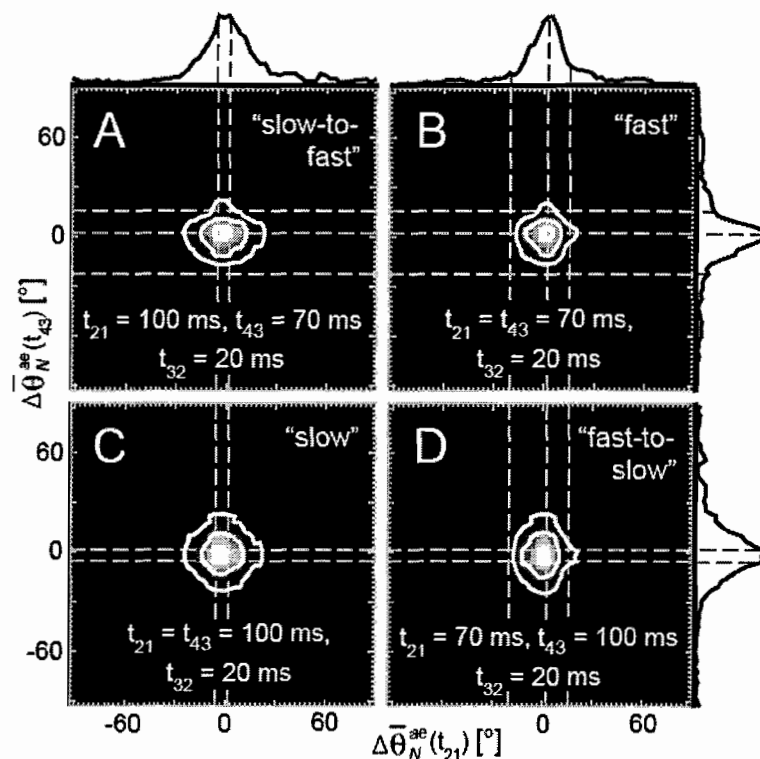
Figure 5.4: (A – D) Joint distributions of the sampled mean displacements of depolarization angles $P^{(4)}\left[\Delta\bar{\theta}_N^{ae}\left(t_{43}\right);\Delta\bar{\theta}_N^{ae}\left(t_{21}\right)\right]$, where the waiting period $t_{32} = 20$ ms, and t_{21}, $t_{43} \in \left\{70\,\text{ms},100\,\text{ms}\right\}$, as shown. Selected features in the joint distributions (indicated by horizontal and vertical dashed gray lines) reflect temporally correlated transitions that participate in "fast" (~ 70 ms) and "slow" (~ 100 ms) conformational transition pathways. The magnitudes of the distributions are projected onto horizontal and vertical axes. Contours are shown at 0.9, 0.5, and 0.25 times the peak height.

The above results suggest that there are two significant optical conformation pathways in DsRed; (i) a "slow" pathway connecting at least two sequential steps, which involve the angular displacements $\Delta\bar{\theta}_N^{ae} = +2°$ and $-6°$; and (ii) a "fast" pathway connecting at least three sequential steps, which involve the displacements $\Delta\bar{\theta}_N^{ae} = +2°$, $+16°$, and $-22°$. As discussed above, the coordinate pairings given by the joint DFs indicate the adjacencies between sequential steps in a given pathway. For example, the "fast" pathway appears to contain adjacent conformational transitions with $\Delta\bar{\theta}_N^{ae} = -22°$ and $+2°$, since the points $\left(+2°, \ -22°\right)$ and $\left(-22°, \ +2°\right)$ are present in the joint DF shown in Fig. 5.4B. On the other hand, the "fast" pathway does not contain adjacent transitions with $\Delta\bar{\theta}_N^{ae} = -22°$ and $+16°$, because the joint distribution has no significant magnitude at the points $\left(+16°, \ -22°\right)$ and $\left(-22°, \ +16°\right)$. The distributions representing off-diagonal features in the spectral density (Figs. 5.4A and 5.4D) contain information about exchange processes between the fast and slow pathways. For the distribution representing "slow-to-fast" exchange (Fig. 5.4A), features are present at the coordinates $\left(+2°, +2°\right)$, $\left(+2°, +16°\right)$, $\left(+2°, -22°\right)$, $\left(-6°, +2°\right)$, $\left(-6°, -22°\right)$ and $\left(-6°, +16°\right)$. For the distribution representing "fast-to-slow" exchange (Fig. 4D), features are present at the coordinates $\left(+2°, +2°\right)$, $\left(+2°, -6°\right)$, $\left(+16°, +2°\right)$, $\left(+16°, -6°\right)$, $\left(-22°, +2°\right)$ and $\left(-22°, -6°\right)$. Features present in the exchange distributions indicate bridging steps between "fast" and "slow" kinetic pathways.

Information about the time scale for exchange between "fast" and "slow" kinetic pathways is obtained from the t_{32}-dependence of the 2D spectrum. In Fig. 5.5A is shown the logarithm of $\left|S_A^{(4)}(v_{21}, t_{32}, v_{43})\right|$ for sequentially increasing values of the waiting period: t_{32} = 200 ms, 2 s, 5 s and 10 s. As the value of t_{32} is increased, the spectral density broadens in the transverse (off-diagonal) direction on the time scale of a few seconds. This transverse broadening indicates that sub-populations of molecules in the "fast" pathway undergo exchange with molecular populations in the "slow" pathway. The average time scale for the exchange is roughly the same as the τ_A = 8 s relaxation time for the anisotropy two-point TCF, reported in chapter IV. Nevertheless, the behavior of the joint DFs indicates that the elementary steps of the exchange processes occur on sub-second time scales. In Fig. 5.5B, are shown two sets of the joint distributions, corresponding to t_{32} = 2 s and 5 s. These DFs exhibit features at the same coordinates as those observed for the t_{32} = 20 ms DFs (indicated by dashed lines). As the waiting period is increased, there is a gradual loss of diagonal symmetry for "fast" and "slow" DFs (sub-panels B and C, respectively), such that they broaden in the direction of the vertical axis. As discussed further below, this loss of diagonal symmetry corresponds to the introduction of a temporal bias that indicates which of the two correlated transitions precedes the other. Furthermore, the loss of diagonal symmetry suggests a tendency for molecular population to flow from "fast" to the "slow" pathways during the waiting period.
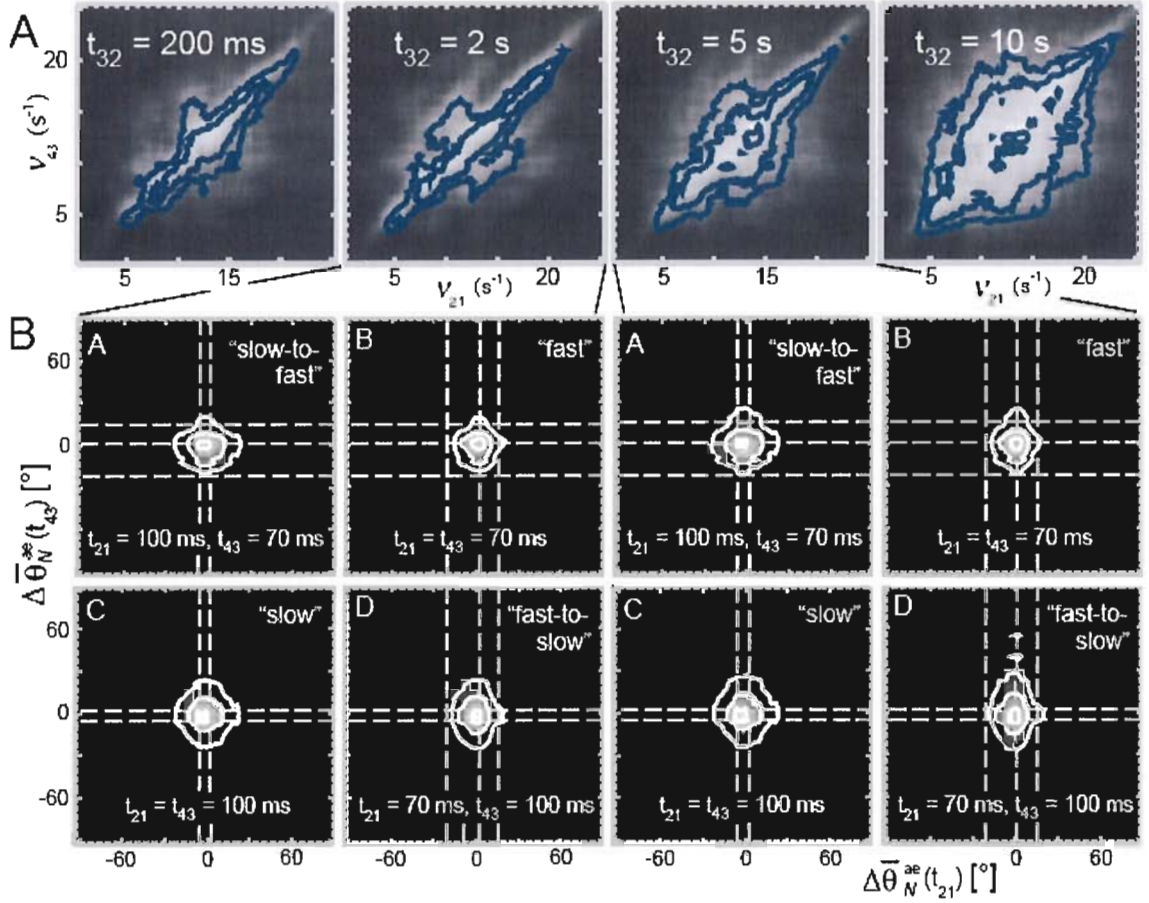
Figure 5.5: (A) Logarithm of the two-dimensional spectral density of the sampled mean depolarization angles $\left|S_A^{(4)}(v_{21},t_{32},v_{43})\right|$, for $t_{32} = 200$ ms, 2 s, 5 s, and 10s. The transverse broadening indicates that the average exchange time scale of the anisotropy fluctuations is approximately the same as the mean relaxation time $\tau_A = 8$ s. (B) Joint distributions $P^{(4)}\left[\Delta\bar{\theta}_N^{ae}(t_{43});\Delta\bar{\theta}_N^{ae}(t_{21})\right]$, with $t_{32} = 2$ s and 5 s.

Conclusions

Millisecond conformational dynamics of freely diffusing DsRed was studied using a four-point analysis of PM-FICS trajectories. The 2D spectrum of conformational transitions, $\left|S_A^{(4)}(v_{21},t_{32},v_{43})\right|$, is roughly partitioned into "fast" and "slow" kinetic

pathways. The slow anisotropy relaxation time τ_A = 8 s is characteristic of exchange

between "fast" and "slow" molecular sub-populations. Detailed information about the

pathways connecting adjacent conformational transitions is contained by the joint

distributions, $P^{(4)}\left[\Delta\bar{\theta}_N^{ae}(t_{43}); \Delta\bar{\theta}_N^{ae}(t_{21})\right]$. For waiting periods much shorter than the

exchange time $(t_{32} \ll \tau_A)$, there is a clear separation between molecular sub-populations

participating in each of the two pathways. For the "fast" sub-population, the angular

displacements $\Delta\bar{\theta}^{ae}$ = +2°, +16°, and −22° are observed, with adjacent pairings

+2° ↔ +16° and +2° ↔ −22°. For the "slow" sub-population, the paired

displacements $\Delta\bar{\theta}^{ae}$ = +2° and −6° are observed.

Our results can be combined with the model discussed in the background section

for the possible depolarization angles of DsRed optical conformations. We propose the

mechanism illustrated in Fig. 5.6 to partially account for our observations of the

conformational transition pathways. The system is assumed to be at equilibrium, with

average steady-state concentrations of species maintained by balanced differential rates

of inter-conversion. Based on the crystal structure of DsRed [7], three conformations are

possible for which the coupled dipoles have relative orientations θ_n^{ae} = 47°, 41°, and 21°

(see Fig. 5.1). Spectral shifts at individual chromophore sites result in conformational

transitions. The "fast" pathway, indicated by the blue arrow, consists of three temporally

correlated steps: −22° → +2° → +16°. The "slow" pathway, indicated by the gold

arrow, consists of two temporally correlated steps: +2° → −6°. For each step is

indicated the observed (in parentheses) and the expected angular displacements

accompanying the conversion between species. In both transition pathways, observations

of the angular displacement $\Delta\bar{\theta}^{ae} = +2°$ are assigned to conformational transitions in

which a red site is converted into a far-red site (purple). The similarities between optical

properties of the red and far-red states likely correspond to a very small change in the

transition dipole moment orientation. It is also hypothesized that intermediates lacking

dipolar coupling, such as the one generically depicted at the center of the diagram,

connects adjacent species. While there is a directional bias implied by the proposed

mechanism, the time ordering of events is interchangeable. A conformational transition
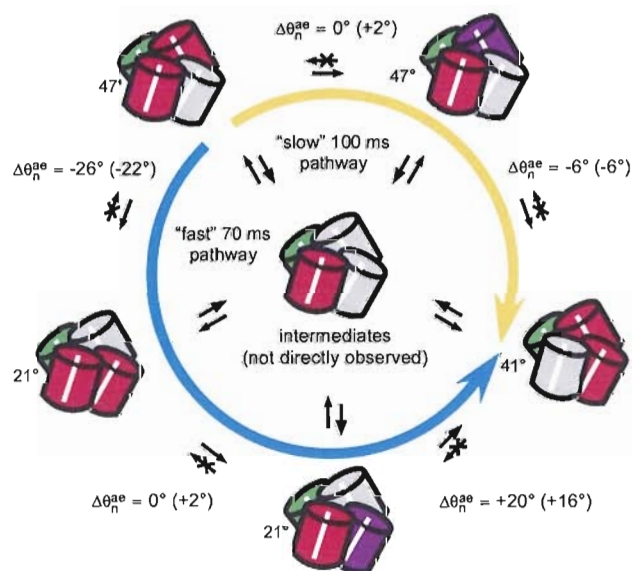
Figure 5.6: Possible model for the conformational transition pathways observed in DsRed. The structural and color conventions are the same as adopted in Fig. 1, except that the "far-red" chromophore state is indicated by purple shading. The measured displacements in the depolarization angle are shown in parentheses next to the expected values from the crystallographic data. The molecule undergoes temporally correlated (cooperative) transitions between different optically coupled conformations. There are distinct "fast" and "slow" transition pathways, operating on the 70 and 100 ms time scales, respectively (indicated by the blue and gold arrows). Intermediates lacking dipolar coupling, such as the one generically depicted at the center of the diagram, connects adjacent species. Exchange processes involve correlations between transitions that occur on separate pathways, and occur on the mean time scale of 8 s.

upstream in the pathway is correlated to an adjacent downstream transition. Nevertheless, for $t_{32} \ll \tau_A$, the time ordering of events is not established. That is, an upstream transition is as likely to occur before a downstream transition, as it is likely to occur after one. Features in the exchange distributions indicate correlations between transitions on separate pathways. Therefore, molecules participating in one reactive pathway can participate in the other pathway at a later time. For $t_{32} \ll \tau_A$, the exchange processes are symmetric; for each exchange process involving transfer of molecular population from the "fast" to the "slow" pathway, there is an equally weighted exchange process in the opposite direction.

As the waiting period is increased to values exceeding the mean relaxation time, the loss of diagonal symmetry of the "fast" and "slow" joint distributions $P^{(4)}\left[\Delta\bar{\theta}_N^{ae}(t_{43}); \Delta\bar{\theta}_N^{ae}(t_{21})\right]$ (see Fig. 5.5B) indicates the introduction of temporal bias. For $t_{32} \geq \tau_A$, downstream transitions tend to occur with greater probability after the waiting period. Corresponding inverse processes, in which downstream events occur prior to upstream events, receive less weight. Furthermore, the broadening of the exchange distributions occurs in an asymmetric manner. While the "fast-to-slow" distribution appears to elongate in the direction of the $\Delta\bar{\theta}_N^{ae}(t_{43})$ axis, the "slow-to-fast" distribution does so to a lesser extent. This indicates that exchange processes between "fast" and "slow" pathways are more heavily biased in the "fast-to-slow" direction.

In this work, we have demonstrated a new 2D optical approach to study the kinetics of equilibrium conformational transitions of biological macromolecules, over a wide range of time scales (10^{-3} – 10^2 s). Polarization-modulated Fourier imaging correlation spectroscopy (PM-FICS) was applied to simultaneously monitor molecular center-of-mass and anisotropy fluctuations. When applied to the system of DsRed molecules undergoing free diffusion, the approach allowed us to isolate the effects of optical switching conformational transitions. The phase-selectivity of PM-FICS measurements enables the calculation of 2D distributions and spectral densities. Similar to established 2D spectroscopic methods, the 2D spectral density determined by PM-FICS is useful to decompose the kinetics of a dynamically heterogeneous system, such as DsRed, into its separate components. A unique feature of PM-FICS is its ability to determine joint probability distributions of coordinate displacements, which contain detailed information about the pathways connecting sequential conformational transitions.

The PM-FICS method shares common attributes with 2D optical spectroscopy, single-molecule spectroscopy, and fluorescence fluctuation spectroscopy. The detailed information provided by PM-FICS measurements should be useful to address broad ranging problems in the fields of protein and nucleic acid dynamics, as well as other areas in complex systems. In the current work, the well-defined structure of the DsRed molecule made this an appealing candidate to demonstrate the potential of the approach. The ability to perform such measurements on proteins and nucleic acids of general

interest, in solution and in cell compartments, could enable future studies of *in vivo* enzymatic function.

CHAPTER VI

TWO-DIMENSIONAL ELECTRONIC COHERENCE SPECTROSCOPY OF SELF-

FORMING PORPHYRIN DIMERS IN LIPID BILAYER VESICLES

Two-dimensional spectroscopy is a useful tool for the study of coupling in

aggregated chromophore complexes. The information that these experiments yield can be

used to elucidate information about local structure of the fluorescent complexes,

timescales of coupling processes, coherence or incoherence of the coupling interactions,

and complex energy landscapes of multi-chromophore aggregates such as those occurring

in photosynthetic complexes,[1-8] conjugated polymers,[9] or semiconductors,[10] for example.

The simplest example of a coupled chromophore system is a homodimer, in which the

individual identical molecules can be modeled as simple two-level systems. When

coupled to each other, these two two-level molecules will form an exciton complex.[11,12]

This interaction splits the degenerate excited state levels into two excited state one-

exciton levels, in addition to creating a two-exciton state that is accessible using

nonlinear spectroscopy. In this chapter we will detail the extension of the formalism

introduced in chapter II to describe exciton coupled dimeric molecular systems, and

present data on self-forming porphyrin dimers in liposomal bilayer vesicles in solution at

room temperature.

It is helpful to mention that we are working in Liouville space and utilizing density operator formalism and superoperators in the theory presented here. The ensembles of molecules in these experiments are best represented as mixed states, and working in Liouville space with the density matrix also maintains the proper time-ordering of field-matter interactions, making it well-suited to describe nonlinear spectroscopy of condensed matter systems. The density matrix formalism in Liouville space, with superoperators and Liouville-space functions, has direct analogs to Hilbert space operators and functions, making its use a logical selection for these experiments.[13]

This chapter contains material co-authored with J. Utterback and A.H. Marcus.

Model Hamiltonian and Energy Levels of a Coupled
Two-Level System Homodimer

Let us consider a dimer of two-level systems. If we ignore the effects of the bath, the system Hamiltonian is

$$\underset{\sim}{H} = \underset{\sim}{H}_1 + \underset{\sim}{H}_2 + \underset{\sim}{V}_{12}, \tag{6.1}$$

where $\underset{\sim}{H}_1$ and $\underset{\sim}{H}_2$ are the monomer Hamiltonians for non-interacting chromophores and $\underset{\sim}{V}_{12}$ is the electronic coupling between the dimer chromphores. We assume a simple dipole-dipole interaction between the two chromophores, with the electronic coupling given by

$$V_{12} = \frac{\left(\underset{\sim}{\mu_1} \cdot \underset{\sim}{\mu_2}\right) - 3\left(\underset{\sim}{\mu_1} \cdot \hat{R}_{12}\right)\left(\underset{\sim}{\mu_2} \cdot \hat{R}_{12}\right)}{4\pi\varepsilon_o R_{12}{}^3}, \tag{6.2}$$

where R_{12} is the distance between the transition dipoles and $\hat{R}_{12}$ is the direction of the vector between the transition dipoles. For non-zero values of V_{12}, the coupled exciton states are delocalized over both of the individual chromophore sites with excited states specified by $|e_1\rangle$ and $|e_2\rangle$. These states are product states, which refer to one of the two chromophores excited while the other is in the ground state. The monomer transition dipole moment operators $\underset{\sim}{\mu_1}$ and $\underset{\sim}{\mu_2}$ are given by

$$\underset{\sim}{\mu_i} = \sum_{a,b} |a\rangle \mu_{i_{ab}} \langle b|. \tag{6.3}$$

For a homodimer we assume that the dipole magnitudes are equal and that their relative orientation is given by the dipole angle ϕ, as shown in Fig. 1.1A. We can define the total dipole operator as

$$\underset{\sim}{M} = \underset{\sim}{\mu_1} + \underset{\sim}{\mu_2}, \tag{6.4}$$

Linear combinations of these states that satisfy the orthogonality, normalization, and stationarity conditions are

$$|\pm\rangle = \frac{|e_1\rangle \pm |e_2\rangle}{\sqrt{2}}. \tag{6.5}$$

Eq. (6.5) defines the two one-exciton wavefunctions. Furthermore, we define the two-exciton state $|f\rangle$ for which both chromophores are simultaneously excited, and the ground state of the dimer $|g\rangle$ in which both chromophores are simultaneously in the ground state. The Hamiltonian in the site basis is

$$\underset{\sim}{H} = \begin{pmatrix} 0 & 0 & 0 & 0 \\ 0 & \omega_0 & V_{12} & 0 \\ 0 & V_{12} & \omega_0 & 0 \\ 0 & 0 & 0 & 2\omega_0 \end{pmatrix}, \tag{6.6}$$

where the effects of binding energy are ignored for the sake of simplicity.

Transition Dipoles and Frequencies to One- and Two-Exciton States

Using Eqs. (6.4) and (6.5), we find the transition dipole moments that couple the ground and one-exciton states are given by

$$\begin{aligned} \langle \pm | \underset{\sim}{M} | g \rangle &= \frac{1}{\sqrt{2}} \left(\langle e_1 | + \langle e_2 | \right) \left(\underset{\sim}{\mu_1} + \underset{\sim}{\mu_2} \right) | g \rangle \\ &= \frac{\mu_1 \pm \mu_2}{\sqrt{2}} \end{aligned} \tag{6.7}$$

Transitions from the $|\pm\rangle$ states to the two-exciton state $|f\rangle$ are determined by the

transition dipole moments

$$
\begin{aligned}
\langle f|\underset{\sim}{M}|\pm\rangle &= \frac{1}{\sqrt{2}}\langle f|\left(\underset{\sim}{\mu_1}+\underset{\sim}{\mu_2}\right)\left(|e_1\rangle\pm|e_2\rangle\right) \\
&= \frac{\mu_2\pm\mu_1}{\sqrt{2}}
\end{aligned}
\qquad (6.8)
$$

If we define $\underset{\sim}{\mu_\pm}=\dfrac{\underset{\sim}{\mu_1}\pm\underset{\sim}{\mu_2}}{\sqrt{2}}$, then the transition dipole moment operators for all four

relevant transitions are given by

$$
\begin{aligned}
|g\rangle &\rightarrow |+\rangle : \underset{\sim}{\mu_+} \\[4pt]
|g\rangle &\rightarrow |-\rangle : \underset{\sim}{\mu_-} \\[4pt]
|+\rangle &\rightarrow |f\rangle : \underset{\sim}{\mu_+} \\[4pt]
|-\rangle &\rightarrow |f\rangle : -\underset{\sim}{\mu_-}
\end{aligned}
\qquad (6.9)
$$

Having determined the relevant transition dipoles for a dimer, we next consider

the effect of the relative dipole angle ϕ. By simple trigonometry, if we take the transition

dipole μ_1 to be along the molecular-frame x-axis, the expressions for the two one-exciton

states can be defined in the molecular frame by

$$\begin{aligned}
\underset{\sim}{\mu}_{+} &= \mu\hat{x} + (\mu\cos\phi\hat{x} + \mu\sin\phi\hat{y}) \\
&= \mu(1+\cos\phi)\hat{x} + \mu\sin\phi\hat{y}
\end{aligned} \tag{6.10}$$

and

$$\begin{aligned}
\underset{\sim}{\mu}_{-} &= \mu\hat{x} - (\mu\cos\phi\hat{x} + \mu\sin\phi\hat{y}) \\
&= \mu(1-\cos\phi)\hat{x} - \mu\sin\phi\hat{y} \quad .
\end{aligned} \tag{6.11}$$

Determining which of the higher and lower energy states are the "+" and "-" states requires prior knowledge of the local structure, or experimental results that can be used to determine the aggregation type. Until we can label the states based on experimental data, we will refer to the lower energy one-exciton state as $|\varepsilon_1\rangle$ and the higher energy state as $|\varepsilon_2\rangle$.

J- and H-Aggregates

The relative amplitudes of features in a linear spectrum depend on the dipole strength, which is defined for $|+\rangle$ and $|-\rangle$ as

$$
\begin{aligned}
D_{\pm} = \left| \langle g | \underset{\sim}{M} | \pm \rangle \right|^2 &= \left| \frac{1}{\sqrt{2}} \langle g | \underset{\sim}{\mu_1} + \underset{\sim}{\mu_2} | \pm \rangle \right|^2 \\
&= \frac{1}{2} \left| \langle g | \underset{\sim}{\mu_1} | 1 \rangle \pm \langle g | \underset{\sim}{\mu_2} | 2 \rangle \right|^2 \\
&= \frac{1}{2} \left[\left| \langle g | \underset{\sim}{\mu_1} | 1 \rangle \right|^2 + \left| \langle g | \underset{\sim}{\mu_2} | 2 \rangle \right|^2 \pm 2 \left(\langle g | \underset{\sim}{\mu_1} | 1 \rangle \cdot \langle g | \underset{\sim}{\mu_2} | 2 \rangle \right) \right] \\
&= \frac{1}{2} \left[\left(\sqrt{D} \right)^2 + \left(\sqrt{D} \right)^2 \pm \left(\sqrt{D} \right)^2 \cos\phi \right] \\
&= D(1 \pm \cos\phi).
\end{aligned}
\tag{6.12}
$$

Equation (6.12) yields a simple result for the relative amplitudes of the two one-exciton features in a linear spectrum based on the relative geometry of the transition dipoles and the uncoupled dipole strength, D. This, in conjunction with Eq. (6.2) can be used to determine structural information for dimers with very narrow transitions, but difficulties arise in attempting to make definitive structural assignments from broadened spectra of molecules in complex environments.

To understand how $|+\rangle$ and $|-\rangle$ are assigned to specific spectral features, we need to understand the most fundamental aggregate configurations, pure J- and H-aggregates. We will examine these aggregates for a dimer. J-aggregates are often referred to as being in an end-to-end configuration, while H-aggregates are in a face-to-face configuration.[14] In Fig. 6.1, panels A and B, we depict a J-aggregate dimer with relative dipole angle of 0° and 180°, respectively. From Eq. (6.12), we see that for a dipole angle of 0°, the "+" state will have maximal dipole strength with a value of 2D and the "-" state will have a value of 0. The situation is reversed for a relative dipole angle of 180° - all of the dipole strength is then in the "-" state and the "+" state is dark. By determining the values of V_{12} (Eq. (6.2)) for these geometries, we can determine the magnitude of the spectral shift for
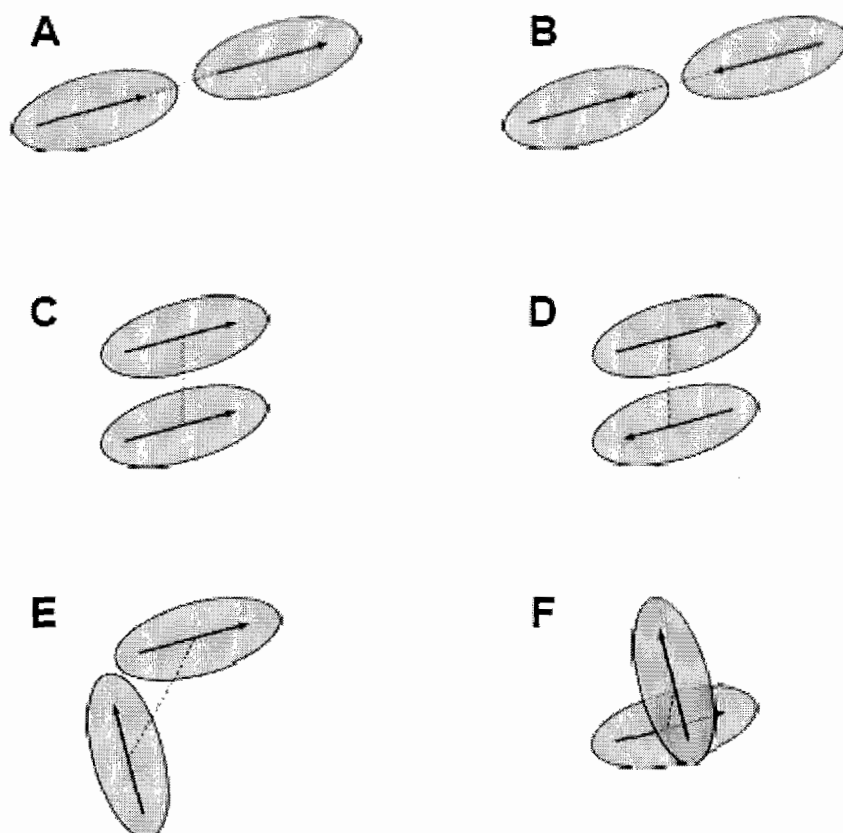
Figure 6.1: (A) and (B) depict J-aggregate dimers with unidirectional transition dipole moments and relative dipole angles of 0° and 180°, respectively. The interchromophore distance is shown as a dashed line, and continues to the middle of each of the transition dipole moments. (C) and (D) depict H-aggregate dimers with relative dipole angles of 0° and 180°, respectively. (E) depicts a coplanar end-to-end dimer with a 90° relative dipole angle. (F) depicts a face-to-face dimer with a relative dipole angle of 90°. The resulting potential V_{12} from each of these configurations is described in the text.

the dipole allowed transition and whether it appears as a red- or blue-shifted feature. The

transition frequencies of the transitions between ground and one-exciton states are

$\omega_{\pm} = \omega_0 \pm V_{12} / \hbar$. Additionally, the two exciton state has frequency, relative to the ground

state, of $\omega_{fg} = 2\omega_0 = \omega_{1g} + \omega_{2g}$, such that $\omega_{f1} \simeq \omega_{2g}$ and $\omega_{f2} \simeq \omega_{1g}$. For the relative dipole

angle of 0°, $V_{12} = -2\mu^2 / R_{12}^3 = -2D / R_{12}^3$, and for a dipole angle of 180°,

$V_{12} = 2\mu^2 / R_{12}^3 = 2D / R_{12}^3$. These results mean that the non-zero feature will be red-shifted with respect to the monomer center frequency – a pure J-aggregate will have a single red-shifted feature, where the magnitude of the shift depends on the distance between the transition dipole moments and the monomer dipole strength D.

Similarly, we consider a pure H-aggregate dimer in Fig. 6.1, panels C and D, with relative dipole angles 0° and 180°, respectively. Using similar arguments to those for the pure J-aggregates, we see that for relative dipole angles 0° and 180°, only the "+" and "-" states have finite intensity, respectively. The single feature for a pure H-aggregate is blue-shifted relative to the monomer center frequency, in contrast to the J-aggregate result. The values for the coupling strengths for the H-aggregate are

$V_{12} = \mu^2 / R_{12}^3 = D / R_{12}^3$ for 0° and $V_{12} = -\mu^2 / R_{12}^3 = -D / R_{12}^3$ for 180°.

Finally, let us examine an end-to-end dimer and an face-to-face dimer with relative dipole angles of 90°, as shown in Fig. 6.1, panels E and F. The face-to-face dimer, with all angles defined in Eq. (6.2) equal to 90°, will show no shift or splitting of energy levels and therefore the spectrum will be identical to that of the monomer. The J-aggregate will also have the two one-exciton states with equal amplitude, but they will be shifted by $V_{12} = -3D / 2R_{12}^3$ (a red-shift for the "+" state and a blue-shift for the "-" state).

From these examples, it is evident that an aggregate that is more 'J-like' than 'H-like' will have a larger red-shifted feature, while one that is more 'H-like' will have a larger blue-shifted feature. Using this information and knowledge of the relative distances of chromophores from one another, local structural information can be obtained from

experimental data. The congested linear spectra that these situations create will be limited in the useful information that they provide. 2D spectra will contain additional information that can be used to draw more definitive conclusions about coupling processes from molecular aggregates of unknown structure. The following sections will focus on how to utilize fluorescence detected 2D PM-ECS as an instrument for structural analysis of coupled molecular dimers.

Liouville Transition Pathways for Exciton Coupled Dimers

We have shown the homodimer to be a four level system with one ground state, two one-exciton states, and a single two-exciton state. We next determine the expressions for each of the quadrilinear overlaps, along with their respective pulse ladder diagrams. There are two types of contributions to the population signal for the four-level dimer. There are two distinct one-exciton terms which involve transitions between the ground and one-exciton states. There are also two-exciton contributions, which involve transitions between the one-exciton and the two exciton states, in addition to transitions between the ground and one-exciton states. There are no direct transitions between the ground and the two-exciton state, as it requires two separate excitation events to create excited electronic amplitude on both one-exciton states simultaneously.[11,12] In this section we will not account for the process of population transfer between the one-exciton states, but it will be addressed in a later section of this chapter. In addition to populations created by overlaps between a three-pulse wave packet and a one-pulse wave packet, there can be populations created by interferences between two two-pulse wavepackets,

$\langle\psi_{43}|\psi_{21}\rangle$, $\langle\psi_{42}|\psi_{31}\rangle$, and $\langle\psi_{41}|\psi_{32}\rangle$. The one-exciton contributions from these two

overlaps generate population on the ground state, not contributing to the collected

fluorescence signal. The total overlaps can then be expressed as, for example,

$\langle\psi_{432}|\psi_1\rangle = \langle\psi_{432}|\psi_1\rangle_{1ex} + \langle\psi_{432}|\psi_1\rangle_{2ex}$, where we have separated the one- and two-exciton

terms and labeled them with the "1*ex*" and "2*ex*" subtitles, respectively. Using the same

phase and free-evolution sign conventions defined in chapter II, we generate the overlap

terms,

$$
\begin{aligned}
\langle\psi_{432}|\psi_1\rangle &= \langle\psi_{432}|\psi_1\rangle_{1ex} + \langle\psi_{432}|\psi_1\rangle_{2ex} \\
&= \sum_{a,b}\left(\underset{\sim}{\mu}_{ag}\cdot\underset{\sim}{\alpha}_1(\omega_{ag})\right)\left(\underset{\sim}{\mu}_{bg}\cdot\underset{\sim}{\alpha}_2(\omega_{bg})\right) \\
&\quad\times\left(\underset{\sim}{\mu}_{bg}\cdot\underset{\sim}{\alpha}_3(\omega_{bg})\right)\left(\underset{\sim}{\mu}_{ag}\cdot\underset{\sim}{\alpha}_4(\omega_{ag})\right)e^{-i(\omega_{ag}t_{43}+\omega_{ag}t_{21}+(\omega_{ag}-\omega_{bg})t_{32})}e^{i(\phi_{43}+\phi_{21})} \\
&\quad+\sum_{a,b}\left(\underset{\sim}{\mu}_{ag}\cdot\underset{\sim}{\alpha}_1(\omega_{ag})\right)\left(\underset{\sim}{\mu}_{bg}\cdot\underset{\sim}{\alpha}_2(\omega_{bg})\right) \\
&\quad\times\left(\underset{\sim}{\mu}_{af}\cdot\underset{\sim}{\alpha}_3(\omega_{af})\right)\left(\underset{\sim}{\mu}_{bf}\cdot\underset{\sim}{\alpha}_4(\omega_{bf})\right)e^{-i(-\omega_{fa}t_{43}+\omega_{ag}t_{21}+(\omega_{ag}-\omega_{bg})t_{32})}e^{-i(\phi_{43}-\phi_{21})},
\end{aligned}
\tag{6.13}
$$

$$
\begin{aligned}
\langle\psi_{431}|\psi_2\rangle &= \langle\psi_{431}|\psi_2\rangle_{1ex} + \langle\psi_{431}|\psi_2\rangle_{2ex} \\
&= \sum_{a,b}\left(\underset{\sim}{\mu}_{ag}\cdot\underset{\sim}{\alpha}_1(\omega_{ag})\right)\left(\underset{\sim}{\mu}_{bg}\cdot\underset{\sim}{\alpha}_2(\omega_{bg})\right) \\
&\quad\times\left(\underset{\sim}{\mu}_{ag}\cdot\underset{\sim}{\alpha}_3(\omega_{ag})\right)\left(\underset{\sim}{\mu}_{bg}\cdot\underset{\sim}{\alpha}_4(\omega_{bg})\right)e^{-i(\omega_{bg}t_{43}-\omega_{ag}t_{21}+(\omega_{bg}-\omega_{ag})t_{32})}e^{i(\phi_{43}-\phi_{21})} \\
&\quad+\sum_{a,b}\left(\underset{\sim}{\mu}_{ag}\cdot\underset{\sim}{\alpha}_1(\omega_{ag})\right)\left(\underset{\sim}{\mu}_{bg}\cdot\underset{\sim}{\alpha}_2(\omega_{bg})\right) \\
&\quad\times\left(\underset{\sim}{\mu}_{af}\cdot\underset{\sim}{\alpha}_3(\omega_{af})\right)\left(\underset{\sim}{\mu}_{bf}\cdot\underset{\sim}{\alpha}_4(\omega_{bf})\right)e^{+i(\omega_{fb}t_{43}+\omega_{ag}t_{21}-(\omega_{ag}-\omega_{bg})t_{32})}e^{-i(\phi_{43}+\phi_{21})},
\end{aligned}
\tag{6.14}
$$

$$\begin{aligned}
\langle \psi_{421} | \psi_3 \rangle &= \langle \psi_{421} | \psi_3 \rangle_{1ex} + \langle \psi_{421} | \psi_3 \rangle_{2ex} \\
&= \sum_{a,b} \left(\underset{\sim}{\mu}_{ag} \cdot \underset{\sim}{\alpha}_1(\omega_{ag}) \right) \left(\underset{\sim}{\mu}_{ag} \cdot \underset{\sim}{\alpha}_2(\omega_{ag}) \right) \\
&\quad \times \left(\underset{\sim}{\mu}_{bg} \cdot \underset{\sim}{\alpha}_3(\omega_{bg}) \right) \left(\underset{\sim}{\mu}_{bg} \cdot \underset{\sim}{\alpha}_4(\omega_{bg}) \right) e^{-i(\omega_{bg}t_{43} - \omega_{ag}t_{21})} e^{i(\phi_{43} - \phi_{21})} \\
&\quad + \sum_{a,b} \left(\underset{\sim}{\mu}_{ag} \cdot \underset{\sim}{\alpha}_1(\omega_{ag}) \right) \left(\underset{\sim}{\mu}_{af} \cdot \underset{\sim}{\alpha}_2(\omega_{af}) \right) \\
&\quad \times \left(\underset{\sim}{\mu}_{bg} \cdot \underset{\sim}{\alpha}_3(\omega_{bg}) \right) \left(\underset{\sim}{\mu}_{bf} \cdot \underset{\sim}{\alpha}_4(\omega_{bf}) \right) e^{+i(\omega_{bf}t_{43} + \omega_{ag}t_{21} + \omega_{fg}t_{32})} e^{-i(\phi_4 + \phi_3 - \phi_2 - \phi_1)},
\end{aligned} \tag{6.15}$$

and

$$\begin{aligned}
\langle \psi_4 | \psi_{321} \rangle &= \langle \psi_4 | \psi_{321} \rangle_{1ex} + \langle \psi_4 | \psi_{321} \rangle_{2ex} \\
&= \sum_{a,b} \left(\underset{\sim}{\mu}_{ag} \cdot \underset{\sim}{\alpha}_1(\omega_{ag}) \right) \left(\underset{\sim}{\mu}_{ag} \cdot \underset{\sim}{\alpha}_2(\omega_{ag}) \right) \\
&\quad \times \left(\underset{\sim}{\mu}_{bg} \cdot \underset{\sim}{\alpha}_3(\omega_{bg}) \right) \left(\underset{\sim}{\mu}_{bg} \cdot \underset{\sim}{\alpha}_4(\omega_{bg}) \right) e^{-i(\omega_{bg}t_{43} + \omega_{ag}t_{21})} e^{i(\phi_{43} + \phi_{21})} \\
&\quad + \sum_{a,b} \left(\underset{\sim}{\mu}_{ag} \cdot \underset{\sim}{\alpha}_1(\omega_{ag}) \right) \left(\underset{\sim}{\mu}_{af} \cdot \underset{\sim}{\alpha}_2(\omega_{af}) \right) \\
&\quad \times \left(\underset{\sim}{\mu}_{bf} \cdot \underset{\sim}{\alpha}_3(\omega_{bf}) \right) \left(\underset{\sim}{\mu}_{bg} \cdot \underset{\sim}{\alpha}_4(\omega_{bg}) \right) e^{-i(\omega_{bg}t_{43} + \omega_{ag}t_{21} + \omega_{fg}t_{32})} e^{-i(\phi_4 + \phi_3 - \phi_2 - \phi_1)},
\end{aligned} \tag{6.16}$$

for the overlaps between three-pulse wave packets and one-pulse wave packets. We have taken into account the fact that the transition dipoles in these exciton systems will not, in general, all be parallel to each other and $a,b \in \{1,2\}$ for the two one-exciton states $|\varepsilon_1\rangle$ and $|\varepsilon_2\rangle$. In each of Eqs. (6.13) – (6.16) it is clear that the one-exciton terms have the same general forms as for a three-level system such as Rb, and will therefore have the same forms as in Eqs. (3.1) – (3.4), after downshifting by the reference signal frequency. The two-exciton terms behave quite differently than the one-exciton terms. The two-

exciton terms from the overlaps $\langle \psi_{421} | \psi_3 \rangle$ and $\langle \psi_4 | \psi_{321} \rangle$ do not have a sum or difference

phase relationship, and will therefore not be part of the collected sum or difference

signals. It is worth noting that even if they had a sum or difference phase signature, they

would be oscillating at a frequency ω_{fg}, which has a period of <1 fs. These terms would

therefore be averaged over experimentally unless pulses significantly shorter than 1 fs

were used. The two exciton contributions to the overlaps $\langle \psi_{432} | \psi_1 \rangle$ and $\langle \psi_{431} | \psi_2 \rangle$ have

difference and sum phases, respectively, imparted by the pulses. These are the *opposite*

phase relationships as the one-exciton contributions to the same overlaps, and the phases

are opposite in sign to the one-exciton sum and difference terms. Similarly, we generate

expressions for the two-pulse wave packet overlaps,

$$
\begin{aligned}
\langle \psi_{43} | \psi_{21} \rangle &= \langle \psi_{43} | \psi_{21} \rangle_{2ex} \\
&= \sum_{a,b} \left(\underset{\sim}{\mu}_{ag} \cdot \underset{\sim}{\alpha}_1 (\omega_{ag}) \right) \left(\underset{\sim}{\mu}_{af} \cdot \underset{\sim}{\alpha}_2 (\omega_{af}) \right) \\
&\quad \times \left(\underset{\sim}{\mu}_{bg} \cdot \underset{\sim}{\alpha}_3 (\omega_{bg}) \right) \left(\underset{\sim}{\mu}_{bf} \cdot \underset{\sim}{\alpha}_4 (\omega_{bf}) \right) e^{-i(-\omega_{fb} t_{43} + \omega_{ag} t_{21} + \omega_{fg} t_{32})} e^{-i(\phi_4 + \phi_3 - \phi_2 - \phi_1)},
\end{aligned}
\tag{6.17}
$$

$$
\begin{aligned}
\langle \psi_{42} | \psi_{31} \rangle &= \langle \psi_{42} | \psi_{31} \rangle_{2ex} \\
&= \sum_{a,b} \left(\underset{\sim}{\mu}_{ag} \cdot \underset{\sim}{\alpha}_1 (\omega_{ag}) \right) \left(\underset{\sim}{\mu}_{bg} \cdot \underset{\sim}{\alpha}_2 (\omega_{bg}) \right) \\
&\quad \times \left(\underset{\sim}{\mu}_{af} \cdot \underset{\sim}{\alpha}_3 (\omega_{af}) \right) \left(\underset{\sim}{\mu}_{bf} \cdot \underset{\sim}{\alpha}_4 (\omega_{bf}) \right) e^{+i(\omega_{fb} t_{43} + \omega_{ag} t_{21} - (\omega_{ag} - \omega_{bg}) t_{32})} e^{-i(\phi_{43} + \phi_{21})},
\end{aligned}
\tag{6.18}
$$

and

$$\langle \psi_{41}|\psi_{32}\rangle = \langle \psi_{41}|\psi_{32}\rangle_{2ex}$$

$$= \sum_{a,b} \left(\underset{\sim}{\mu}_{ag} \cdot \underset{\sim}{\alpha}_1(\omega_{ag}) \right)\left(\underset{\sim}{\mu}_{bg} \cdot \underset{\sim}{\alpha}_2(\omega_{bg}) \right) \tag{6.19}$$

$$\times \left(\underset{\sim}{\mu}_{bf} \cdot \underset{\sim}{\alpha}_3(\omega_{bf}) \right)\left(\underset{\sim}{\mu}_{af} \cdot \underset{\sim}{\alpha}_4(\omega_{af}) \right) e^{-i(\omega_{bf}t_{43}+\omega_{ag}t_{21}+(\omega_{bg}-\omega_{ag})t_{32})} e^{-i(\phi_{43}-\phi_{21})},$$

where we see, as for Eqs. (6.13) – (6.17), that the overlap $\langle \psi_{43}|\psi_{21}\rangle$ will not contribute to

the sum or difference signal, while $\langle \psi_{42}|\psi_{31}\rangle$ and $\langle \psi_{41}|\psi_{32}\rangle$ will contribute to the sum

and difference signals, respectively.

When multiplying the fluorescence signal by the reference signal in the lock-in

amplifiers, the complex conjugates of the two-exciton overlap terms in Eqs. (6.13) –

(6.16) will be those that enter into the collected complex signal. More explicitly, the

resulting sum and difference interference signals for a dimer system are

$$S_{sum}(t_{43},t_{32},t_{21};t') = 2\,\mathrm{Re}\left\{ \langle \psi_{432}|\psi_1\rangle_{1ex} + \langle \psi_4|\psi_{321}\rangle_{1ex} + \langle \psi_{431}|\psi_2\rangle_{2ex}^* - \langle \psi_{42}|\psi_{31}\rangle_{2ex} \right\} \tag{6.20}$$
$$\propto \cos(\phi_{43}+\phi_{21})$$

and

$$S_{dif}(t_{43},t_{32},t_{21};t') = 2\,\mathrm{Re}\left\{ \langle \psi_{431}|\psi_2\rangle_{1ex} + \langle \psi_{421}|\psi_2\rangle_{1ex} + \langle \psi_{432}|\psi_1\rangle_{2ex}^* - \langle \psi_{41}|\psi_{32}\rangle_{2ex} \right\} \tag{6.21}$$
$$\propto \cos(\phi_{43}-\phi_{21}),$$

respectively. The negative sign in Eqs. (6.20) and (6.21) is due to the number of pulse

interactions on the bra and ket sides of the overlaps, where the respective signs change as

$(-1)^{n+1}$, with n terms on the bra side of the overlap.[13,15] The first three terms in Eqs. (6.20) - (6.21) have identical numbers of interactions on each side of the overlap and therefore have identical signs, while the populations generated by the two-pulse overlaps will have the opposite sign. The latter two terms in Eqs. (6.20) – (6.21) are excited states absorption (ESA) contributions to the signal.

The pulse ladder diagrams that represent the one-exciton terms are exactly the same as those in Figs. 2.4 – 2.7, with the one-exciton energy levels ε_1 and ε_2 replacing the states labeled *I* and *II*. The two-exciton pathways for Eqs. (6.13) and (6.14) are shown in Figs. 6.2 and 6.3, respectively. The two-exciton pathways from the two-pulse overlaps defined in Eqs. (6.18) and (6.19) are shown in Figs. 6.4 and 6.5, respectively. The pulse ladder diagrams that represent the one-exciton terms are exactly the same as those in Figs. 2.4 – 2.7, with the one-exciton energy levels ε_1 and ε_2 replacing the states labeled *I* and *II*. The two-exciton pathways for Eqs. (6.13) and (6.14) are shown in Figs. 6.2 and 6.3, respectively.

Figure 6.2: Pulse ladder diagrams illustrating the four distinct two-exciton states for the overlap $\langle \psi_{432} | \psi_1 \rangle$ in the four-level dimer system. These are excited state absorption contributions, contributing with a sign identical to the one-exciton population signals.

Figure 6.3: Pulse ladder diagrams illustrating the four distinct two-exciton states for the overlap $\langle \psi_{431} | \psi_2 \rangle$ in the four-level dimer system. These are excited state absorption contributions, contributing with a sign identical to the one-exciton population signals.

Figure 6.4: Pulse ladder diagrams illustrating the four distinct two-exciton states for the overlap $\langle \psi_{42} | \psi_{31} \rangle$ in the four-level dimer system. These are excited state absorption contributions, contributing with a sign opposite to the one-exciton population signals.
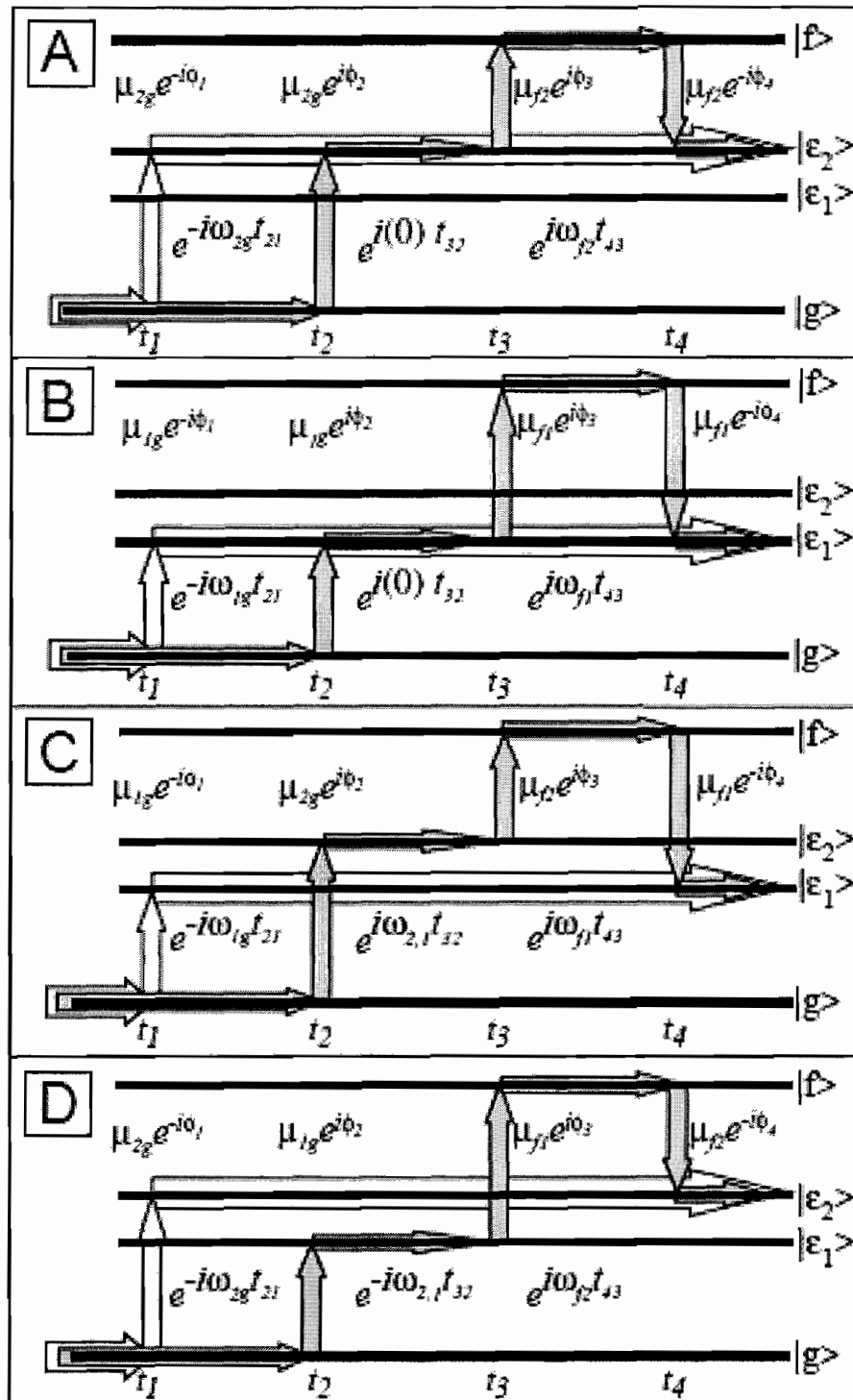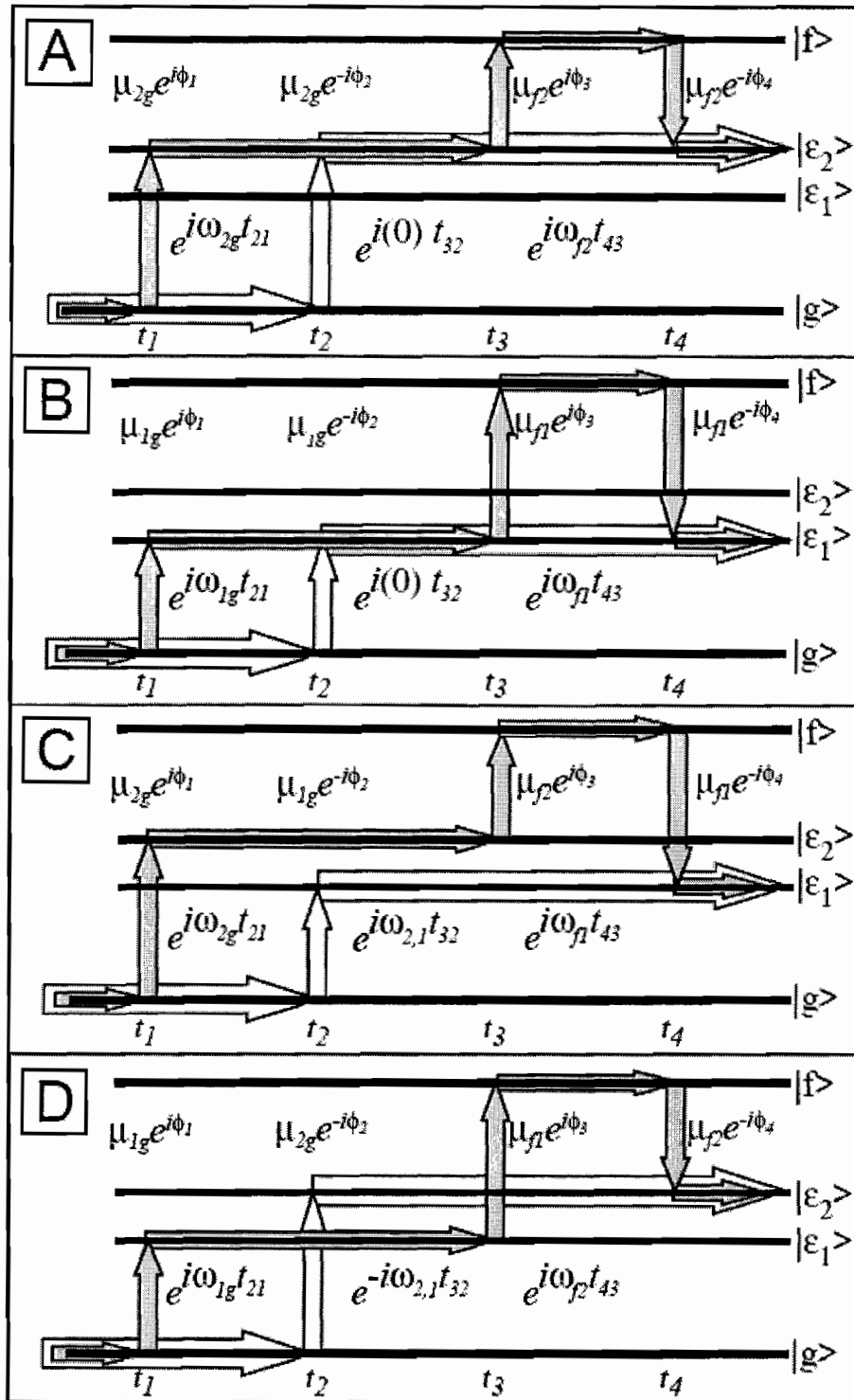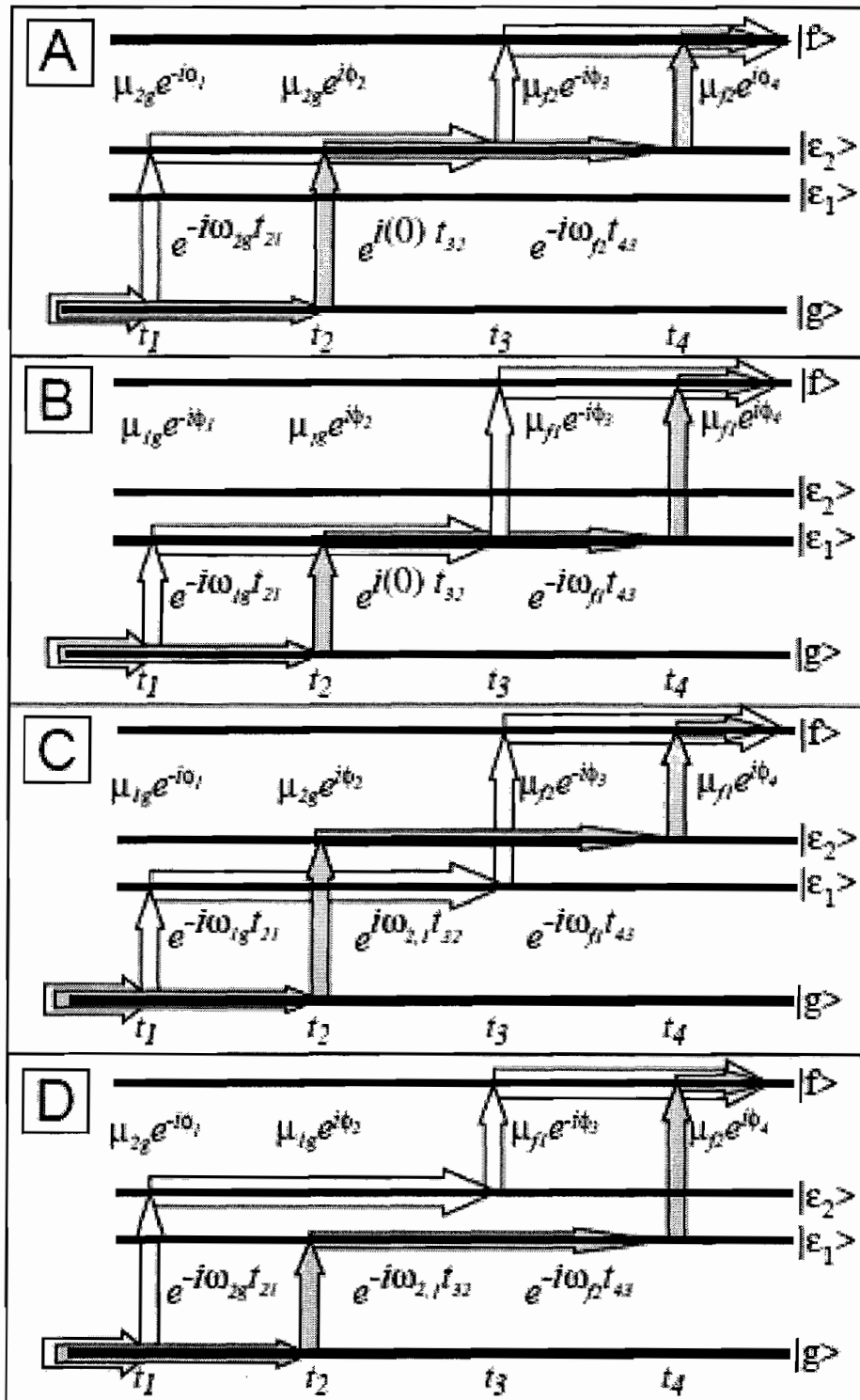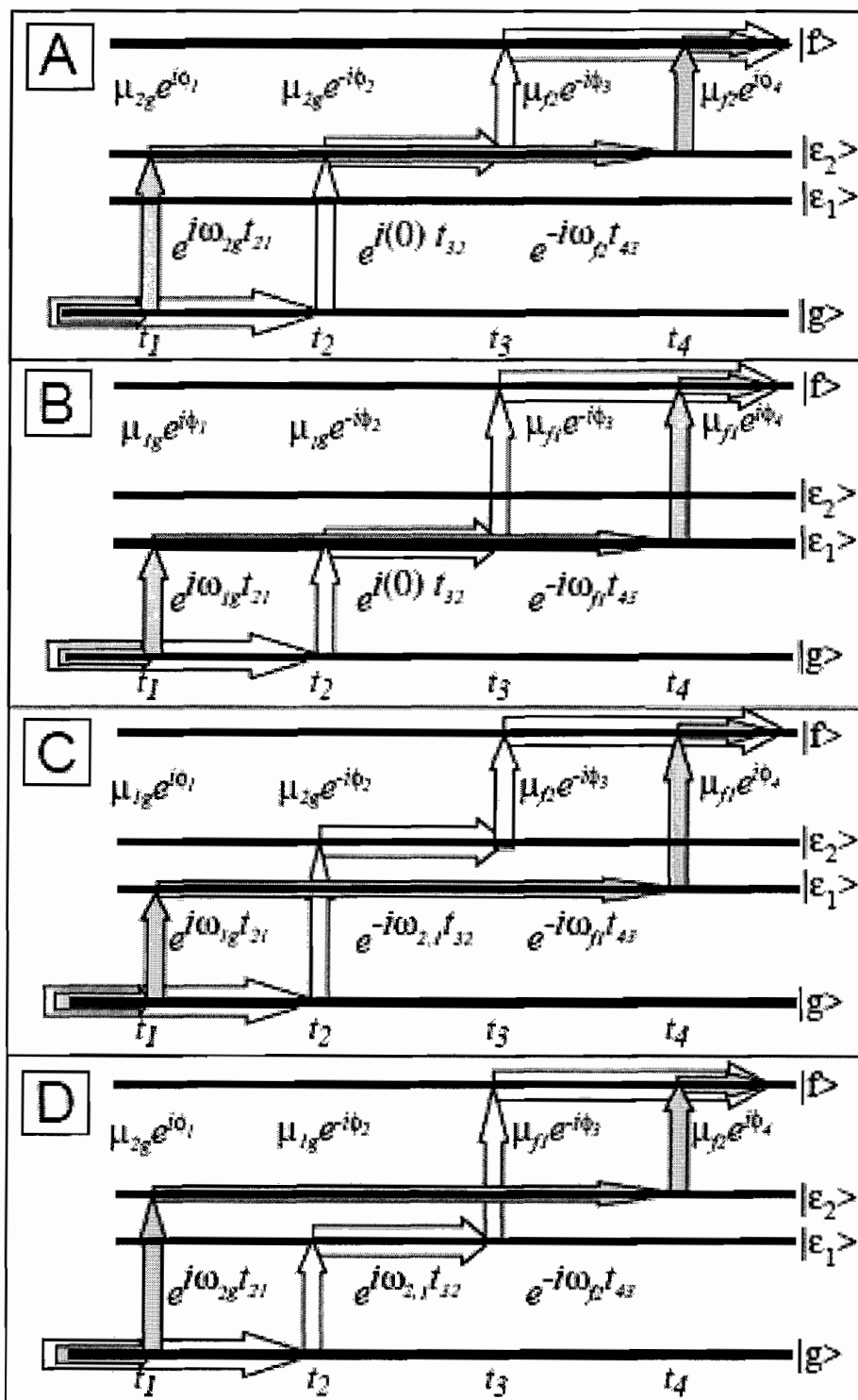
Figure 6.5: Pulse ladder diagrams illustrating the four distinct two-exciton states for the overlap $\langle \psi_{41} | \psi_{32} \rangle$ in the four-level dimer system. These are excited state absorption contributions, contributing with a sign opposite to the one-exciton population signals.

The Intermediate Time Regime

In the Rb experiments in chapter III, we saw oscillatory behavior of the four features in the 2D spectra due to the frequency difference between the two excited electronic energy levels. This coherent behavior was easily observable due to the long lived coherences of atomic Rb vapor. However, quantum beats like these relax very quickly in solution at room temperature due to thermal energy redistribution with the bath.[16-18] The dephasing of electronic coherences often occur within 100 fs at room temperature (ref: Cho, Fleming), resulting in the elimination of signal contributions from terms with explicit population time dependence. This is a good approximation for the system we have studied, and as we shall see, we do not observe oscillatory behavior in the 2D spectra as a function of T for the data presented in the latter part of this chapter.

Additionally, it is important to note that there are many non-radiative internal conversion processes from two-exciton states that result in the fluorescence quantum yield from the two-exciton state being very small relative to that of the one-exciton states. This allows us to make the approximation that the final term in Eqs. (6.20) and (6.21) does not contribute to the collected fluorescence signal. These approximations eliminate terms from both the sum and difference signals. Removing terms with explicit t_{32} dependence, and excluding terms resulting in population on the two-exciton state, the overlaps from Eqs. (6.13) – (6.19) become, in the intermediate time regime,

$$\langle \psi_{432} | \psi_1 \rangle = \sum_a \left(\underset{\sim}{\mu}_{ag} \cdot \underset{\sim}{\alpha}_1(\omega_{ag}) \right) \left(\underset{\sim}{\mu}_{ag} \cdot \underset{\sim}{\alpha}_2(\omega_{bg}) \right) \left(\underset{\sim}{\mu}_{ag} \cdot \underset{\sim}{\alpha}_3(\omega_{ag}) \right)$$

$$\times \left(\underset{\sim}{\mu}_{ag} \cdot \underset{\sim}{\alpha}_4(\omega_{bf}) \right) e^{-i(\omega_{ag}t_{43} + \omega_{ag}t_{21})} e^{i(\phi_{43} + \phi_{21})}$$

$$+ \sum_b \left(\underset{\sim}{\mu}_{bg} \cdot \underset{\sim}{\alpha}_1(\omega_{bg}) \right) \left(\underset{\sim}{\mu}_{bg} \cdot \underset{\sim}{\alpha}_2(\omega_{bg}) \right) \left(\underset{\sim}{\mu}_{bf} \cdot \underset{\sim}{\alpha}_3(\omega_{ag}) \right)$$

$$\times \left(\underset{\sim}{\mu}_{bf} \cdot \underset{\sim}{\alpha}_4(\omega_{bf}) \right) e^{-i(-\omega_{fb}t_{43} + \omega_{bg}t_{21})} e^{-i(\phi_{43} - \phi_{21})}, \tag{6.22}$$

.

$$\langle \psi_{431} | \psi_2 \rangle = \sum_a \left(\underset{\sim}{\mu}_{ag} \cdot \underset{\sim}{\alpha}_1(\omega_{ag}) \right) \left(\underset{\sim}{\mu}_{ag} \cdot \underset{\sim}{\alpha}_2(\omega_{ag}) \right) \left(\underset{\sim}{\mu}_{ag} \cdot \underset{\sim}{\alpha}_3(\omega_{ag}) \right)$$

$$\times \left(\underset{\sim}{\mu}_{ag} \cdot \underset{\sim}{\alpha}_4(\omega_{ag}) \right) e^{-i(\omega_{ag}t_{43} - \omega_{ag}t_{21})} e^{i(\phi_{43} - \phi_{21})}$$

$$+ \sum_b \left(\underset{\sim}{\mu}_{bg} \cdot \underset{\sim}{\alpha}_1(\omega_{bg}) \right) \left(\underset{\sim}{\mu}_{bg} \cdot \underset{\sim}{\alpha}_2(\omega_{bg}) \right) \left(\underset{\sim}{\mu}_{bf} \cdot \underset{\sim}{\alpha}_3(\omega_{bf}) \right)$$

$$\times \left(\underset{\sim}{\mu}_{bf} \cdot \underset{\sim}{\alpha}_4(\omega_{bf}) \right) e^{+i(\omega_{fb}t_{43} + \omega_{bg}t_{21})} e^{-i(\phi_{43} + \phi_{21})}, \tag{6.23}$$

$$\langle \psi_{421} | \psi_3 \rangle = \sum_{a,b} \left(\underset{\sim}{\mu}_{ag} \cdot \underset{\sim}{\alpha}_1(\omega_{ag}) \right) \left(\underset{\sim}{\mu}_{ag} \cdot \underset{\sim}{\alpha}_2(\omega_{ag}) \right) \left(\underset{\sim}{\mu}_{bg} \cdot \underset{\sim}{\alpha}_3(\omega_{bg}) \right)$$

$$\times \left(\underset{\sim}{\mu}_{bg} \cdot \underset{\sim}{\alpha}_4(\omega_{bg}) \right) e^{-i(\omega_{bg}t_{43} - \omega_{ag}t_{21})} e^{i(\phi_{43} - \phi_{21})} \tag{6.24}$$

and

$$\langle \psi_4 | \psi_{321} \rangle = \sum_{a,b} \left(\underset{\sim}{\mu}_{ag} \cdot \underset{\sim}{\alpha}_1(\omega_{ag}) \right) \left(\underset{\sim}{\mu}_{ag} \cdot \underset{\sim}{\alpha}_2(\omega_{ag}) \right) \left(\underset{\sim}{\mu}_{bg} \cdot \underset{\sim}{\alpha}_3(\omega_{bg}) \right)$$

$$\times \left(\underset{\sim}{\mu}_{bg} \cdot \underset{\sim}{\alpha}_4(\omega_{bg}) \right) e^{-i(\omega_{bg}t_{43} + \omega_{ag}t_{21})} e^{i(\phi_{43} + \phi_{21})}. \tag{6.25}$$

By removing the t_{32} dependent terms, all sum and difference terms vary with respect to the coherence and detection times only. Since the transition frequencies from the one-exciton to the two-exciton states can be expressed in terms of transition frequencies from the ground to the one exciton states ($\omega_{f2} = \omega_{1g}$ and $\omega_{f1} = \omega_{2g}$), we can use Eq. (6.9) to express the transition dipole moments between the one-and two-exciton states similarly. These substitutions modify Eqs. (6.22) – (6.25) to

$$
\begin{aligned}
\langle \psi_{432} | \psi_1 \rangle = \sum_a &\left(\underset{\sim}{\mu}_{ag} \cdot \underset{\sim}{\alpha}_1(\omega_{ag}) \right)\left(\underset{\sim}{\mu}_{ag} \cdot \underset{\sim}{\alpha}_2(\omega_{ag}) \right)\left(\underset{\sim}{\mu}_{ag} \cdot \underset{\sim}{\alpha}_3(\omega_{ag}) \right) \\
&\times \left(\underset{\sim}{\mu}_{ag} \cdot \underset{\sim}{\alpha}_4(\omega_{ag}) \right) e^{-i(\omega_{ag}t_{43}+\omega_{ag}t_{21})} e^{i(\phi_{43}+\phi_{21})} \\
+ \sum_{b \neq a} &\left(\underset{\sim}{\mu}_{bg} \cdot \underset{\sim}{\alpha}_1(\omega_{bg}) \right)\left(\underset{\sim}{\mu}_{bg} \cdot \underset{\sim}{\alpha}_2(\omega_{bg}) \right)\left(\underset{\sim}{\mu}_{bg} \cdot \underset{\sim}{\alpha}_3(\omega_{bg}) \right) \\
&\times \left(\underset{\sim}{\mu}_{bg} \cdot \underset{\sim}{\alpha}_4(\omega_{bg}) \right) e^{-i(-\omega_{ag}t_{43}+\omega_{bg}t_{21})} e^{-i(\phi_{43}-\phi_{21})},
\end{aligned}
\tag{6.26}
$$

$$
\begin{aligned}
\langle \psi_{431} | \psi_2 \rangle = \sum_a &\left(\underset{\sim}{\mu}_{ag} \cdot \underset{\sim}{\alpha}_1(\omega_{ag}) \right)\left(\underset{\sim}{\mu}_{ag} \cdot \underset{\sim}{\alpha}_2(\omega_{ag}) \right)\left(\underset{\sim}{\mu}_{ag} \cdot \underset{\sim}{\alpha}_3(\omega_{ag}) \right) \\
&\times \left(\underset{\sim}{\mu}_{ag} \cdot \underset{\sim}{\alpha}_4(\omega_{ag}) \right) e^{-i(\omega_{ag}t_{43}-\omega_{ag}t_{21})} e^{i(\phi_{43}-\phi_{21})} \\
+ \sum_{b \neq a} &\left(\underset{\sim}{\mu}_{bg} \cdot \underset{\sim}{\alpha}_1(\omega_{bg}) \right)\left(\underset{\sim}{\mu}_{bg} \cdot \underset{\sim}{\alpha}_2(\omega_{bg}) \right)\left(\underset{\sim}{\mu}_{bg} \cdot \underset{\sim}{\alpha}_3(\omega_{bg}) \right) \\
&\times \left(\underset{\sim}{\mu}_{bg} \cdot \underset{\sim}{\alpha}_4(\omega_{bg}) \right) e^{+i(\omega_{ag}t_{43}+\omega_{bg}t_{21})} e^{-i(\phi_{43}+\phi_{21})},
\end{aligned}
\tag{6.27}
$$

$$
\begin{aligned}
\langle \psi_{421} | \psi_3 \rangle = \sum_{a,b} &\left(\underset{\sim}{\mu}_{ag} \cdot \underset{\sim}{\alpha}_1(\omega_{ag}) \right)\left(\underset{\sim}{\mu}_{ag} \cdot \underset{\sim}{\alpha}_2(\omega_{ag}) \right)\left(\underset{\sim}{\mu}_{bg} \cdot \underset{\sim}{\alpha}_3(\omega_{ag}) \right) \\
&\times \left(\underset{\sim}{\mu}_{bg} \cdot \underset{\sim}{\alpha}_4(\omega_{ag}) \right) e^{-i(\omega_{bg}t_{43}-\omega_{ag}t_{21})} e^{i(\phi_{43}-\phi_{21})}
\end{aligned}
\tag{6.28}
$$

and

$$\langle \psi_4 | \psi_{321} \rangle = \sum_{a,b} \left(\underset{\sim}{\mu}_{ag} \cdot \underset{\sim}{\alpha}_1(\omega_{ag}) \right) \left(\underset{\sim}{\mu}_{ag} \cdot \underset{\sim}{\alpha}_2(\omega_{ag}) \right) \left(\underset{\sim}{\mu}_{bg} \cdot \underset{\sim}{\alpha}_3(\omega_{bg}) \right)$$
$$\times \left(\underset{\sim}{\mu}_{bg} \cdot \underset{\sim}{\alpha}_4(\omega_{bg}) \right) e^{-i(\omega_{bg}t_{43}+\omega_{ag}t_{21})} e^{i(\phi_{43}+\phi_{21})}. \tag{6.29}$$

We can now separate the terms into groups, independent of population time, that contribute to the four features in the 2D spectra – the two diagonal peaks from the single-mode contributions of the one-exciton states and the two off-diagonal peaks that yield information about the coupling between the one-exciton states. The diagonal features are centered at the points $(\omega_{1g}, \omega_{1g})$ and $(\omega_{2g}, \omega_{2g})$, where the frequencies ω_{1g} and ω_{2g} are the frequencies to access the one-exciton states $|\varepsilon_1\rangle$ and $|\varepsilon_2\rangle$, respectively. The two off-diagonal features are centered at $(\omega_{1g}, \omega_{2g})$ and $(\omega_{2g}, \omega_{1g})$. The off-diagonal features are often referred to as "uphill" and "downhill" coupling features, respectively. We label the terms in the time domain that contribute to specific spectral features, in the same order as described above, Z_{11}, Z_{22}, Z_{12}, and Z_{21} for both the sum and difference signals. Taking into account the reference signals, $e^{i(\bar{\omega}_{43}t_{43}\pm\bar{\omega}_{21}t_{21})}$, we construct the complex valued functions for the sum signal

$$Z_{11}^{sum}(t_{43}, t_{32}, t_{21}) = 2 \left(\underset{\sim}{\mu}_{1g} \cdot \underset{\sim}{\alpha}_1(\omega_{1g}) \right) \left(\underset{\sim}{\mu}_{1g} \cdot \underset{\sim}{\alpha}_2(\omega_{1g}) \right) \left(\underset{\sim}{\mu}_{1g} \cdot \underset{\sim}{\alpha}_3(\omega_{1g}) \right)$$
$$\times \left(\underset{\sim}{\mu}_{1g} \cdot \underset{\sim}{\alpha}_4(\omega_{1g}) \right) e^{-i((\omega_{1g}-\bar{\omega}_{43})t_{43}+(\omega_{1g}-\bar{\omega}_{43})t_{21})}, \tag{6.30}$$

$$Z_{22}^{sum}(t_{43},t_{32},t_{21}) = 2\left(\underset{\sim}{\mu}_{2g}\cdot\underset{\sim}{\alpha}_1(\omega_{2g})\right)\left(\underset{\sim}{\mu}_{2g}\cdot\underset{\sim}{\alpha}_2(\omega_{2g})\right)\left(\underset{\sim}{\mu}_{2g}\cdot\underset{\sim}{\alpha}_3(\omega_{2g})\right)$$
$$\times\left(\underset{\sim}{\mu}_{2g}\cdot\underset{\sim}{\alpha}_4(\omega_{2g})\right)e^{-i((\omega_{2g}-\bar{\omega}_{43})t_{43}+(\omega_{2g}-\bar{\omega}_{43})t_{21})}, \tag{6.31}$$

$$Z_{12}^{sum}(t_{43},t_{32},t_{21}) = \left(\underset{\sim}{\mu}_{1g}\cdot\underset{\sim}{\alpha}_1(\omega_{1g})\right)\left(\underset{\sim}{\mu}_{1g}\cdot\underset{\sim}{\alpha}_2(\omega_{1g})\right)\left(\underset{\sim}{\mu}_{2g}\cdot\underset{\sim}{\alpha}_3(\omega_{2g})\right)$$
$$\times\left(\underset{\sim}{\mu}_{2g}\cdot\underset{\sim}{\alpha}_4(\omega_{2g})\right)e^{-i((\omega_{2g}-\bar{\omega}_{43})t_{43}+(\omega_{1g}-\bar{\omega}_{43})t_{21})}$$
$$+\left(\underset{\sim}{\mu}_{1g}\cdot\underset{\sim}{\alpha}_1(\omega_{1g})\right)\left(\underset{\sim}{\mu}_{1g}\cdot\underset{\sim}{\alpha}_2(\omega_{1g})\right)\left(\underset{\sim}{\mu}_{1g}\cdot\underset{\sim}{\alpha}_3(\omega_{1g})\right)$$
$$\times\left(\underset{\sim}{\mu}_{1g}\cdot\underset{\sim}{\alpha}_4(\omega_{1g})\right)e^{-i((\omega_{2g}-\bar{\omega}_{43})t_{43}+(\omega_{1g}-\bar{\omega}_{43})t_{21})}, \tag{6.32}$$

and

$$Z_{21}^{sum}(t_{43},t_{32},t_{21}) = \left(\underset{\sim}{\mu}_{2g}\cdot\underset{\sim}{\alpha}_1(\omega_{2g})\right)\left(\underset{\sim}{\mu}_{2g}\cdot\underset{\sim}{\alpha}_2(\omega_{2g})\right)\left(\underset{\sim}{\mu}_{1g}\cdot\underset{\sim}{\alpha}_3(\omega_{1g})\right)$$
$$\times\left(\underset{\sim}{\mu}_{1g}\cdot\underset{\sim}{\alpha}_4(\omega_{1g})\right)e^{-i((\omega_{1g}-\bar{\omega}_{43})t_{43}+(\omega_{2g}-\bar{\omega}_{43})t_{21})}$$
$$+\left(\underset{\sim}{\mu}_{2g}\cdot\underset{\sim}{\alpha}_1(\omega_{2g})\right)\left(\underset{\sim}{\mu}_{2g}\cdot\underset{\sim}{\alpha}_2(\omega_{2g})\right)\left(\underset{\sim}{\mu}_{2g}\cdot\underset{\sim}{\alpha}_3(\omega_{2g})\right)$$
$$\times\left(\underset{\sim}{\mu}_{2g}\cdot\underset{\sim}{\alpha}_4(\omega_{2g})\right)e^{-i((\omega_{1g}-\bar{\omega}_{43})t_{43}+(\omega_{2g}-\bar{\omega}_{43})t_{21})}, \tag{6.33}$$

and equivalently for the difference signal,

$$Z_{11}^{dif}(t_{43},t_{32},t_{21}) = 2\left(\underset{\sim}{\mu}_{1g}\cdot\underset{\sim}{\alpha}_1(\omega_{1g})\right)\left(\underset{\sim}{\mu}_{1g}\cdot\underset{\sim}{\alpha}_2(\omega_{1g})\right)\left(\underset{\sim}{\mu}_{1g}\cdot\underset{\sim}{\alpha}_3(\omega_{1g})\right)$$
$$\times\left(\underset{\sim}{\mu}_{1g}\cdot\underset{\sim}{\alpha}_4(\omega_{1g})\right)e^{-i((\omega_{1g}-\bar{\omega}_{43})t_{43}-(\omega_{1g}-\bar{\omega}_{43})t_{21})}, \tag{6.34}$$

$$Z_{22}^{dif}(t_{43},t_{32},t_{21}) = 2\left(\underset{\sim}{\mu}_{2g}\cdot\underset{\sim}{\alpha}_1(\omega_{2g})\right)\left(\underset{\sim}{\mu}_{2g}\cdot\underset{\sim}{\alpha}_2(\omega_{2g})\right)\left(\underset{\sim}{\mu}_{2g}\cdot\underset{\sim}{\alpha}_3(\omega_{2g})\right)$$
$$\times\left(\underset{\sim}{\mu}_{2g}\cdot\underset{\sim}{\alpha}_4(\omega_{2g})\right)e^{-i((\omega_{2g}-\bar{\omega}_{43})t_{43}-(\omega_{2g}-\bar{\omega}_{43})t_{21})}, \tag{6.35}$$

$$Z_{12}^{dif}(t_{43}, t_{32}, t_{21}) = \left(\underset{\sim}{\mu}_{1g} \cdot \underset{\sim}{\alpha}_1(\omega_{1g}) \right)\left(\underset{\sim}{\mu}_{1g} \cdot \underset{\sim}{\alpha}_2(\omega_{1g}) \right)\left(\underset{\sim}{\mu}_{2g} \cdot \underset{\sim}{\alpha}_3(\omega_{2g}) \right)$$
$$\times \left(\underset{\sim}{\mu}_{2g} \cdot \underset{\sim}{\alpha}_4(\omega_{2g}) \right) e^{-i((\omega_{2g} - \bar{\omega}_{43})t_{43} - (\omega_{1g} - \bar{\omega}_{43})t_{21})}$$
$$+ \left(\underset{\sim}{\mu}_{1g} \cdot \underset{\sim}{\alpha}_1(\omega_{1g}) \right)\left(\underset{\sim}{\mu}_{1g} \cdot \underset{\sim}{\alpha}_2(\omega_{1g}) \right)\left(\underset{\sim}{\mu}_{1g} \cdot \underset{\sim}{\alpha}_3(\omega_{1g}) \right)$$
$$\times \left(\underset{\sim}{\mu}_{1g} \cdot \underset{\sim}{\alpha}_4(\omega_{1g}) \right) e^{-i((\omega_{2g} - \bar{\omega}_{43})t_{43} - (\omega_{1g} - \bar{\omega}_{43})t_{21})}, \tag{6.36}$$

and

$$Z_{21}^{dif}(t_{43}, t_{32}, t_{21}) = \left(\underset{\sim}{\mu}_{2g} \cdot \underset{\sim}{\alpha}_1(\omega_{2g}) \right)\left(\underset{\sim}{\mu}_{2g} \cdot \underset{\sim}{\alpha}_2(\omega_{2g}) \right)\left(\underset{\sim}{\mu}_{1g} \cdot \underset{\sim}{\alpha}_3(\omega_{1g}) \right)$$
$$\times \left(\underset{\sim}{\mu}_{1g} \cdot \underset{\sim}{\alpha}_4(\omega_{1g}) \right) e^{-i((\omega_{1g} - \bar{\omega}_{43})t_{43} - (\omega_{2g} - \bar{\omega}_{43})t_{21})}$$
$$+ \left(\underset{\sim}{\mu}_{2g} \cdot \underset{\sim}{\alpha}_1(\omega_{2g}) \right)\left(\underset{\sim}{\mu}_{2g} \cdot \underset{\sim}{\alpha}_2(\omega_{2g}) \right)\left(\underset{\sim}{\mu}_{2g} \cdot \underset{\sim}{\alpha}_3(\omega_{2g}) \right)$$
$$\times \left(\underset{\sim}{\mu}_{2g} \cdot \underset{\sim}{\alpha}_4(\omega_{2g}) \right) e^{-i((\omega_{1g} - \bar{\omega}_{43})t_{43} - (\omega_{2g} - \bar{\omega}_{43})t_{21})}. \tag{6.37}$$

These complex valued functions are analogous to those for rubidium in Eqs. (3.1) - (3.4), but here we have separated them into signals that contribute to specific features in the non-rephasing (sum) and rephasing (difference) spectra. The total time-dependent signal functions are $Z^{sum/dif} = Z_{11}^{sum/dif} + Z_{22}^{sum/dif} + Z_{12}^{sum/dif} + Z_{21}^{sum/dif}$.

Rotational Averaging of Fourth-Rank Tensors

Molecular aggregate systems will usually have locally fixed relative transition dipole orientations. It is important to consider the fact that while the transition dipoles are fixed relative to each other, each aggregate from an ensemble in a disordered, isotropic environment will be randomly oriented with respect to the four specifically polarized

laser pulses. We can account for this through rotational averaging of the relevant fourth-rank tensors.[17] We were not forced to account for this in the rubidium experiments because both of the experimentally accessed transition dipole moments in rubidium were parallel to one another.

Generally, if the nth rank tensor $t^{(n)}$ in the molecular-fixed frame is known, the averaged n^{th} rank tensor $T^{(n)}$ in the laboratory frame is

$$\widehat{T}^{(n)}_{l_1 l_2 l_3 \ldots l_n} = I^{(n)}_{l_1 l_2 l_3 \ldots l_n : m_1 m_2 m_3 \ldots m_n} \, t^{(n)}_{m_1 m_2 m_3 \ldots m_n} \qquad (6.38)$$

where we have defined the Cartesian axes in the molecular and laboratory frames as m_k and l_k, respectively, and the well known n^{th} rank rotationally invariant tensor is $I^{(n)}$. The fourth rank rotationally invariant tensor is[19]

$$I^{(4)} = \frac{1}{30} \begin{pmatrix} \delta_{l_1 l_2} \delta_{l_3 l_4} & \delta_{l_1 l_3} \delta_{l_2 l_4} & \delta_{l_1 l_4} \delta_{l_2 l_3} \end{pmatrix} \begin{pmatrix} 4 & -1 & -1 \\ -1 & 4 & -1 \\ -1 & -1 & 4 \end{pmatrix} \begin{pmatrix} \delta_{m_1 m_2} \delta_{m_3 m_4} \\ \delta_{m_1 m_3} \delta_{m_2 m_4} \\ \delta_{m_1 m_4} \delta_{m_2 m_3} \end{pmatrix}, \qquad (6.39)$$

where δ_{ij} are Kroneker delta functions. Expanded, Eq. (6.39) becomes

$$I^{(4)} = \frac{1}{30} \left\{ \delta_{l_1 l_2} \delta_{l_3 l_4} \left[4\delta_{m_1 m_2} \delta_{m_3 m_4} - \delta_{m_1 m_2} \delta_{m_3 m_4} - \delta_{m_1 m_2} \delta_{m_3 m_4} \right] \right. $$
$$ + \delta_{l_1 l_3} \delta_{l_2 l_4} \left[-\delta_{m_1 m_2} \delta_{m_3 m_4} + 4\delta_{m_1 m_2} \delta_{m_3 m_4} - \delta_{m_1 m_2} \delta_{m_3 m_4} \right] \qquad (6.40)$$
$$ \left. + \delta_{l_1 l_4} \delta_{l_2 l_3} \left[-\delta_{m_1 m_2} \delta_{m_3 m_4} - \delta_{m_1 m_2} \delta_{m_3 m_4} + 4\delta_{m_1 m_2} \delta_{m_3 m_4} \right] \right\}.$$

For a sequence of four parallel polarized laser pulses, the products of Kronecker delta functions $\delta_{l_i l_j} \delta_{l_p l_q}$ will all be equal to one, reducing Eq. (6.40) to

$$I^{(4)} = \frac{1}{15} \left\{ \delta_{m_1 m_2} \delta_{m_3 m_4} + \delta_{m_1 m_2} \delta_{m_3 m_4} + \delta_{m_1 m_2} \delta_{m_3 m_4} \right\}. \qquad (6.41)$$

Inserting Eq. (6.41) into Eq. (6.38) for four parallel polarized pulses (in the X direction for Cartesian axes X, Y, and Z in the laboratory frame) yields the expression

$$\hat{T}_{XXXX}^{(4)} = \frac{1}{15} \sum_{m_1 m_2 m_3 m_4} \left(\delta_{m_1 m_2} \delta_{m_3 m_4} t_{m_1 m_2 m_3 m_4}^{(4)} + \delta_{m_1 m_3} \delta_{m_2 m_4} t_{m_1 m_3 m_2 m_4}^{(4)} + \delta_{m_1 m_4} \delta_{m_2 m_3} t_{m_1 m_4 m_2 m_3}^{(4)} \right)$$
$$= \frac{1}{15} \sum_{1234} \left(\delta_{12} \delta_{34} t_{1234}^{(4)} + \delta_{13} \delta_{24} t_{1324}^{(4)} + \delta_{14} \delta_{23} t_{1423}^{(4)} \right), \qquad (6.42)$$

where we have dropped the m indices on the second line for simplicity. This can be reduced to, for molecular-frame axes of x, y, and z,

$$\hat{T}^{(4)}_{XXXX} = \frac{1}{15}\left[3\left(t^{(4)}_{xxxx} + t^{(4)}_{yyyy} + t^{(4)}_{zzzz}\right) + \sum_{i\neq j\in\{x,y,z\}}\left(t^{(4)}_{iijj} + t^{(4)}_{ijij} + t^{(4)}_{ijji}\right)\right].$$

$$(6.43)$$

Eq. (6.43) contains all possible non-zero elements from Eq. (6.42).

We assume that as well as being parallel, all electric fields have equal amplitude and are spectrally broad. This effectively removes the electric field dependence from the results, and means that we are rotationally averaging over the tensor elements $\mu_1\mu_2\mu_3\mu_4$ from the molecular frame, where the indices 1, 2, 3, and 4 denote the four separate transition events and possibly distinct dipole moments. From Eq. (6.43) we see that the time ordering of the dipoles does not matter – a term like $t^{(4)}_{iijj}$, for example, is a product of the scalar components of the transition dipole vectors, such that the ordering of the individual components does not affect the product. More explicitly, if we have a sequence of four transitions with the same transition dipole moment, the ordering of the i and j indices will not affect the final rotationally averaged result as long as the number of individual i and j indices are preserved.

From Eqs. (6.30) – (6.37), we can determine the various population terms that must be orientationally averaged. Let us first look at the one-exciton GSB and SE contributions, which can be expressed as $\langle\mu_+^2\mu_+^2\rangle_{XXXX}$, $\langle\mu_-^2\mu_-^2\rangle_{XXXX}$, $\langle\mu_+^2\mu_-^2\rangle_{XXXX}$, and $\langle\mu_-^2\mu_+^2\rangle_{XXXX}$. From Eqs. (6.30) – (6.37) we see that the four relative peak heights, for both rephasing and non-rephasing signals, are proportional to

$$S_{++} \propto 2 \left\langle \mu_+^2 \mu_+^2 \right\rangle_{XXXX} \tag{6.44}$$

$$S_{--} \propto 2 \left\langle \mu_-^2 \mu_-^2 \right\rangle_{XXXX} \tag{6.45}$$

$$S_{+-} \propto \left\langle \mu_+^2 \mu_-^2 \right\rangle_{XXXX} + \left\langle \mu_-^2 \mu_+^2 \right\rangle_{XXXX} \tag{6.46}$$

$$S_{-+} \propto \left\langle \mu_+^2 \mu_-^2 \right\rangle_{XXXX} + \left\langle \mu_-^2 \mu_-^2 \right\rangle_{XXXX} \tag{6.47}$$

Again, we have not yet assigned the "+" and "-" states since these designations depend on *a priori* structural information or inferences based on experimental results, but it is clear that these are the only four possible combinations of transitions. The brackets around these transition dipole products reflect the orientational averaging process that we have defined in Eq. (6.43). We immediately see that the latter two terms are equal to each other, as changing the ordering of the indices in Eq. (6.43) does not change the final orientationally averaged result, as we argued above. Using Eq. (6.43), we solve for $\left\langle \mu_+^2 \mu_+^2 \right\rangle_{XXXX}$:

$$\left\langle \mu_+^2 \mu_+^2 \right\rangle_{XXXX} = \frac{\mu^4}{15} \Big[3 \left(\mu_{+_x} \mu_{+_x} \mu_{+_x} \mu_{+_x} \right) + 3 \left(\mu_{+_y} \mu_{+_y} \mu_{+_y} \mu_{+_y} \right) + 6 \left(\mu_{+_x} \mu_{+_x} \mu_{+_y} \mu_{+_y} \right) \Big]. \tag{6.48}$$

Substituting the components of μ_+ from Eq. (6.10), we find

$$\left\langle \mu_+^2 \mu_+^2 \right\rangle_{XXXX} = \frac{3|\mu|^4}{15} \Big[(1+\cos\phi)^4 + (\sin\phi)^4$$
$$+ 2(1+\cos\phi)^2 (\sin\phi)^2 \Big] \quad (6.49)$$
$$= \frac{12|\mu|^4}{15} (1+\cos\phi)^2 .$$

This is exactly the answer we should intuitively expect – it has an angle dependence that is the square of the "+" feature angle dependence in the linear spectrum. Similarly, we use Eq. (6.11) to find

$$\left\langle \mu_-^2 \mu_-^2 \right\rangle_{XXXX} = \frac{3|\mu|^4}{15} \Big[(1-\cos\phi)^4 + (\sin\phi)^4$$
$$+ 2(1-\cos\phi)^2 (\sin\phi)^2 \Big] \quad (6.50)$$
$$= \frac{12|\mu|^4}{15} (1-\cos\phi)^2 .$$

Since $\left\langle \mu_+^2 \mu_-^2 \right\rangle_{XXXX} = \left\langle \mu_-^2 \mu_+^2 \right\rangle_{XXXX}$, we find the final relevant rotationally averaged tensor element to be

$$\left\langle \mu_+^2 \mu_-^2 \right\rangle_{xxxx} = \frac{|\mu|^4}{15} \Big[3\left(\mu_{+_x}\mu_{+_x}\mu_{-_x}\mu_{-_x}\right) + 3\left(\mu_{+_y}\mu_{+_y}\mu_{-_y}\mu_{-_y}\right)$$
$$+ 4\left(\mu_{+_x}\mu_{+_y}\mu_{-_x}\mu_{-_y}\right) + \left(\mu_{+_x}\mu_{+_x}\mu_{-_y}\mu_{-_y}\right) + \left(\mu_{+_y}\mu_{+_y}\mu_{-_y}\mu_{-_y}\right) \Big]$$
$$= \frac{|\mu|^4}{15} \Big[3(1+\cos\phi)^2 (1-\cos\phi)^2 + 3(\sin\phi)^2 (\sin\phi)^2$$
$$+ 4(1+\cos\phi)(\sin\phi)(1-\cos\phi)(\sin\phi)$$
$$+ (1+\cos\phi)^2 (\sin\phi)^2 + (1-\cos\phi)^2 (\sin\phi)^2 \Big]$$
$$= \frac{4|\mu|^4}{15}(1+\cos\phi)(1-\cos\phi). \tag{6.51}$$

This result, too, is consistent with our expectations – with two of the μ_+ dipole moments and two of the μ_-, we find the rotationally averaged element to be the product of the linear feature angle dependencies.

These rotationally averaged products can be combined as in Eqs. (6.44) – (6.47) to determine the relative behavior of the four features in the 2D spectra. We note that the four features in both rephasing and non-rephasing spectra depend on the same rotationally averaged tensor products, which determine the relative peak amplitudes. Both rephasing and non-rephasing spectra have similar amplitudes, but are potentially quite different in their overall structures due to the different symmetries of the four spectral features. The four relative peak amplitudes scale as

$$S_{++} \propto 2\left\langle \mu_+^2 \mu_+^2 \right\rangle_{xxxx} \propto 24(1+\cos\phi)^2, \tag{6.52}$$

$$S_{--} \propto 2\left\langle \mu_-^2 \mu_-^2 \right\rangle_{XXXX} \propto 24(1-\cos\phi)^2 ,$$

(6.53)

$$S_{+-} \propto \left\langle \mu_+^2 \mu_-^2 \right\rangle_{XXXX} - \left\langle \mu_+^2 \mu_+^2 \right\rangle_{XXXX} \propto 8(\cos\phi+1)(\cos\phi+2),$$

(6.54)

and

$$S_{-+} \propto \left\langle \mu_+^2 \mu_-^2 \right\rangle_{XXXX} - \left\langle \mu_-^2 \mu_-^2 \right\rangle_{XXXX} \propto 8(\cos\phi-1)(\cos\phi-2).$$

(6.55)

Incoherent Population Transfer Effects in a Four-Level System Dimer

In this section, we consider the process of incoherent population transfer. The terms defined above for the intermediate time regime have no t_{32} dependence, which means the features are static as a function of population time. Incoherent population transfer is a statistical energy transfer process caused by interactions between the system and surrounding bath, affecting the population as a function of the population time t_{32}. From a simple Redfield kinetic model[20,21] for population transfer between a lower energy state A and higher energy state B, we have the rate equations

$$\frac{dA}{dt} = -k_u A + k_d B$$

$$\frac{dB}{dt} = k_u A - k_d B \quad ,$$

(6.56)

where the subscripts u and d denote uphill and downhill energy transfer rates, respectively. This leads to the well-known detailed balance relation,

$$\frac{k_u}{k_d} = \exp(-\frac{\hbar|\omega_{12}|}{k_B T}),$$

(6.57)

in which the ratio of the rate constants depends on the relative magnitude of the one-exciton splitting to the thermal energy. The survival and conditional probability functions are defined by the master equation

$$\frac{d}{dt_{32}}\begin{pmatrix} G_{AA}(t_{32}) & G_{AB}(t_{32}) \\ G_{BA}(t_{32}) & G_{BB}(t_{32}) \end{pmatrix} = \begin{pmatrix} -k_u & k_d \\ k_u & -k_d \end{pmatrix}\begin{pmatrix} G_{AA}(t_{32}) & G_{AB}(t_{32}) \\ G_{BA}(t_{32}) & G_{BB}(t_{32}) \end{pmatrix}.$$

(6.58)

The functions $G_{AA}(t_{32})$ and $G_{BB}(t_{32})$ are the survival probabilities of the A and B species. The function $G_{AA}(t_{32})$ [$G_{BB}(t_{32})$] is the conditional probability of finding B [A] species at t_{32}, when initially preparing A [B] species at a population time of 0. These equations have the solutions

$$G_{AA}(t_{32}) = \frac{k_d + k_u \exp[-(k_d + k_u)t_{32}]}{k_d + k_u},$$

(6.59)

$$G_{BB}(t_{32}) = \frac{k_u + k_d \exp\left[-(k_d + k_u)t_{32}\right]}{k_d + k_u},$$

(6.60)

$$G_{AB}(t_{32}) = \frac{k_u \left(1 - \exp\left[-(k_d + k_u)t_{32}\right]\right)}{k_d + k_u},$$

(6.61)

and

$$G_{BA}(t_{32}) = \frac{k_d \left(1 - \exp\left[-(k_d + k_u)t_{32}\right]\right)}{k_d + k_u}.$$

(6.62)

Of the eight remaining terms for each the rephasing and non-rephasing signals described by Eqs. (6.30) – (6.37), four are GSB, two are SE, and two are ESA. The GSB terms cannot experience population transfer during the population time since their free evolution is on the ground state. The SE and ESA terms will each be split into two terms – a term that does not undergo population transfer, and a term that does undergo population transfer. The SE and ESA terms that contribute to diagonal (off-diagonal) features will contribute to an off-diagonal (diagonal) feature if population transfer occurs. The rephasing and non-rephasing terms resulting from these population transfer probabilities are shown in Figs. 6.6 and 6.7, respectively. The figures are separated by the spectral features that they contribute to. Eqs. (6.44) – (6.47) are thus modified, resulting in the population transfer inclusive relative peak height amplitudes behaving as

$$S_{++} \propto (1 + G_{++}(t_{32})) \left\langle \mu_+^2 \mu_+^2 \right\rangle_{XXXX} - G_{+-}(t_{32}) \left\langle \mu_-^2 \mu_+^2 \right\rangle_{XXXX} \tag{6.63}$$

$$S_{--} \propto (1 + G_{--}(t_{32})) \left\langle \mu_-^2 \mu_-^2 \right\rangle_{XXXX} - G_{-+}(t_{32}) \left\langle \mu_-^2 \mu_-^2 \right\rangle_{XXXX} \tag{6.64}$$

$$S_{+-} \propto (1 + G_{+-}(t_{32})) \left\langle \mu_+^2 \mu_-^2 \right\rangle_{XXXX} - G_{++}(t_{32}) \left\langle \mu_+^2 \mu_+^2 \right\rangle_{XXXX} \tag{6.65}$$

and

$$S_{-+} \propto (1 + G_{-+}(t_{32})) \left\langle \mu_+^2 \mu_-^2 \right\rangle_{XXXX} - G_{--}(t_{32}) \left\langle \mu_-^2 \mu_-^2 \right\rangle_{XXXX}. \tag{6.66}$$
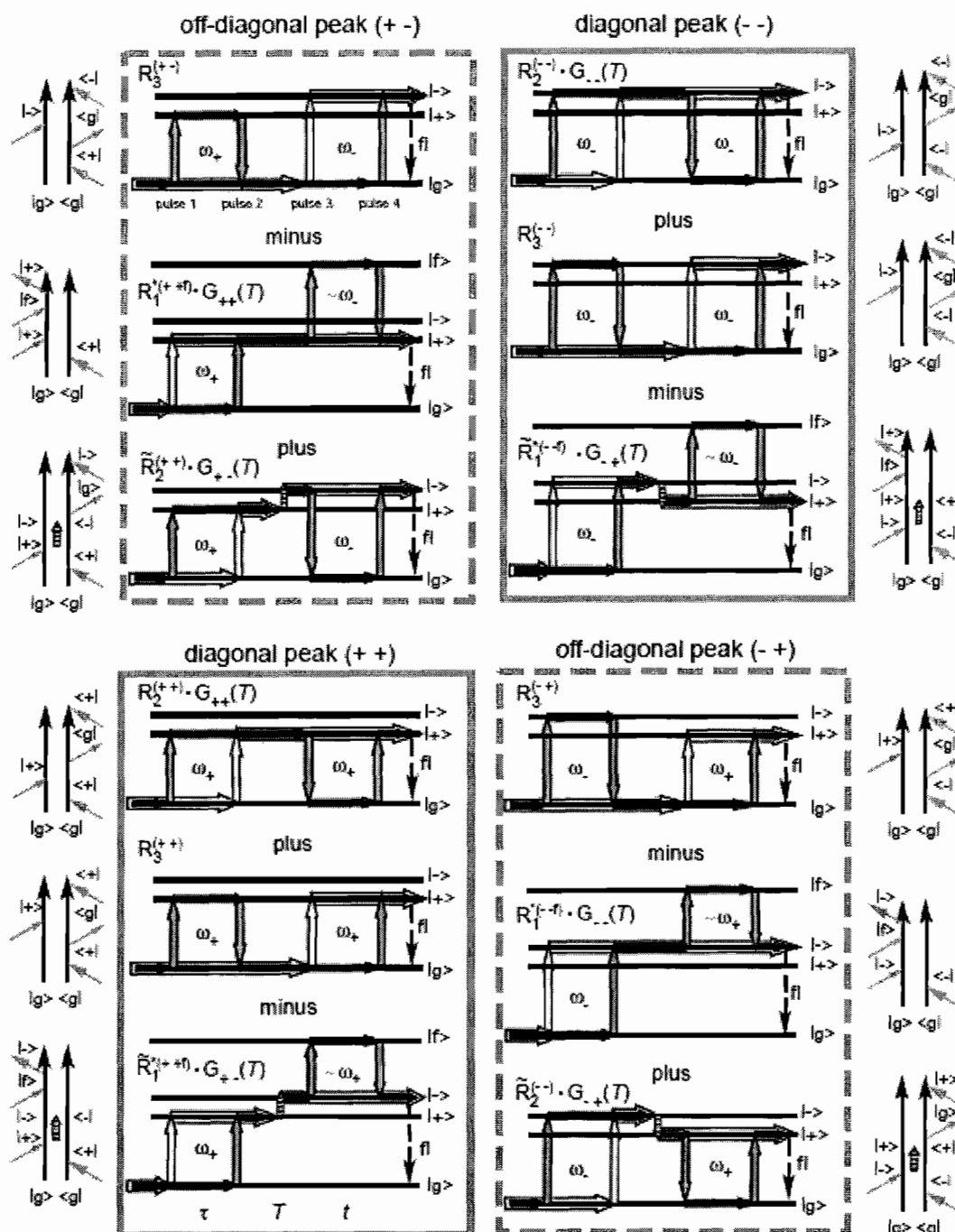
Figure 6.6: Rephasing signal pathways for 2D-ECS experiments on dimers in the intermediate time regime, considering incoherent energy transfer with Redfield theory. The ladder diagrams yield identical information as more familiar Feynman diagrams. Matching Feynman diagrams are shown next to the equivalent ladder diagram. Pathways are split according to the spectral feature they contribute to, organized in the same relative placements as the four features in a 2D dimer spectrum.
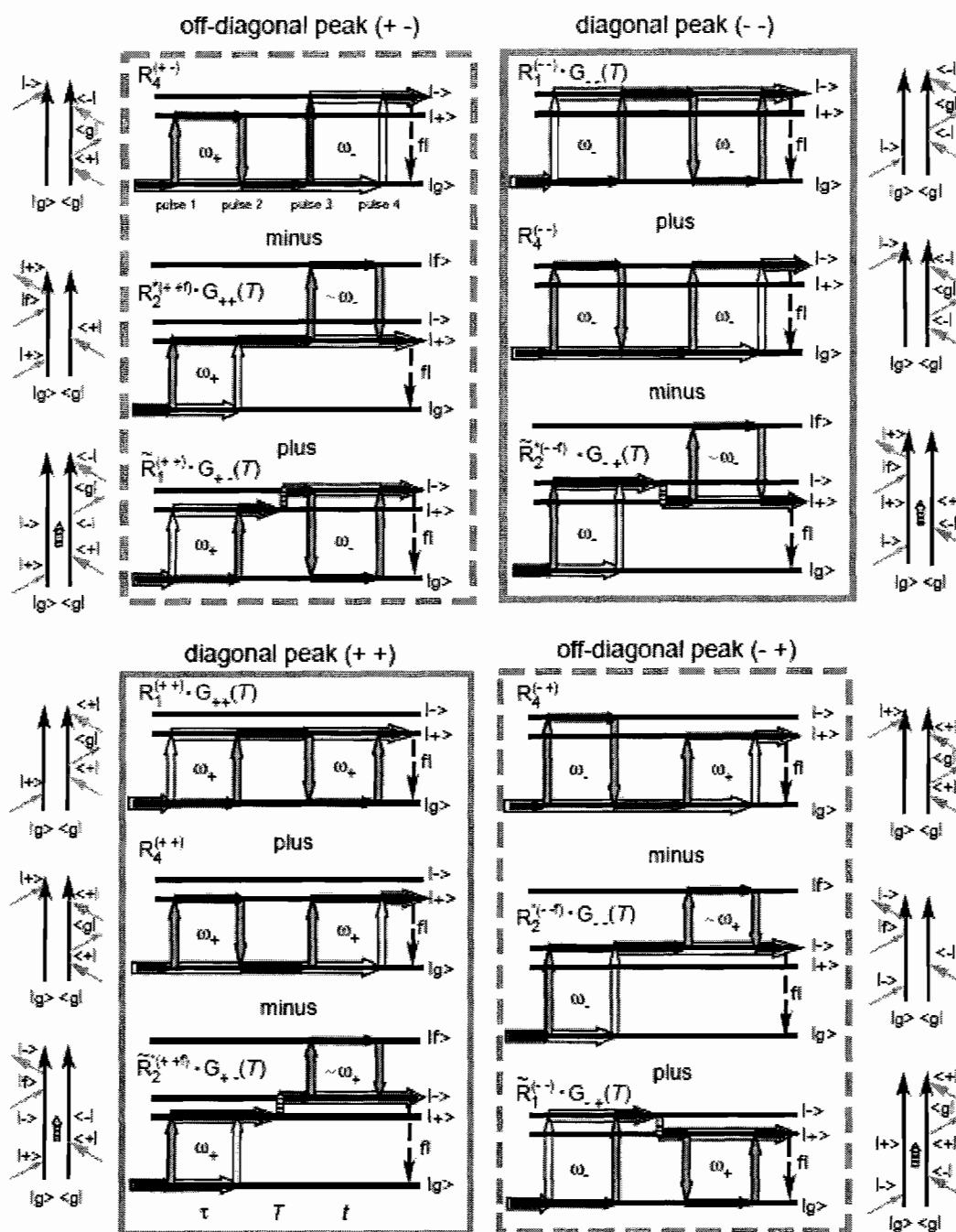
Figure 6.7: Non-rephasing signal contributions for 2D PM-ECS experiments on dimers in the intermediate time regime with population transfer. Equivalent Feynman diagrams are placed next to the corresponding pulse pathway diagram.

Experimental Apparatus and Procedure

2D PM-ECS Apparatus: 6 W of a 532 nm CW laser (Coherent, Verdi V-18) pump a Ti:Sapphire seed laser (Coherent, MIRA), generating 650 mW of 35 fs pulses at 76 MHz repetition rate. Two-thirds of the output power of the seed is temporally stretched before entering a regenerative amplifier (Coherent, RegA 9050), pumped by 12 W of the V-18. The RegA injects one out of every ~300 stretched seed pulses, amplifying it substantially to create a pulse train with 2.35 W power and 250 kHz repetition rate. This pulse train is compressed, and split between two optical parametric amplifiers (Coherent, OPA 9400), each receiving ~900 mW. The OPAs act as tunable femtosecond light sources across the wavelength range 480 nm – 700 nm. For the experiments described within, the OPAs have center wavelengths of 603 nm, and a bandwidth at the sample of 12 nm, corresponding to a Gaussian time-bandwidth limited pulse length of ~45 fs. A simplified schematic of the remainder of the experimental apparatus is shown in Fig. 6.8. The apparatus external to the light sources is very similar to that employed in the 2D Rb experiments. The pulse trains, after exiting the OPAs, double-pass through a pair of SF10 prisms (Newport, Brewster's Angle) for dispersion pre-compensation. Interferometric autocorrelations are performed using a 0.5 mm BBO crystal. Typical pulse widths recovered from autocorrelations are ~75 fs, significantly longer than the time-bandwidth limited expectation, due to high dispersive properties of SF10 prisms that are necessitated by table configuration constraints and high dispersive properties of the TeO_2 acousto-optics (AO).

After dispersion pre-compensation, the beams are incident on separate but identical Mach-Zender interferometers (MZI). The beams are split with 50/50 beamsplitters (CVI, custom). Each arm of each MZI has a TeO_2 AO, used to generate linear phase sweeps as detailed in chapters II and III, with the same difference frequencies of 5 kHz between pulses 1 & 2, and 8 kHz between pulses 3 & 4. These frequencies are chosen such that modulations between pulse pairs other than other than 1 & 2 or 3 & 4, and the difference and sum frequencies of 3 kHz and 13 kHz, fall outside the bandwidth of the lock-in amplifiers. The first order Bragg peak from each of the AOs is isolated and collimated. One arm of each interferometer has a fixed path length, while the other has a computer controlled delay stage with 20 nm precision, used to control the relative arrival time between the two separate pulses trains in a particular interferometer. The beams are recombined collinearly at second beamsplitter. These collinear pulse pairs from each interferometer are combined collinearly by a final beamsplitter, with a third delay stage controlling the relative arrival time between the separate interferometers. The final, four-pulse sequence is focused into the sample by a 75 mm lens to a spot size of $\sim$15 μm. The sample is in a flow cell with 3 mm path length (Starna), with a flow rate of $\sim$1 mL/min, pumped by a peristaltic pump from a reservoir with a total fluid volume of $\sim$6 mL. Emitted fluorescence is filtered by a 620 nm long pass filter and collected by a pair of 75 mm achromatic doublet lenses, and focused onto an avalanche photodiode (APD). Collected fluorescence signals are sent to two lock-in amplifiers (Stanford Research Systems, SR830).

Reference signals are generated as described in chapters II and III. Monochromators are used to spectrally filter the pulse pairs and generate reference signals oscillating at the AO difference frequencies of 5 kHz and 8 kHz. The spectral filtering temporally broadens the pulses, generating stable reference signals out to delay times of ~5 ps, much longer than the pulse durations themselves. The reference signals are combined by a frequency mixer to create the 3 kHz difference and 13 kHz sum frequency reference signals. The sum and difference signals are sent to the same lock-in amplifiers as the fluorescence, demodulating the fluorescence signals to isolate components oscillating at sum and difference frequencies.

The demodulated signals are collected via computer controlled analog-to-digital data acquisition, recording $X_{sum(dif)}(t_{43}, t_{32}, t_{21})$ and $Y_{sum(dif)}(t_{43}, t_{32}, t_{21})$. Time-domain data sets are collected starting at the time origin, and extending to time delays of 240 fs along the t_{43} and t_{21} axes. Step size is 10 fs, creating 25×25 arrays of data. The lock-in amplifier time constant is 1 s for MgTPP in liposome samples and 300 ms for MgTPP in toluene. In-phase and in-quadrature data is combined as per the procedures outlined prior.

Sample Preparation: Liposomal samples were prepared in accordance to the procedures in Ref. [22]. MgTPP in toluene with a known optical density was roto-evaporated in a spherical flask until dry. 1,2-distearoyl-*sn*-glycero-3-phosphocholine (DSPC) was dissolved in dichloromethane, and an amount was added to the flask to create a 70:1 DSPC:MgTPP ratio, and roto-evaporated until dry. Nanopure water was added to the flask, and the flask was alternated between being heated in a bath to a temperature of no

more than 70° C and sonicated for a period of 15 – 30 minutes. Once the lipid and porphyrin mixture was dissolved in water, it was filtered twice through glass wool packed pipettes. Uniform liposomal membrane sizes are creatable via pressure extrusion through 100 – 1000 nm pore nylon membranes. The sample with 7:1 DSPC:MgTPP ratio was created with the same procedure. MgTPP was also dissolved in toluene for an additional sample. All samples were diluted to have an optical density of ~0.15 for a 3 mm path length.
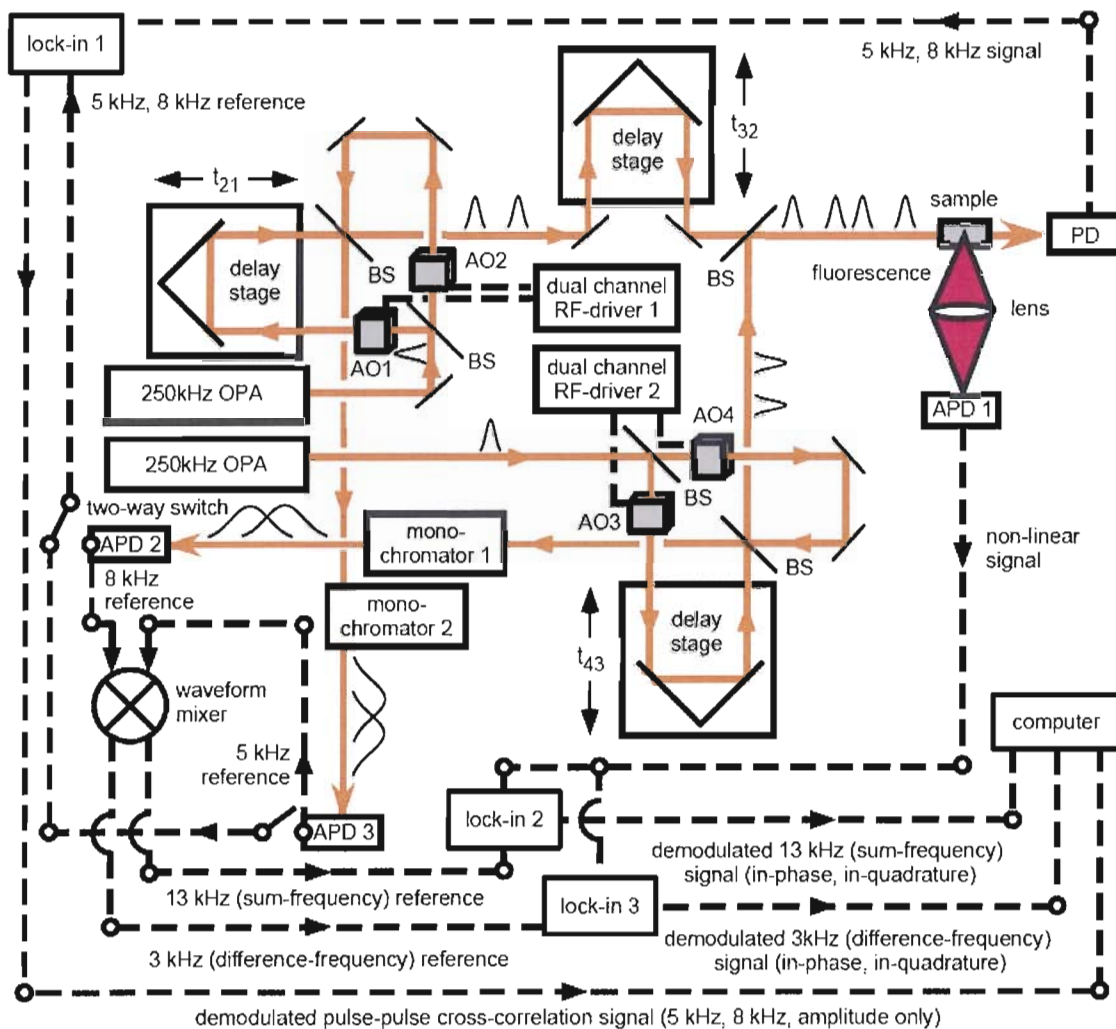
Figure 6.8: Shematic diagram of the experimental setup for 2D PM-ECS experiments in the visible wavelength range. Abbreviations are as follows: Amplified photodiode (APD), *p-i-n* photodiode (PD), acousto-optic Bragg cell (AO), beam splitter (BS), optical parametric amplifier (OPA).

Magnesium Tetraphenylporphyrin

The upper left-hand corner of Fig. 6.9A shows the molecular structure diagram for magnesium tetraphenylporphyrin (MgTPP). MgTPP has fourfold symmetry about the Mg atom. MgTPP has two degenerate transition dipole moments, whose directions are across the Mg, through opposite nitrogen atoms. Absorption spectra were collected for three distinct samples, shown in Fig. 6.9A and displaced vertically: MgTPP in toluene (bottom), 70:1 DSPC:MgTPP in nanopure water (middle) and 7:1 DSPC:MgTPP in nanopure water (top). The first two samples show spectral characteristics of broadened, well separated electronic features in condensed phase, as expected. Between 550 and 650 nm there are two inhomogeneously broadened features. The Q(0,0) transition centered around 605 nm and the Q(1,0) transition centered around 565 nm are transitions with zero and one vibrational quanta for the same electronic energy level, respectively. Porphyrin spectra are quite sensitive to solvent, so the small differences between MgTPP in toluene and 70:1 DSPC:MgTPP in water are not unexpected. Tetraphenylporphyrins are known to form dimers in lipid membranes with a concentration of around 7 lipids to 1 porphyrin.[22] The linear absorption spectrum shows clear evidence of excitonic structure. The Q(0,0) transition has two distinct features, each shifted by an equal energy relative to the monomer Q(0,0) center transition energy, as expected for a dimer of two-level systems. The lower energy feature has significantly larger amplitude than the higher energy feature, meaning that the aggregates are more J-like than H-like.
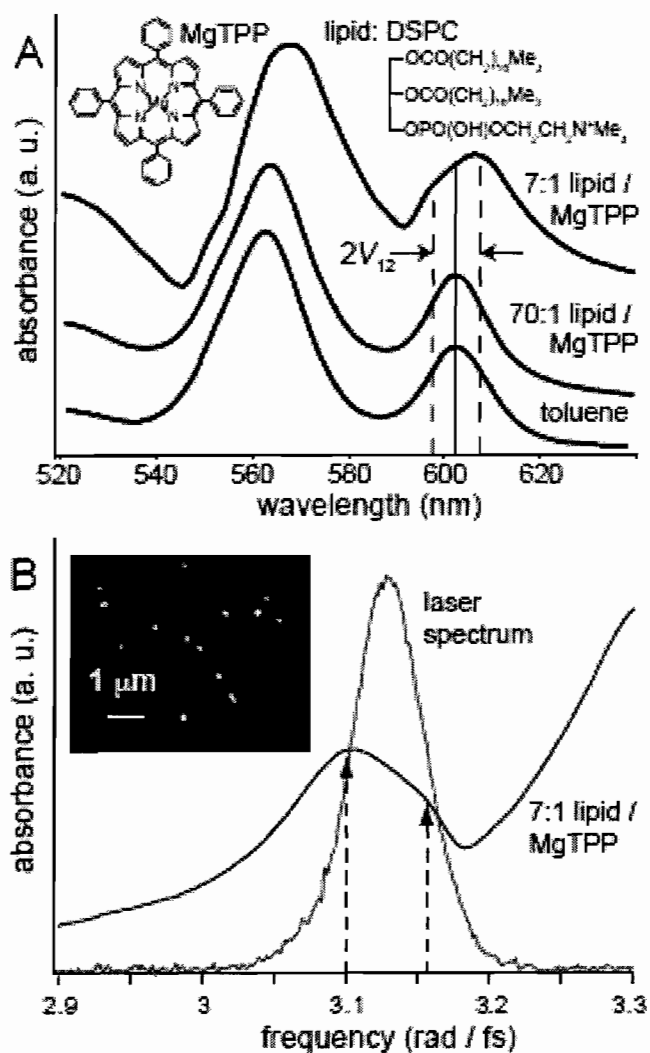
Figure 6.9: (A) Molecular structure of MgTPP, and linear absorption spectra for three samples – MgTPP in toluene, a 70:1 ratio of DSPC:MgTPP in nanopure water, and a 7:1 ratio of DSPC:MgTPP in nanopure water. The first two samples show spectral features characteristic of monomers, while the 7:1 sample shows clear exciton structure features. (B) Overlap of the Q(0,0) band for the 7:1 MgTPP sample and the laser excitation spectrum.

2D PM-ECS Experiments on MgTPP in Lipid Bilayer Vesicles

Fig. 6.9B shows the overlap of our laser spectrum with the MgTPP dimer absorption spectrum on a frequency scale. The excitation spectrum in centered at the monomer center transition frequency, directly between the two main dimer features in the linear spectrum. Experiments are performed on the three MgTPP samples described above. In Figs. 6.10 and 6.11 rephasing and non-rephasing results are presented, respectively, for all three samples for a population time of 0 fs. Both experimental data, in panel A, and theoretical calculations, in panel B, are presented. The top row of plots is for MgTPP in toluene, the middle row is for the low concentration of MgTPP to lipids, and the bottom row is the data for the higher concentration of MgTPP in lipids. Each data set shows the absolute value, real, and imaginary components of the third-order susceptibility, from left to right. The two monomer samples, MgTPP in toluene and the low concentration of MgTPP to lipids in water, behave as simple, broadened two-level systems for both the rephasing and non-rephasing susceptibilities, as expected. The 2D features in the absolute value, real, and imaginary components of the third-order susceptibility are familiar results for 2D spectra of two-level systems,[17,23,24] and are centered at the expected frequencies. The experimental results are in agreement with calculated 2D spectra for two-level systems. In the theory presented above, we did not account for spectral broadening. In these calculations we do so by multiplying the time-resolved data by a windowing function, similar to the windowing function used to truncate the Rb data in chapter III. The broadening functions for the toluene and 70:1 calculations have standard deviations of 51 fs and 56 fs, respectively. The larger temporal
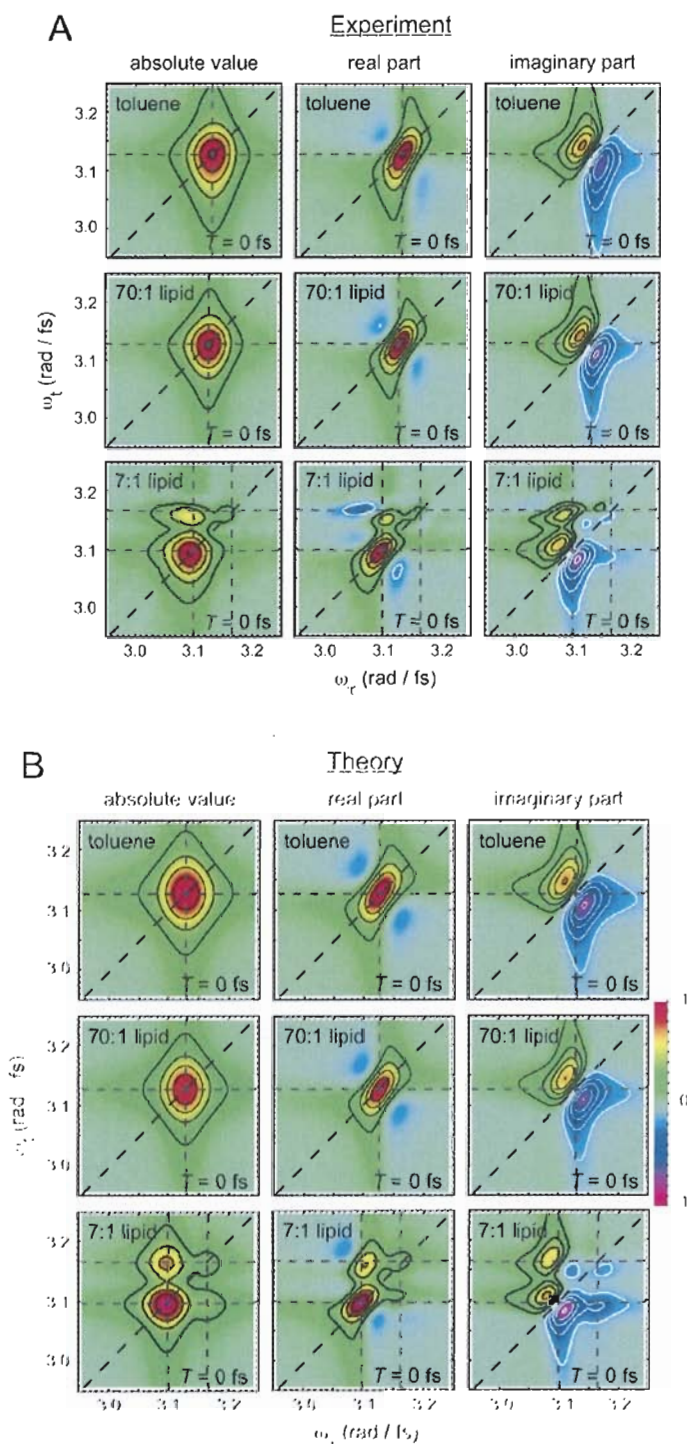
Figure 6.10: (A) Experimental and (B) calculated 2D rephasing spectra for MgTPP samples. We find very good agreement, between relative feature signs and coordinates for a model angle of 65°. Monomer spectra show expected structure. Dimer spectra show four features that can be used to characterize local structure.
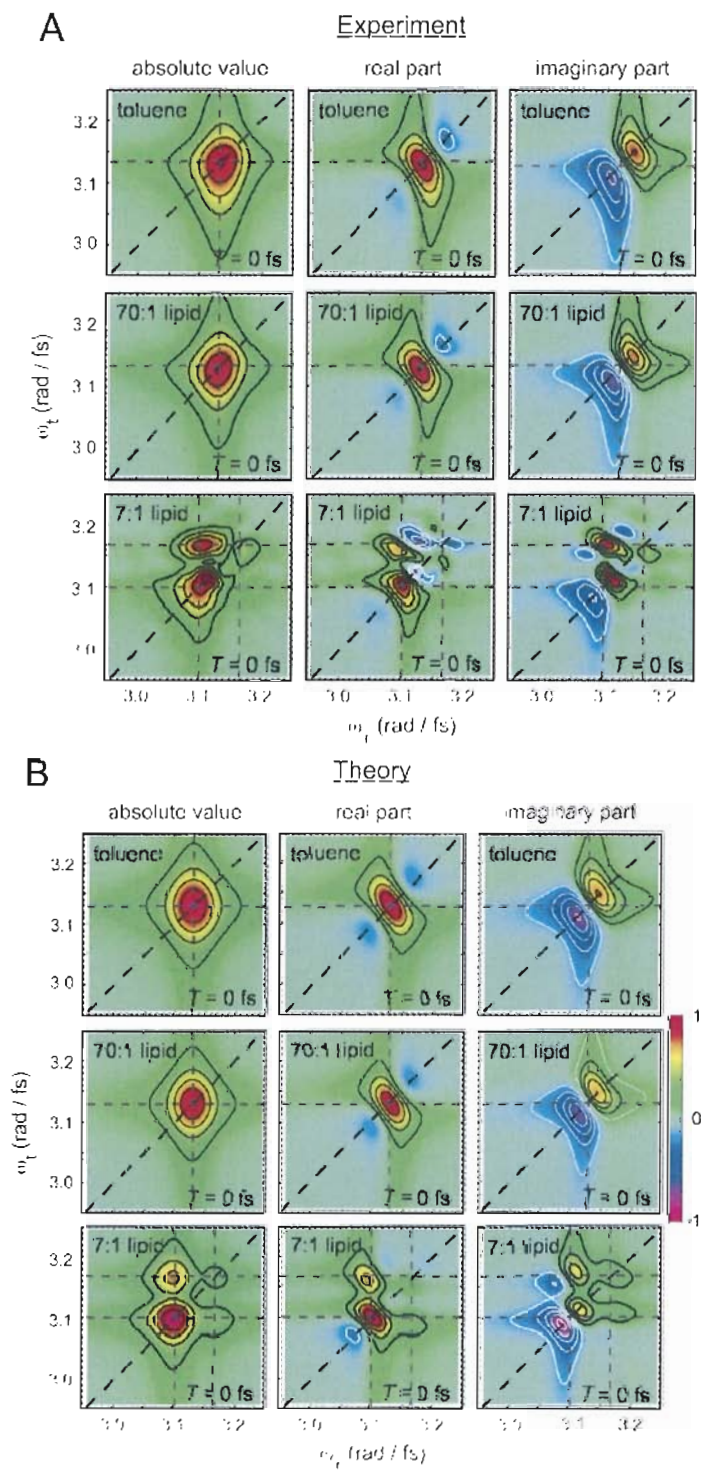
Figure 6.11: Non-rephasing spectra for (A) experiment and (B) theory. There is very good agreement between measured spectral features and model calculations for a relative dipole angle of 65°.

standard deviation for the 70:1 sample corresponds to slightly narrower 2D spectral features in comparison to MgTPP in toluene, correlating to the more structured environment inside the lipid vesicle bilayers. The experimental results are in agreement with this. Results are similar for both rephasing and non-rephasing data – non-rephasing spectra are simply rotated with respect to rephasing spectra, reflecting the expected symmetry difference.[17,23,24]

The results for the 7:1 DSPC:MgTPP sample show notably greater complexity in both rephasing and non-rephasing third-order susceptibilities. It is immediately evident that there are two distinct features along the diagonal and additional structure in the off-diagonal regions that signifies coupling between the diagonal features. While MgTPP monomers have two degenerate transition dipole moments, as described above, we only see two clear diagonal features, characteristic of a dimer of two-level systems. For now, we will treat this as a dimer of two-level systems, similar to many theoretical treatments of porphyrin dimers, to gauge how well our results agree with a simple model. Using Eqs. (6.45) – (6.48) we find that for a relative dipole interaction angle of 65° we achieve very good agreement with the collected 2D susceptibilities for the rephasing spectra. The broadening function has a standard deviation of 60 fs, reflecting motional narrowing of the linewidths of the exciton features in comparison to the monomer features. For the rephasing spectra in Fig. 6.8 we see that while the amplitudes of all features are not identical when comparing theory to data, the shapes and locations of the individual features are in excellent agreement. Similarly, the non-rephasing spectra in Fig. 6.9 show features centered at the same frequencies as the rephasing spectra, but with the expected

symmetry of a non-rephasing third-order susceptibility. Comparing experimental results to the calculated spectra once again finds very good agreement. Similar features are visible in almost all areas of the spectra, but with some discrepancy between calculations and experimental data.

The J- and H-aggregate examples in Fig. 6.1 defined the behavior of the spectra for systems with unidirectional transition dipole moments. For a dimer of molecules with twofold symmetry, like MgTPP if we consider a single transition dipole moment, dimer geometries will always have a relative dipole angle less than 90°. These MgTPP dimers, with the lower energy spectral feature being larger in amplitude, therefore have the "+" and "-" state designations assigned to the lower and higher energy features, respectively.

High resolution of dipole angle assignments is important for proper structural determination. In Fig. 6.12 we display the calculated absolute value rephasing spectra for three separate angles - 65°, which best fits our data for $t_{32} = 0$ fs, and ±20° (45° and 85°) to demonstrate the sensitivity of the relative spectral peak amplitudes to the dipole angle. For these angle changes, we see clear differences in the relationship between all four spectral features, and therefore have sensitivity to angle changes significantly smaller than these differences. 2D PM-ECS experiments can therefore be used as a technique for determination of aggregate structure with relatively high precision.

The features of the 2D spectra change very noticeably as a function of population time, as seen in Fig. 6.13 for both non-rephasing (left) and rephasing (right) spectra. We show data from population times of 0 fs, 15 fs, 45 fs, and 1200 fs. The progression of data sets as a function of population time show rapid uphill energy transfer, with a
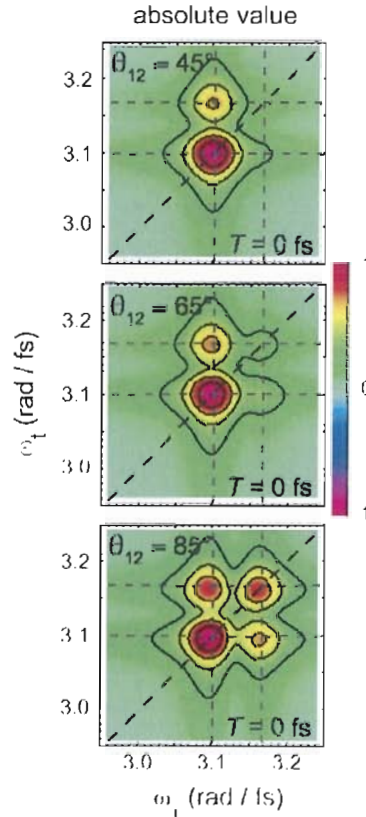
Figure 6.12: Absolute value of the 2D rephasing spectra for three relative dipole interaction angles. There are distinct differences in the relative peak amplitudes for the angles of 73°, 78°, and 83°, demonstrating the relative sensitivity of the 2D PM-ECS technique as a structural analysis tool.

characteristic time of 30 ± 5 fs. Uphill energy transfer is expected due to the thermal energy ($k_B T = 4.07 \times 10^{-21}$ J) being close in value to the energy difference of the one-exciton states ($\hbar \omega_{12} = 6.33 \times 10^{-21}$ J), which makes the ratio $k_u/k_d = 0.21$ by Eq. (6.54). Using these results and Eqs. (6.60) – (6.63) we find that the asymptotic values that the features rapidly approach do not agree well with the experimental values (calculations not shown). More specifically, the uphill energy transfer feature that we find in both rephasing and non-rephasing spectra is much larger than the simple kinetic model predicts. The downhill energy transfer feature is comparatively small, even at a

population time of 0 fs. This makes sense when one considers the donor states for uphill and downhill energy transfer. The lower energy state is the donor for uphill energy transfer, and is significantly larger than the higher energy feature, which is the donor for downhill energy transfer. The energy transfer feature itself cannot become larger than the initial value of its donor feature, so we are not surprised that the uphill energy transfer feature is larger than the downhill feature in these results. We are currently evaluating models that account for the discrepancy between the simple Redfield kinetic model and the experimental results.

Using Eq. (6.2) and results presented thus far, we can calculate the approximate transition dipole separation and compare the distance to possible dimer configurations. This analysis is currently ongoing, and we are proposing configurations such as Fig. 6.14 which take into account all four transition dipole moments, in attempts to match experimental results to a suitable model.

Summary

We have presented an extension of the 2D PM-ECS formalism for studies of exciton coupling in molecular complexes for use as a structural analysis tool. A theoretical treatment of dipole coupled two-level systems has been presented as a simple theory for the study of coupled dimers, taking into account the necessary rotational averaging of randomly oriented ensembles. For systems at room temperature, coherent oscillatory couping behavior is unlikely to be observed with PM-ECS experiments, so we work in the intermediate time regime.
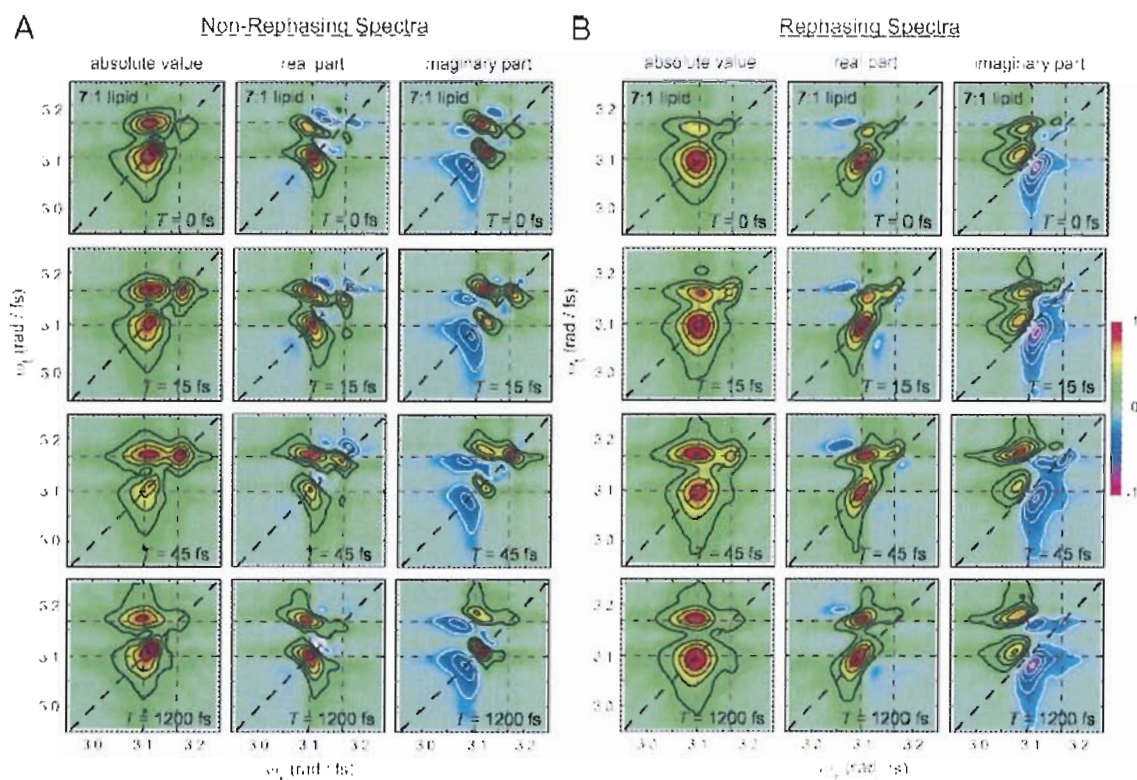
Figure 6.13: Experimental (A) rephasing and (B) non-rephasing spectra as a function of population time. Absolute value, real, and imaginary components of the spectra show rapid evolution of spectral features, with the uphill energy transfer feature becoming especially prominent. Current attempts to model the population transfer processes have been unsuccessful by use of a simple Redfield theory kinetic model. Each of the features is located at the same coordinate in both rephasing and non-rephasing data sets, with expected symmetry differences.

Results have been presented for 2D PM-ECS experiments on MgTPP complexes. Monomer systems in toluene and lipid bilayer vesicles behave as expected, showing simple two-level system dynamics. Aggregates of MgTPP in lipid bilayer vesicles show signature features of molecular dimers. Third-order susceptibilities for both rephasing and non-rephasing signals show similar behavior that is in good agreement with the dimer model theory. As a function of population time t_{32}, the off-diagonal features grow

in amplitude, and all four features approach asymptotic values. The uphill energy transfer feature is not accounted for by simple kinetic theory.

2D PM-ECS experiments are able to determine relative dipole angles in molecular dimers with high precision. This will allow experiments to be performed on a wide array of strategically labeled systems to better understand the local structure, orientation, and directional flow of excitation energy.
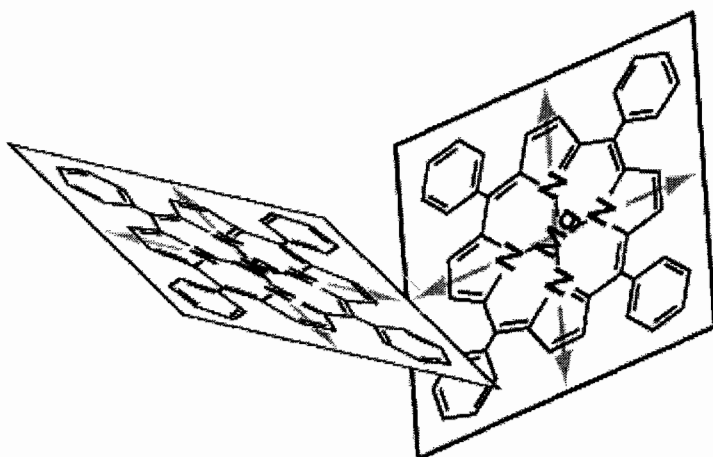

Figure 6.14: Possible configuration for MgTPP dimers in liposomal membranes based on experimental results and analysis thus far. We are investigating the possibility of configurations such as this as suitable models for our measured 2D spectra.

CHAPTER VII

CONCLUSION

As the scientific community delves deeper into the inner workings of the cell and its components, fluorescence labeling techniques will continue to be versatile methods for the study of dynamics and structure in biologically relevant systems across a vast range of timescales. This dissertation has presented two novel, high signal-to-noise phase modulation fluorescence spectroscopy techniques, PM-ECS and PM-FICS, as useful tools for the study of fluorescently labeled ensembles. In conclusion, a brief summary will be presented for each of these methods and the experimental results, and future directions will be proposed.

Summary of PM-FICS Experiments

The PM-FICS technique utilizes modulated intensity and polarization gratings to separate conformational dynamics of coupled chromophore systems from their diffusive motion. We successfully separate the translational and optical anisotropy signal components for DsRed, a naturally occurring obligate tetramer of fluorescent chromophores. The results for the translational dynamics mimic the expected behavior of a particle undergoing Brownian motion for both two-point (chapter IV) and joint (chapter

V) distribution functions and two-dimensional spectral densties. Plots of the distribution functions and spectral densities for the depolarization angle show markedly different behavior, compared to the translational dynamics. The two-point distribution functions clearly depart from a linear broadening with respect to the time interval t_{21}. The two-dimensional spectral densities of the mean depolarization angles are much more complicated than the simple, expected Lorentzian lineshapes for translational dynamics. We find broad distributions of transition rates in the 2D spectral densities, with two main features at 10 and 14 Hz. On long timescales (~8 second time constant) we see clear evidence of transitions between these "fast" and "slow" frequencies. We calculate the joint distributions, finding that there are many distinct conformational transitions that agree well with prior crystallographic analysis, allowing us to propose the thermally driven conformation transition pathway mechanism shown in Fig. 5.6.

Summary of PM-ECS Experiments

PM-ECS is an ultrafast four-pulse technique, utilizing collinear pulse geometry. The resultant fluorescence signal is collected, and we isolate the terms linear in each of the four time-ordered fields in order to generate third-order susceptibilities that can characterize coupling processes between distinct electronic modes and generate time-dependant structural information. Proof-of principle experiments for the PM-ECS technique were performed on atomic rubidium, with excellent agreement between theory and experimental data. The success of these initial measurements inspired us to study exciton dynamics in solution at room temperature. The results of experiments on self-

forming porphyrin dimers in lipid bilayer vesicles, along with two monomer control studies, were presented in chapter VI. We find clear energy transfer features in both uphill and downhill directions, and diagonal features in agreement with evidence of exciton behavior in the linear spectra. The features in the 2D spectra are well modeled by a simple dimer model in the intermediate time regime for a population time of 0 fs. As the population time increases there are significant chances to both the rephasing and nonrephasing spectra. The uphill energy transfer feature rapidly increases in amplitude, which is not well matched by simple kinetic models. We are currently examining explanations for the evolution of the features that we see.

Future Directions

Currently, PM-FICS experiments are being performed to study nanoparticle fluctuations in glass-forming polymer liquids, specifically fluorescent CdSe quantum dots in polybutadiene blends. Preliminary studies show promise for characterizing the dynamical heterogeneity present in glass-forming liquids by performing a sequence of temperature dependent experiments. The polymer entanglement length scale will be altered by varying the molecular weight of the polymer blends. We are also interested in studying the effects of the presence of nanoparticles on the glass forming liquids. Two-dimensional joint distribution functions will be useful for characterizing the length scales of the heterogeneous domains and the time scales of interconversion between fast and slow domains near the glass transition.

Using the 2D PM-ECS technique, we will continue studies of porphyrin aggregates in lipid bilayer vesicles. We will use the membranes as structured environments for the study of coherence and energy redistribution in the membrane-assisted organization of porphrin aggregates. By performing studies on porphyrin dimers separated by flexible or rigid ester chains in solution and in membranes, we will learn about the structural organization properties of the membrane with respect to molecular aggregates and arrays, and about the suitability of using membranes as environments for highly efficient self-assembling energy transfer complexes. We have received porphyrin dimer samples from collaborators in the Molinski lab at the University of California, San Diego. One of the dimer samples has the two porphyrins separated by a flexible ester chain, while a second sample separates the two porphyrins with a rigid ester chain, with the porphyrins in known relative positions and orientations.

Another set of experiments will be performed with the both the PM-ECS and PM-FICS techniques as tools for structural analysis of protein-nucleic acid complexes. Results will reveal information concerning relative separation, local orientation, and dynamic behavior of specifically selected pairs of nucleotide bases in DNA and RNA molecules. The specific nucleotide bases that we choose to examine will be labeled with 6-MI, a fluorescent chromophore that can be used as a non-invasive replacement for guanine, with spectrally separate absorption and emission features from unlabeled DNA or RNA. These experiments will be used to study the mechanisms of DNA polymerase and helicase, protein-DNA complexes that are integral to the biological processes that enact and regulate gene expression.

BIBLIOGRAPHY

Chapter I

[1]   Tian, P.; Keusters, D.; Suzuki, Y.; Warren, W. S. Femtosecond phase-coherent two-dimensional spectroscopy. *Science* **2003**, *300*, 1553-1555.

[2]   Li, C.; Wagner, W.; Ciocca, M.; Warren, W. S. Multiphoton femtosecond phase-coherent two-dimensional electronic spectroscopy. *J. Chem. Phys.* **2007**, *126*, 164307/1-164307/6.

[3]   Keusters, D.; Tan, H. -S.; Warren, W. S. Role of pulse phase and direction in two-dimensional optical spectroscopy. *J. Phys. Chem. A* **1999**, *103*, 10369-10380.

[4]   Berland, K. M. Fluorescence correlation spectroscopy: new methods for detecting molecular associations. *Biophys J* **1997**, *72*, 1487-1488.

[5]   Woutersen, S.; Hamm, P. Nonlinear two-dimensional vibrational spectroscopy of peptides. *J. Phys. Cond. Matt.* **2002**, *14*, R1035-R1062.

[6]   Cho, M. *Two-Dimensional Optical Spectroscopy*, CRC Press: Boca Raton, 2009.

[7]   Mukamel, S. Multidimensional femtosecond correlation spectroscopies of electronic and vibrational excitations. *Annu. Rev. Phys. Chem.* **2000**, *51*, 691-729.

[8]   Humble, T. S.; Cina, J. A. Nonlinear wave-packet interferometry and molecular state reconstruction in a vibrating and rotating diatomic molecule. *J. Phys. Chem. B* **2006**, *110*, 18879-18892.

[9]   Engel, G. S.; Calhoun,G. R.; Read, E. L.; Ahn, T. -K.; Mancal, T.; Cheng, Y. -C.; Blankenship, R. E.; Fleming, G. R. Evidence for wavelike energy transfer through quantum coherence in photosynthetic systems. *Nature* **2007**, *446*, 782-786.

Chapter II

[1]   Cina, J.A., Unpublished notes.

[2]   Humble, T. S. Ph.D. Thesis, University of Oregon, **2005**.

[3]   Tian, P.; Keusters, D.; Suzuki, Y.; Warren, W. S. Femtosecond phase-coherent two-dimensional spectroscopy. *Science* **2003**, *300*, 1553-1555.

[4]   Li, C.; Wagner, W.; Ciocca, M.; Warren, W. S. Multiphoton femtosecond phase-coherent two-dimensional electronic spectroscopy. *J. Chem. Phys.* **2007**, *126*, 164307/1-164307/6.

[5]   Humble, T. S.; Cina, J. A. Nonlinear Wave-packet interferometry and molecular state reconstruction in a vibrating and rotating diatomic molecule. *J. Phys. Chem. B* **2006**, *110*, 18879-18892.

[6]   Cina, J. A. Nonlinear Wavepacket interferometry for polyatomic molecules. *J. Chem. Phys.*, **2000**, *113*, 9488-9496.

[7]   Keusters, D.; Tan, H. -S.; Warren, W. S. Role of Pulse Phase and Direction in Two-Dimensional Optical Spectroscopy. *J. Phys. Chem. A* **1999**, *103*, 10369-10380.

[8]   Wefers, M. M.; Kawashima, H.; Nelson, K. A. Automated multidimensional coherent optical spectroscopy with multiple phase-related femtosecond pulses. *J. Chem. Phys.* **1995**, *102*, 9133-9136.

[9]   Kawashima, H.; Wefers, M. M.; Nelson, K. A. Femtosecond pulse shaping, multiple-pulse spectroscopy, and optical control. *Annu. Rev. Phys. Chem.* **1995**, *46*, 627-656.

[10]   Fourkas, J. T.; Wilson, W. L.; Wackerle, G.; Frost, A. E.; Fayer, M. D. Picosecond time-scale phase-related optical pulses: measurement of sodium optical coherence decay by observation of incoherent fluorescence. *J. Opt. Soc. Am. B* **1989**, *6*, 1905-1910.

[11]   Jonas, D. M. Two-dimensional femtosecond spectroscopy. *Annu. Rev. Phys. Chem.* **2003**, *54*, p. 425-463.

[12]   Mukamel, S. Principles *of Nonlinear Optical Spectroscopy*; Oxford University Press: Oxford, 1995.

[13]   Sakurai, J. J. *Modern Quantum Mechanics*. Addison-Wesley: New York, 1994.

[14]   Brixner, T.; Mancal, T.; Stiopkin, I. V.; Fleming, G. R. Phase Stabilized Two-Dimensional Electronic Spectroscopy. *J. Chem. Phys.* **2004**, *121*, 4221-4236.

[15]   Cowan, M. L.; Ogilvie, J. P.; Miller, R. J. D. Two-dimensional spectroscopy using diffractive optics based phased-locked photon echoes. *Chem. Phys. Lett.* **2004**, *386*, 184-189.

[16]   Hybl, J. D.; Albrecht, A. W.; Gallagher Feader, S. M.; Jonas, D. M. Two-dimensional electronic spectroscopy. *Chem. Phys. Lett.* **1998**, *297*, 307-313.

[17]   Hybl, J.D.; Ferro, A. A.; Jonas, D. M. Two-dimensional Fourier transform electronic spectroscopy. *J. Chem. Phys.* **2001**, *115*, 6606-6622.

[18]   Gallagher Feader, S. M.; Jonas, D. M. Two-Dimensional Electronic Correlation and Relaxation Spectra: Theory and Model Calculations. *J. Phys. Chem. A* **1999**, *103*, 10489-10505.

[19]   Zhang, T.; Borca, C. N.; Li, X.; Cundiff, S. T. Optical two-dimensional Fourier transform spectroscopy with active interferometric stabilization. *Opt. Express* **2005**, *13*, 7432-7441.

[20]   Mukamel, S. Multidimensional femtosecond correlation spectroscopies of electronic and vibrational excitations. *Annu. Rev. Phys. Chem.* **2000**, *51*, 691-729.

[21]   Engel, G. S.; Calhoun, T. R.; Read, E. L.; Ahn, T. -K.; Mancal, T.; Cheng, Y. -C.; Blankenship, R. E.; Fleming, G. R. Evidence for wavelike energy transfer: Quantum coherences in photosynthetic complexes, *Nature* **2007**, *446*, 782-786.

[22]   Brixner, T.; Stenger, J.; Vaswami, H. M.; Cho, M.; Blankenship, R. E.; Fleming, G. R. Two-dimensional spectroscopy of electronic couplings in photosynthesis. *Nature* **2005**, *434*, 625-628.

[23]   Khalil, M.; Demirdoven, N.; Tokmakoff, A. Coherent 2D IR Spectroscopy: Molecular Structure and Dynamics in Solution. *J. Phys. Chem. A* **2003**, *107*, 5258-5279.

[24]   Khalil, M.; Demirdoven, N.; Tokmakoff, A. Obtaining Absorptive Line Shapes in Two-Dimensional Infrared Vibrational Correlation Spectra. *Phys. Rev. Lett.* **2003**, *90*, 047401/1-047401/4.

[25]   Horowitz, P.; Hill, W. *The Art of Electronics*. Cambridge University Press: Cambridge, 1980.

[26]   Lepetit, L.; G. Cheriaux, M. Joffre, Linear techniques of phase measurement by femtosecond spectral interferometry for applications in spectroscopy. *J. Opt. Soc. Am. B* **1995**, *12*, 2467-2474.

[27]   Lepetit, L.; M. Joffre, Two-dimensional nonlinear optics using Fourier-transform spectral interferometry. *Opt. Lett.* **1996**, *21*, 564-566.

[28]   de Boeij; W. P., Pshenichnikov, M. S.; Wiersma, D. A. Phase-locked heterodyne-detected stimulated photon echo. A unique tool to study solute-solvent interactions. *Chem. Phys. Lett.* **1995**, *238*, 1-8.

[29]   de Boeij; W. P., Pshenichnikov, M. S.; Wiersma, D. A. Heterodyne-detected stimulated photon echo: applications to optical dynamics in solution. *Chem. Phys.* **1998**, *233*, 287-309.

[30]   Scherer, N. F.; Matro, A.; Ziegler, L. D.; Du, M.; Carlson, R. J.; Cina, J. A.; Fleming, G. R.; Rice, S. A. Fluorescence-detected wave packet interferometry. II. Role of rotations and determination of the susceptibility. *J. Chem. Phys.* **1992**, *96*, 4180-4194.

[31]   Scherer, N. F.; Carlson, R. J.; Matro, A.; Du, M.; Ruggiero, A. J.; Romero-Rochin, V.; Cina, J. A.; Fleming, G. R.; Rice, S. A. Fluorescence-detected wave packet interferometry: time resolved molecular spectroscopy with sequences of femtosecond phase-locked pulses. *J. Chem. Phys.* **1991**, *95*, 1487-1511.

[32]   Tekavec, P. F.; Dyke, T. R.; Marcus, A. H. Wave packet interferometry and quantum state reconstruction by acousto-optic phase modulation. *J. Chem. Phys.* **2006**, *125*, 194303/1-194303/19.

Chapter III

[1]   Johansson, L *Ark. Fys.* **1961**, *20*, 135-146.

[2]   Tekavec, P.F., Lott, G. A.; Marcus, A. H. Fluorescence-detected two-dimensional electronic coherence spectroscopy by acousto-optic phase modulation. *J. Chem. Phys.* **2007**, *127*, 214307/1-214307/21.

[3]   Horowitz, P.; Hill, W. *The Art of Electronics.* Cambridge University Press: Cambridge, 1980.

[4] Mukamel, S. *Principles of Nonlinear Optical Spectroscopy*. Oxford University Press: Oxford, 1995.

[5] Allen, L.; Eberly, J. H. *Optical Resonance and Two-Level Atoms*. Dover Publications, Inc.: New York, 1975.

[6] Press, W.H.; Teukolsky, S. A.; Vetterling, W. T.; Flannery, B. P. *Numerical Recipes in C, The Art of Scientific Computing*. Cambridge University Press: New York, 1997.

[7] Jonas, D. M. Two-dimensional femtosecond spectroscopy. *Annu. Rev. Phys. Chem.* **2003**, *54*, p. 425-463.

[8] Khalil, M.; Demirdoven, N.; Tokmakoff, A. Coherent 2D IR Spectroscopy: Molecular Structure and Dynamics in Solution. *J. Phys. Chem. A* **2003**, *107*, 5258-5279.

[9] Khalil, M.; Demirdoven, N.; Tokmakoff, A. Obtaining Absorptive Line Shapes in Two-Dimensional Infrared Vibrational Correlation Spectra. *Phys. Rev. Lett.* **2003**, *90*, 047401/1-047401/4.

Chapter IV

[1] Giepmans, B. N. G.; Adams, S. R.; Ellisman, M. H.; Tsien, R. Y. The fluorescent toolbox for assessing protein location and function. *Science* **2006**, *312*, 217-224.

[2] Field, S. F.; Bulina, M. Y.; Kelmanson, I. V.; Bielawski, J. P.; Matz, M. V. Adaptive evolution of multicolored fluorescent proteins in reef-building corals. *J. Mol. Evol.* **2006**, *62*, 332-339.

[3] Shaner, N. C.; Campbell, R. E.; Steinbach, P. A.; Giepmans, B. N. G.; Palmer, A. E.; Tsien, R. Y. Improved monomeric red, orange, and yellow fluorescent proteins derived from Discosoma sp. red fluorescent protein. *Nat. Biotechnol.* **2004**, *22*, 1567-1572.

[4] Wall, M. A.; Socolich, M.; Ranaganathan, R. The structural basis for red fluorescence in the tetrameric GFP homolog DsRed. *Nat. Struct. Biol.* **2000**, *7*, 1133-1138.

[5]   Yarbrough, D.; Wachter, R. M.; Kallio, K.; Matz, M. V.; Remington, S. J. Refined crystal structure of DsRed, a red fluorescent protein from coral, at 2.0-A resolution. *Proc. Nat. Acad. Sci.* **2001**, *98*, 462-467.

[6]   Gross, L. A.; Baird, G. S.; Hoffman, R. C.; Baldridge, K. K.; Tsien, R. Y.; The structure of the chromophore within DsRed, a red fluorescent protein from coral. *Proc. Nat. Acad. Sci.* **2000**, *97*, 11990-11995.

[7]   Bonsma, S.; Gallus, J.; Konz, F.; Purchase, R.; Volker, S. Light-induced conformational changes and energy transfer in red fluorescent protein. *J. Luminesc.* **2004**, *107*, 203-212.

[8]   Bonsma, S.; Purchase, R.; Jezowski, S.; Gallus, J.; Konz, F.; Volker, S. Green and red fluorescnt proteins: photo- and thermally induced dynamics probed by site-selective spectroscopy and hole burning. *ChemPhysChem* **2005**, *6*, 838-849.

[9]   Garcia-Parajo, M. F.; Koopman, M.; van Dijk, E. M. H. P.; Subramaniam, V.; van Hulst, N. F. The nature of fluorescence emission in the red fluorescent protein DsRed, revealed by single-molecule detection. *Proc. Nat. Acad. Sci.* **2001**, *98*, 14392-14397.

[10]   Heikal, A. A.; Hess, S. T.; Baird, G. S.; Tsien, R. Y.; Webb, W. W. Molecular spectroscopy and dynamics of intrinsically fluorescent proteins: coral red (dsRed) and yellow (Citrine). *Proc. Nat. Acad. Sci.* **2000**, *97*, 11996-12001.

[11]   Lounis, B.; Deich, J.; Rosell, F. I.; Boxer, S. G.; Moerner, W. E. Photophysics of DsRed, a red fluorescent protein, from the ensemble to the single-molecule level. *J. Phys. Chem. B* **2001**, *105*, 5048-5054.

[12]   Malvezzi-Campeggi, F.; Jahnz, M.; Heinze, K. G.; Dittrich, P.; Schwille, P. Light-induced flickering of DsRed provides evidence for distinct and interconvertible fluorescence states. *Biophys. J.* **2001**, *81*, 1776-1785.

[13]   Schenk, A.; Ivanchenko, S.; Rocker, C.; Wiedenmann, J.; Nienhaus, G. U. Photodynamics of red fluorescent proteins studied by fluorescence correlation spectroscopy. *Biophys. J.* **2004**, *86*, 384-394.

[14]   Fink, M. C.; Adair, K. V.; Guenza, M. G.; Marcus, A. H. Translational diffusion of fluorescent proteins by molecular Fourier imaging correlation spectroscopy. *Biophys. J.* **2006**, *91*, 3482-3498.

[15]   Kinosita, J. K.; Kawato, S.; Ikegami, A. A theory of fluorescence polarization decay in membranes. *Biophys. J.* **1977**, *20*, 289-305.

[16]   Cantor, C. R.; Schimmel, P. R. *Biophysical Chemistry Part II: Techniques for the study of biological structure and function.* Freeman: New York, 1980; Vol. 2.

[17]   Nitzan, A. *Chemical Dynamics in Condensed Phases.* Oxford University Press: Oxford, 2006.

[18]   Berne, B. J.; Pecora, R. *Dynamic Light Scattering.* Dover: Mineoloa, NY, 2000.

Chapter V

[1]   Frauenfelder, H.; Sligar, S. G.; Wolynes, P. G. The energy landscapes and motions of proteins. *Science* **1991,** *254,* 1598-1603.

[2]   Miyashita, O.; Onuchic, J. N.; Wolynes, P. G. Nonlinear elasticity, proteinquakes, and the energy landscapes of functional transitions in proteins. *Proc. Nat. Acad. Sci.* **2003,** *100,* 12570-12575.

[3]   Henzler-Wildman, K. A.; Lei, M.; Thai, V.; Kerns, S. J.; Karplus, M.; Kern, D. A heirarchy of timescales in protein dynamics is linked to enzyme catalysis. *Nature* **2007,** *450,* 913-918.

[4]   Boehr, D. B.; Dyson, H. J.; Wright, P. E. An NMR perspective on enzyme dynamics. *Chem. Rev.* **2006,** *106,* 3055-3079.

[5]   Hochstrasser, R. M. Two-dimensional spectroscopy at the infrared and optical frequencies. *Proc. Nat. Acad. Sci.* **2007,** *104,* 14190-14196.

[6]   Shaner, N. C.; Campbell, R. E.; Steinbach, P. A.; Giepmans, B. N. G.; Palmer, A. E.; Tsien, R. Y. Improved monomeric red, orange, and yellow fluorescent proteins derived from Discosoma sp. red fluorescent protein. *Nat. Biotechnol.* **2004,** *22,* 1567-1572.

[7]   Wall, M. A.; Socolich, M.; Ranaganathan, R. The structural basis for red fluorescence in the tetrameric GFP homolog DsRed. *Nat. Struct. Biol.* **2000,** *7,* 1133-1138.

[8]   Gross, L. A.; Baird, G. S.; Hoffman, R. C.; Baldridge, K. K.; Tsien, R. Y.; The structure of the chromophore within DsRed, a red fluorescent protein from coral. *Proc. Nat. Acad. Sci.* **2000,** *97,* 11990-11995.

[9]   Yarbrough, D.; Wachter, R. M.; Kallio, K.; Matz, M. V.; Remington, S. J. Refined crystal structure of DsRed, a red fluorescent protein from coral, at 2.0-A resolution. *Proc. Nat. Acad. Sci.* **2001**, *98*, 462-467.

[10]   Baird, G. S.; Zacharias, D. A.; Tsien, R. Y. Biochemistry, mutagenesis, and oligomerization of DsRed, a red fluorescent protein from coral. *Proc. Nat. Acad. Sci.* **2000**, *97*, 11984-11989.

[11]   Garcia-Parajo, M. F.; Koopman, M.; van Dijk, E. M. H. P.; Subramaniam, V.; van Hulst, N. F. The nature of fluorescence emission in the red fluorescent protein DsRed, revealed by single-molecule detection. *Proc. Nat. Acad. Sci.* **2001**, *98*, 14392-14397.

[12]   Bonsma, S.; Gallus, J.; Konz, F.; Purchase, R.; Volker, S. Light-induced conformational changes and energy transfer in red fluorescent protein. *J. Luminesc.* **2004**, *107*, 203-212.

[13]   Bonsma, S.; Purchase, R.; Jezowski, S.; Gallus, J.; Konz, F.; Volker, S. Green and red fluorescnt proteins: photo- and thermally induced dynamics probed by site-selective spectroscopy and hole burning. *ChemPhysChem* **2005**, *6*, 838-849.

[14]   Heikal, A. A.; Hess, S. T.; Baird, G. S.; Tsien, R. Y.; Webb, W. W. Molecular spectroscopy and dynamics of intrinsically fluorescent proteins: coral red (dsRed) and yellow (Citrine). *Proc. Nat. Acad. Sci.* **2000**, *97*, 11996-12001.

[15]   Malvezzi-Campeggi, F.; Jahnz, M.; Heinze, K. G.; Dittrich, P.; Schwille, P. Light-induced flickering of DsRed provides evidence for distinct and interconvertible fluorescence states. *Biophys. J.* **2001**, *81*, 1776-1785.

[16]   Schenk, A.; Ivanchenko, S.; Rocker, C.; Wiedenmann, J.; Nienhaus, G. U. Photodynamics of red fluorescent proteins studied by fluorescence correlation spectroscopy. *Biophys. J.* **2004**, *86*, 384-394.

[17]   Lounis, B.; Deich, J.; Rosell, F. I.; Boxer, S. G.; Moerner, W. E. Photophysics of DsRed, a red fluorescent protein, from the ensemble to the single-molecule level. *J. Phys. Chem. B* **2001**, *105*, 5048-5054.

[18]   Hendrix, J., C. Flors, P. Dedecker, J. Hofkens, and Y. Engelborghs, Dark states in moneric red fluorescent proteins studied by fluorescence correlation and single molecule spectroscopy *Biophys. J.* **2008**, *94*, p. 4103-4113.

[19]   Mukamel, S. *Principles of Nonlinear Optical Spectroscopy.* Oxford University Press: Oxford, 1995.

Chapter VI

[1]   Brixner, T.; Stenger, J.; Vaswani,H. M.; Cho, M.; Blankenship, R. E.; Fleming, G. R. Two-dimensional spectroscopy of electronic couplings in photosynthesis. *Nature* **2005**, *434*, 625-628.

[2]   Engel, G. S.; Calhoun, T. R.; Read, E. L.; Ahn, T. -K.; Mancal, T.; Cheng, Y. -C.; Blankenship, R. E.; Fleming, G. R. Evidence for wavelike energy transfer: Quantum coherences in photosynthetic complexes, *Nature* **2007**, *446*, 782-786.

[3]   Read, E. L.; Engel, G. S.; Calhoun, T. R.; Mancal, T.; Ahn, T. -K.; Blankenship, R. E.; Fleming, G. R. Cross-peak specific two-dimensional electronic spectroscopy. *Proc. Nat. Acad. Sci.* **2007**, *104*, 14203-14208.

[4]   Cho, M.; Vaswani, H. M.; Brixner, T.; Stenger, J.; Fleming, G. R. Exciton analysis in 2D electronic spectroscopy. *J. Phys. Chem. B* **2005**, *109*, 10542-10556.

[5]   Calhoun, T. R.; Ginsberg, N. S.; Schlau-Cohen, G. S.; Cheng, Y. -C.; Ballottari, M.; Bassi, R.; Fleming, G. R. Quantum coherence enabled determination of the energy landscape in light harvesting complex II. *J. Phys. Chem. B* **2009**, *113*, 16291-16295.

[6]   Schlau-Cohen, G. S.; Calhoun, T. R.; Ginsberg, N. S.; Read, E. L.; Ballottari, M.; Bassi, R.; van Grondelle, R.; Fleming, G. R. Pathways of energy flow in LHCII from two-dimensional electronic spectroscopy. *J. Phys. Chem. B* **2009**, *113*, 15352-15363.

[7]   Abramavicius, D.; Voronine, D. M.; Mukamel, S. Unravelling coherent dynamics and energy dissipation in photosynthetic complexes by 2D spectroscopy. *Biophysical Journal* **2008**, *94*, 3613-3619.

[8]   Womick, J. M.; Moran, A. M. Exciton coherence and energy transport in the light-harvesting dimers of allophycocyanin. *J. Phys. Chem. B* **2009**, *113*, 15747-15759.

[9]   Collini, E.; Scholes, G. D. Coherent intrachain energy migration in a conjugated polymer at room temperature. *Science* **2009**, *323*, 369-373.

[10]   Zhang, T.; Kuznetsova, I.; Meier, T.; Li, X.; Mirin, R. P.; Thomas, P.; Cundiff, S. T.; Polarization-dependent optical 2D Fourier transform spectroscopy of semiconductors. *Proc. Nat. Acad. Sci.* **2007**, *104*, 14227-14232.

[11]   Kasha, M.; Rawls, H. R.; Ashraf El-Bayouni, M. The exciton model in molecular spectroscopy. *Pure Appl. Chem.* **1965**, *11*, 371-392.

[12]   Knoester, J. Optical properties of molecular aggregates. *Proceedings of the International School of Physics - Organic Nanostructures: Science and Applications.* IOS Press: Amsterdam, 2002, 149-186.

[13]   Mukamel, S. *Principles of Nonlinear Optical Spectroscopy.* Oxford University Press: Oxford, 1995.

[14]   Cantor, C. R.; Schimmel, P. R. *Biophysical Chemistry Part II: Techniques for the study of biological structure and function.* Freeman: New York, 1980; Vol. 2.

[15]   Cho, M.; Brixner, T.; Stiopkin,I.; Vaswani, H.; Fleming, G. R. Two dimensional electronic spectroscopy of molecular complexes. *J. Chem. Chin. Chem. Soc.* **2006**, *53*, 15-24.

[16]   Cho, M.; Fleming, G. R. The integrated photon echo and solvation dynamics. II. Peak shifts and two-dimensional photon echo of a coupled chromophore system. *J. Chem. Phys.* **2005**, *123*, 114506/1-114506/18.

[17]   Cho, M. *Two-Dimensional Optical Spectroscopy*, CRC Press: Boca Raton, 2009.

[18]   Cho, M. Coherent two-dimensional optical spectroscopy. *Chem. Rev.* **2008**, *108*, p. 1331.

[19]   Craig, D. P.; Thirunamachandran, T. *Molecular Quantum Electrodynamics: An Introduction to Radiation Molecule Interactions.* Dover Publications, Inc.: New York. 1998.

[20]   Kjellberg, P.; Pullerits, T. Three-pulse photon echo of an excitonic dimer modeled via Redfield theory. *J. Chem. Phys.* **2006**, *124*, 024106/1-024106/9.

[21]   May, V.; Kuhn, O. *Charge and Energy Transfer Dynamics in Molecular Systems,* Wiley-VCH: New York, 2004.

[22]   MacMillan, J. B.; Molinski, T. F. Long-range stereo-relay: Relative and absolute configuration of 1,*n*-glycols from circular dichroism of liposomal porphyrin esters. *J. Am. Chem. Soc.* **2004**, *128*, 9944-9945.

[23] Khalil, M.; Demirdoven, N.; Tokmakoff, A. Coherent 2D IR Spectroscopy: Molecular Structure and Dynamics in Solution. *J. Phys. Chem. A* **2003**, *107*, 5258-5279.

[24] Khalil, M.; Demirdoven, N.; Tokmakoff, A. Obtaining Absorptive Line Shapes in Two-Dimensional Infrared Vibrational Correlation Spectra. *Phys. Rev. Lett.* **2003**, *90*, 047401/1-047401/4.